THE UNIVERSITY OF MANITOBA

ON THE FORMATION OF SOLUTE DEPLETED ZONES ON THE SURFACE OF A γ-TiAl ALLOY DURING HEAT-TREATMENT

By

UTTARA PRASAD

A thesis
submitted to the faculty of graduate studies
in partial fulfillment of the
requirements for the degree of
Master of Science

DEPARTMENT OF MECHANICAL AND INDUSTRIAL ENGINEERING
WINNIPEG, MANITOBA
AUGUST 1998

THE UNIVERSITY OF MANITOBA

FACULTY OF GRADUATE STUDIES

*****

COPYRIGHT PERMISSION PAGE

ON THE FORMATION OF SOLUTE DEPLETED ZONES ON THE SURFACE OF A γ-TiAl ALLOY DURING HEAT-TREATMENT

BY

UTTARA PRASAD

A Thesis/Practicum submitted to the Faculty of Graduate Studies of The University of Manitoba in partial fulfillment of the requirements of the degree

of

MASTER OF SCIENCE

ACKNOWLEDGEMENTS

I take this opportunity to thank Dr. M. C. Chaturvedi for his guidance and encouragement throughout the course of this work.

Thanks are due to Dr. A. K. Jena for his valuable suggestions and thought-provoking discussions and also to Dr. Q. Xu for many helpful discussions. I would also like to acknowledge the technical assistance of Mr. John Van Dorp and Mr. Don Mardis at various stages of this work.

My special thanks to my friends, Chandra and Chithra, for their help and support during the last one year. Last but not the least, I would like to thank all my family members, especially my parents for their constant support and encouragement.

ABSTRACT

An investigation was carried out on Ti-45Al-2Mn-2Nb alloy, to study the mechanism of solute depletion from the surface of the specimen and formation of solute depleted damaged layer during heat treatment. Small specimens were wrapped in tantalum foil and encapsulated in vycor capsules which were evacuated and backfilled with 160 torr of commercial argon. The encapsulated specimens were annealed at 1200°C for various time periods, viz. 15 hrs, 30 hrs and 50 hrs. A solute depleted damaged layer was observed to form in all the specimens which were heat treated at 1200°C. The thickness of damaged layer was found to have parabolic relation with time. The mechanism involved in solute depletion was proposed. The phases present in the damaged layer were identified by detailed transmission electron microscopy. The damaged layer in the specimens heat treated at 1200°C, was found to consist of α_2 phase near the interface between the undamaged lamellar bulk and the damaged layer, B2 phase with ω-type precipitates (ω″) in the central region of the damaged layer and B2 phase with ω-type phase having $B8_2$ structure near the outer edge of the specimen.

TABLE OF CONTENTS

LIST OF FIGURES

LIST OF TABLES

Chapter 1

INTRODUCTION

Approximately 30 years ago, the U.S. Air Force recognized that titanium aluminide based systems offered great potential for application in the hot sections of jet engines [1]. Such alloys exhibit numerous attractive properties for high temperature structural applications. The density of titanium aluminides is less than half of that of superalloys. The ordered structure of the aluminides reduces disiocation mobility and diffusion processes at elevated temperatures and consequently, promotes attractive elevated temperature properties. Titanium aluminides have high specific moduli, high specific strength and good oxidation resistance [2,3]. Therefore, γ-TiAl based alloys have emerged from a group of wide-composition range intermetallic compounds to be the first to enter commercial jet engine service and have attracted a great deal of attention from the aerospace community and the automobile industry [2-5].Various components of gas turbine engines including the rotating parts like low pressure turbine, high pressure compressor blades, and high pressure turbine blade cover plates, and the stationary parts like transition duct beams, vanes, swirlers, cases, and nozzle flaps and tiles have been identified to be made of γ-TiAl based alloys [2,5].

The gamma titanium aluminide alloys of engineering importance are based on Ti-(45-48)Al [2]. These are two phase alloys containing the phases, α_2 and γ. Due to the satisfactory properties of these alloys for high temperature structural applications their acceptance is growing in aerospace and automobile industries [6-8]. However, titanium aluminides have

certain shortcomings. The key shortcomings are: low ductility, low fracture toughness and poor oxidation resistance above 850°C. Various efforts are being made to overcome these problems by proper processing, alloying and microstructure control. Microstructures of TiAl-based alloys can be greatly altered by thermal and thermo-mechanical treatments. Since microstructure is the major controlling parameter for mechanical properties, the properties are being considerably improved by appropriate thermal as well as thermo-mechanical treatments.

Processing by thermal and thermo-mechanical treatments requires exposure of the material to high temperatures. Since, the rates of diffusion of components is very low, the transformation rates are low and longer heat treatments at higher temperatures are required for promoting changes in the microstructure. During such heat treatments undesirable changes in the microstructure have been reported to occur near the surface of the heat treated samples [8,9]. Ramanujan *et al.* [8] observed a variety of microstructural changes near the surface of the samples of Ti-47Al alloys subjected to different heat treatments under vacuum at 800-1250°C . They referred the zone close to the surface of the specimen as "damaged layer". A change in microstructure was also observed near the surface when the Ti-48Al-2Mn-2Nb alloy was vacuum heat treated at 1300°C [9].The change in microstructure was attributed to either the loss of aluminum or the increase in the oxygen content experienced during heat treatment. However, the problem was not analysed in detail. Changes in microstructure have also been reported during long term oxidation tests of TiAl-based titanium aluminides due to Al-depletion [10-12]. Formation of depletion layer also occurred during oxidation in low air pressure at ~1000°C [13].

Such surface damage and near surface microstructural changes are undesirable. They degrade the properties of the material during fabrication as well as during service. Particularly, the properties like fatigue resistance, oxidation resistance and surface finish are considerably altered. For alloy development and processing and for the effective use of the alloy, it is necessary to avoid such surface damage. Unfortunately, no effort has so far been made either to understand the cause of this phenomenon or to find ways of preventing its occurrence. The present research was undertaken to investigate the microstructural changes which occur near the surface of the specimen during vacuum heat treatment of TiAl-based titanium aluminides.

Chapter 2

LITERATURE REVIEW

2.1 PHASE EQUILIBRIA

2.1.1 Ti-Al Phase Diagram

The first detailed investigation of the Ti-Al system was carried out by Ogden *et al.* [14] in 1951. They summarized the results of prior investigations and proposed a phase diagram of the Ti-Al system. In 1952, Bumps *et al.* [15] studied the Ti-Al system more carefully and in greater detail. They proposed a complete phase diagram of binary Ti-Al system by combining their results with other available data.

Murray [16] revised the Ti-Al phase diagram in 1988 and proposed the eutectoid reaction $\alpha \rightarrow \alpha_2 + \gamma$ at 1125°C. This phase diagram was further revised by McCullough *et al.* [17] who introduced two peritectic reactions, $L+\beta \rightarrow \alpha$ and $\alpha+L \rightarrow \gamma$ and indicated the absence of the peritectoid reaction at 1285°C. This was later verified by Jones and Kaufman [18]. Later, Ding *et al.* [19] also confirmed the absence of the peritectoid reaction at 1285°C. They also suggested that the eutectoid transformation was virtually impossible to achieve experimentally in this system because of the large differences in the transformation kinetics of the two product phases, α_2 and γ. The γ phase can precipitate either from α or from α_2 depending upon the composition and cooling rate.

The most widely accepted Ti-Al binary phase diagram is shown in Fig.2.1 [20]. Recently,

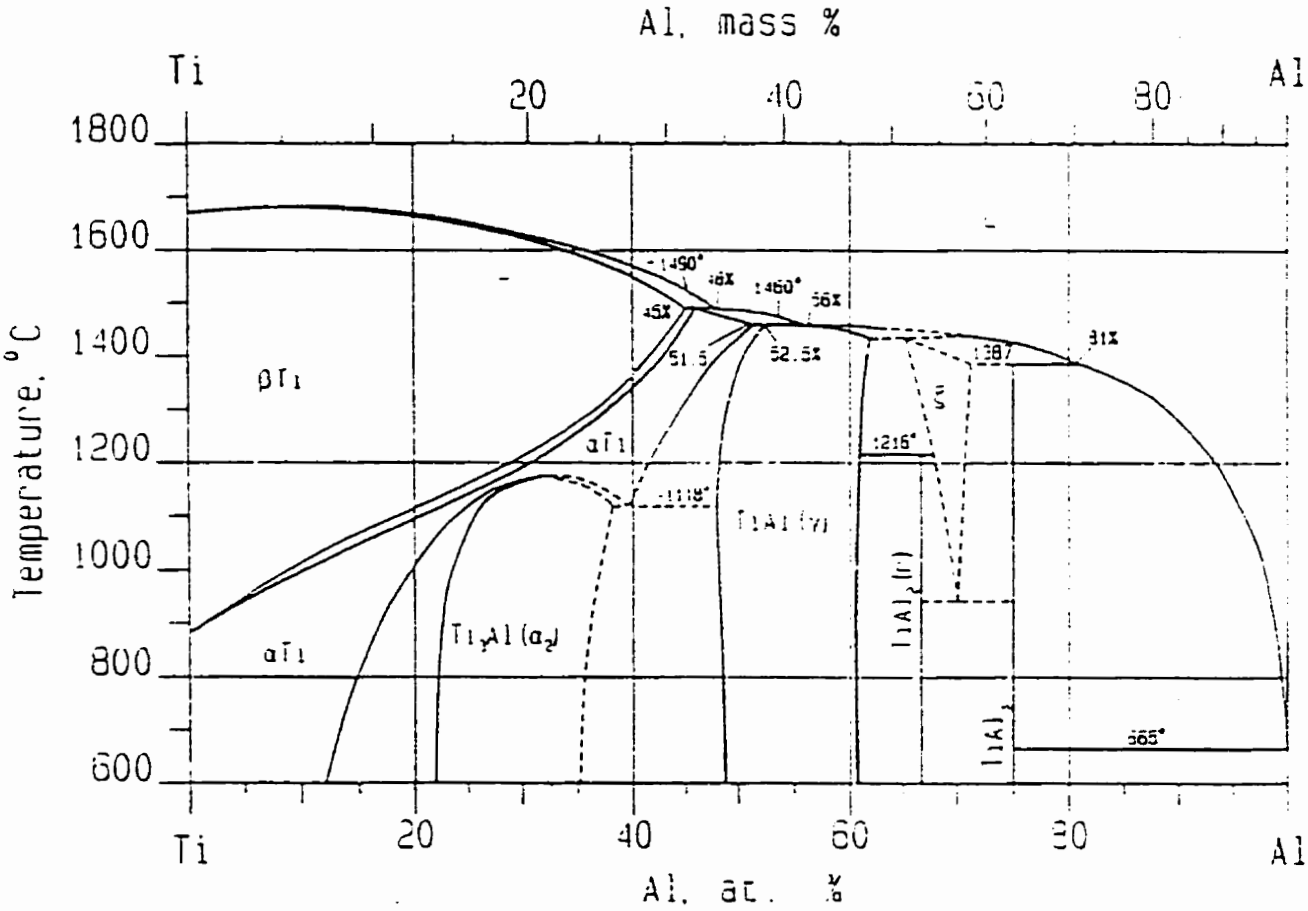

Fig.2.1 Most widely accepted binary Ti-Al phase diagram. [20]

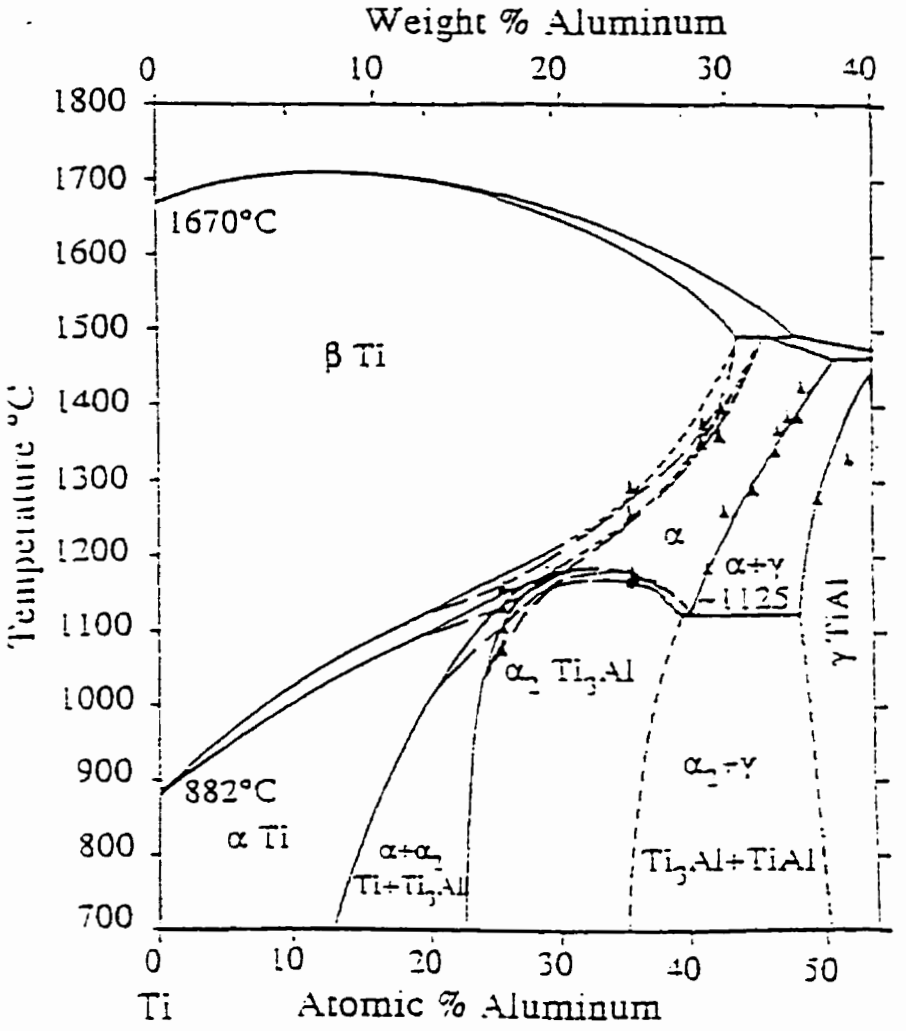

Fig.2.2 Modified Ti-Al phase diagram. [21]

Veeraraghavan *et al.* [21] studied the Ti-Al system in the composition range of 25-52 at.% Al using electrical resistivity. They have made slight modifications in the phase boundaries. Their proposed modifications are shown in Fig.2.2.

Thus, till to date there is still some controversy about the Ti-Al phase diagram. Several phase boundaries are uncertain and hence, it is not possible to precisely define the transformation paths for phase transformations.

2.1.2 **Structure and Properties of Phases**

TiAl: The titanium aluminide, TiAl is often designated as the γ phase. It crystallizes with the tetragonal $L1_0$ structure (AuCu-type). The TiAl unit cell is illustrated in Fig.2.3. The $L1_0$ structure results due to ordering in the fcc lattice (Al). The face centered cubic structure is tetragonally distorted because alternate (002) planes are occupied by atoms of the same component. The c/a ratio is 1.015 at the stoichiometric composition. The crystal structure data of γ phase are given in Table 2.1 [22]. The γ phase remains ordered upto its melting point.

The maximum composition range of stability of TiAl is 48-60 at.% Al. The high aluminum content of this compound also increases its resistance to oxidation and burning [23]. TiAl has low density (Table 2.2) which is an important attribute for jet engine applications as light weight enhances engine performance. The heat of formation of –40

kJ/g-atom of TiAl suggests formation of strong bonds that lead to higher activation energy for diffusion, and help in strength retention at higher temperatures and in increased resistance to creep. However, γ phase lacks ductility and toughness. These mechanical properties can be improved to some extent through microstructural control and suitable alloying additions.

Ti_3Al: The titanium aluminide, Ti_3Al is often designated as the α_2 phase. It has an hexagonal ordered DO_{19} structure (Ni_3Sn-type). The schematic unit cell of Ti_3Al is shown in Fig.2.4. The ratio (c/a) of the lattice parameters c and a is 0.8 for stoichiometric composition. The crystal structure data of this phase are given in Table 2.1. The α_2 phase disorders above 1180°C to form the disordered hexagonal α phase.

The maximum composition range of stability of α_2 phase is 24 to 36 at.% Al. Some of the properties of α_2 phase are given in Table 2.2. The α_2 phase also lacks room temperature ductility. The ductility can however, be improved by alloying with sufficient amount of β stabilizing element like Nb [24]. In the presence of Nb, the high temperature β phase is retained upon cooling to low temperatures and becomes ordered. This ordered bcc phase is called the B2 phase. A small volume fraction of B2 phase increases the ductility of α_2 alloys to 3-8 %. The presence of B2 phase is believed to delay the cleavage crack nucleation in α_2 and consequently, results in higher ductility. The presence of large volume fractions of B2 phase results in loss of creep resistance. Effort has also been made to improve the room temperature ductility of α_2 phase by grain refinement [25,26].

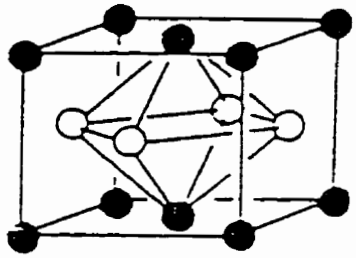

Fig.2.3 TiAl unit cell.

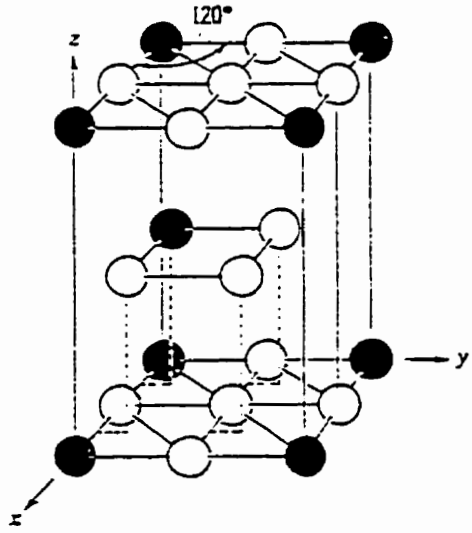

Fig.2.4 Ti_3Al unit cell.

Phase	Strukturbericht symbol	Crystal structure	Space group	Lattice parameter		
				a	b	c
Ti_3Al (α_2)	DO_{19}	Ordered hexagonal	$P6_3/mmc$	0.5782	–	0.4629
TiAl (γ)	$L1_o$	Ordered F.C.T	P4/mmm	0.4005	–	0.4070
B2	DO_3	Ordered bcc	$Pm\ \bar{3}m$	0.322	–	–
ω-type	$B8_2$	Hexagonal	$P6_3/mmc$	0.45803	–	0.55204
ω	–	Hexagonal	P6/mmm	0.46	–	0.58
ω^c	–	Trigonal	$P\ \bar{3}m1$	0.4555	–	0.5542

Table 2.1 Crystal structure data of stable and metastable phases.

Properties	Ti_3Al	$TiAl$
Density (gm/cm^3)	3.8 – 4.0	4.1 – 4.7
Youngs Modulus (GPa)	160 – 175	120 – 145
Ductility (%)	1 – 3	2 – 5
Yield Strength (MPa)	400 – 650	700 – 990
Upper Limit for Structural Stability (°C)	1440	1180
Creep Limit (°C)	850	750
Oxidation Limit (°C)	850	650

Table 2.2 Properties of titanium aluminide alloys

2.1.3 Effect of alloying additions

Alloys that have been developed for engineering applications can be grouped into either single phase (γ) alloys or two phase ($\alpha_2+\gamma$) alloys. Initially, single phase alloys attracted attention because of their excellent resistance to environmental attack by oxidation and hydrogen absorption. However, their importance as engineering alloys has diminished due to their poor ductility and toughness. Gamma titanium aluminide alloys of engineering importance are two phase alloys based on Ti-(45-48)Al with appropriate combination of alloying elements. The new generation alloys under development have compositions of Ti-(45-47.5)Al-(1-2)M-(2-6)N-x(W, Hf, C)-(0-0.3)B, where M=Cr, V, Mn and N=Nb, Mo, Ta [2,26].

Phase Equilibria

The alloying elements modify the binary phase diagram. The modifications are manifested as changes in the shape and size of the gamma phase field due to shifting of $(\alpha+\gamma)/\gamma$ phase boundary. Three types of gamma phase field can form in the isothermal sections of Ti-Al-X (X=M or N) systems [2,26,27] (Fig.2.5). The type N elements replace titanium to form type I phase field. Type M elements can substitute either for both titanium and aluminum to form type II phase field or for aluminum only to form type III phase field. For a given alloy composition, the aluminum content in γ phase varies depending on the type of alloying element. The aluminum content of γ phase remains unchanged or increases slightly with increase in the content of type N alloying elements

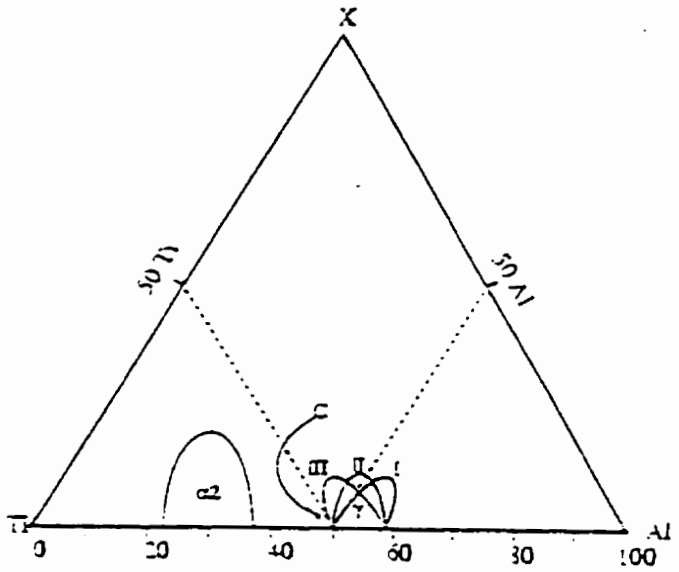

Fig.2.5 Three typical gamma phase fields formed due to addition of alloying elements. [2,26,27]

in type I, whereas the aluminum content decreases with increase in the content of type M elements in type II and III. In the Ti-48Al-2Nb alloy, where Nb is a type I phase field former, aluminum content in γ phase is the same as that in the Ti-48Al alloy [28]. However, at Nb contents between 2 to 8 %, a segment of the phase boundary extends across the 50Al line resulting in lowered aluminum content in the γ phase [4,29]. In the Ti-48Al-2Mn alloy, where Mn is a type III phase field former, the aluminum content of γ phase is lower than that in the Ti-48Al alloy. A similar decrease in aluminum content has been predicted in case of type II phase field forming alloying elements and been observed in the alloys Ti-48Al-(1-3)V and Ti-48Al-(1-3)Cr [26].

The Ti-Al-Mn System: There is a lack of information on the Ti-Al-Mn system. This system was first studied in 1955 by Domagala and Rostoker [30] who investigated the composition range defined by Ti and the binary compositions of TiAl and Mn_2Ti at temperatures in the range of 700-1200°C. At elevated temperatures, the phase fields α-Ti(hcp), β-Ti(bcc), ($\alpha + \beta$), ($\alpha + \beta + \gamma$–TiAl) and ($\beta + \gamma$–TiAl +Mn_2Ti) were established, but the ordered α_2-Ti_3Al field was not identified. Domagala and Rostoker found that only body centered cubic β–Ti appeared to have large solubility for Mn and they did not report any new ternary phase. Later, work done by Chakrabarti [31] on Mn rich alloys of the Ti-Al-Mn system showed extensive solubility of aluminum in Mn_2Ti. This is a Laves phase of $MgZn_2$ type and is known to exist in the binary Ti-Mn system. Chakrabarti reported ~ 30 at.% Al in Mn_2Ti. His data indicate that the Laves phase extends into the ternary system along a line of approximately constant Ti content (~35 at.%). This observation suggests that Al substitutes for Mn in the Laves phase and that the phase

should be properly represented by the formula $(Mn, Al)_2Ti$. Jacob and Shaltiel [32] subsequently confirmed this result. Hashimoto *et al.* [33] performed the study in a composition range of 36-38 at.% Al and upto 5 at.% Mn. But instead of $(Mn, Al)_2Ti$, they reported the formation of of a ternary phase $Mn_2Al_3Ti_3$ (ξ–phase) along with α_2–Ti_3Al and γ-TiAl.

Butler *et al.* [34] recently investigated the solidification microstructures in the ternary Ti-Al-Mn system for Ti/Al ratio of ~1.14 with Mn levels of 5, 10, 20, and 30 at.% and proposed isothermal sections of the ternary Ti-Al-Mn phase diagram at high temperatures. They observed that for 5 and 10 at.% Mn alloys, the microstructure consisted of lamellar γ/α_2 and interdendritic γ, β and $(Mn,Al)_2Ti$. The microstructure of 20 % Mn alloy was reported to have accicular plates of $(Mn, Al)_2Ti$ in a matrix of β and α/α_2. On the other hand, 30 % Mn alloy had primary dendrites of $(Mn, Al)_2Ti$ with only small quantity of secondary phases.

The Ti-Al-Nb System: Limited research has been carried out to assess the effect of Nb on phase relations and deformation behavior in the ternary Ti-Al-Nb system. Nb behaves as a β stabilizer and also shows solid solution strengthening. However, the main purpose of adding Nb to γ titanium aluminides is to improve the oxidation resistance of the alloy.

Kaltenbach *et al.* [35] studied the binary Nb-Ti and Al-Nb as well as ternary Ti-Al-Nb systems. The isothermal section of Ti-Al-Nb system at 900°C is shown in Fig.2.6 [36]. Several other isothermal sections are also available [2,37-39]. The Ti-Al-Nb system has

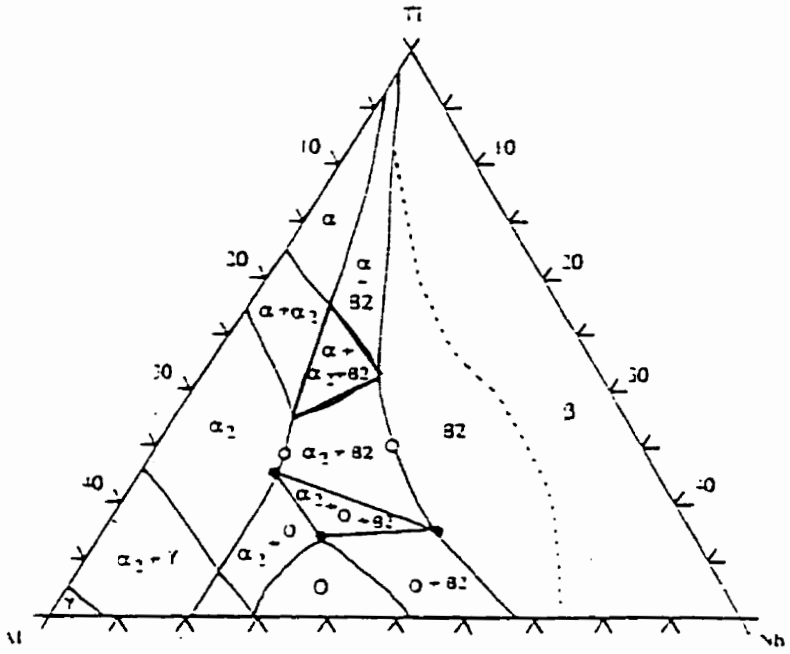

Fig.2.6 Isothermal section of Ti-Al-Nb system at 900°C. [36]

recently been analyzed in detail by Hellwig *et al.* [40]. The Ti-Al-Nb phase diagrams proposed by Hellwig *et al.* are shown in Fig.2.7(a & b) . Li and Loretto [29] found that addition of Nb expands the γ phase field by shifting the $(\alpha+\gamma)/\gamma$ phase boundary towards Al- lean side.

In Ti-Al-Nb alloys containing 5 to 17 at.% Nb, a ductile ordered bcc phase (B2) forms upon quenching from high temperatures [41,42]. The B2 phase forms by the ordering of equilibrium high temperature β phase in the Ti-Al-X system, where X is a β stabilizing ternary addition [22]. Formation of a number of phases has been also observed subsequent to the ordering of β [41,42]. These phases are known as ω or ω related phase. Additionally, an ordered orthorhombic phase has also been detected in Ti-Al-Nb alloys with an approximate stoichiometry of Ti_2AlNb [43,44].

B2 phase has an ordered body centered cubic structure (CsCl-type). The B2 unit cell is shown in Fig.2.8. The crystal structure data of B2 phase observed in Ti-Al-Nb system [42] are given in Table 2.2. The B2 phase has a large number of independent slip systems and as a result it has a relatively high ductility [24]. Large number of slip systems also result in a decrease in creep resistance of the alloy. The ω-type phase which forms as a result of decomposition of B2 phase has $B8_2$ structure. The transition phases which appear due to decomposition of B2 phase are referred to as $\omega'$and ω'' [41,42]. The ω-type phase has also been observed in the quenched in B2 phase [36]. The crystal structure data of ω', ω'' and ω-type phases are given in Table 2.2.

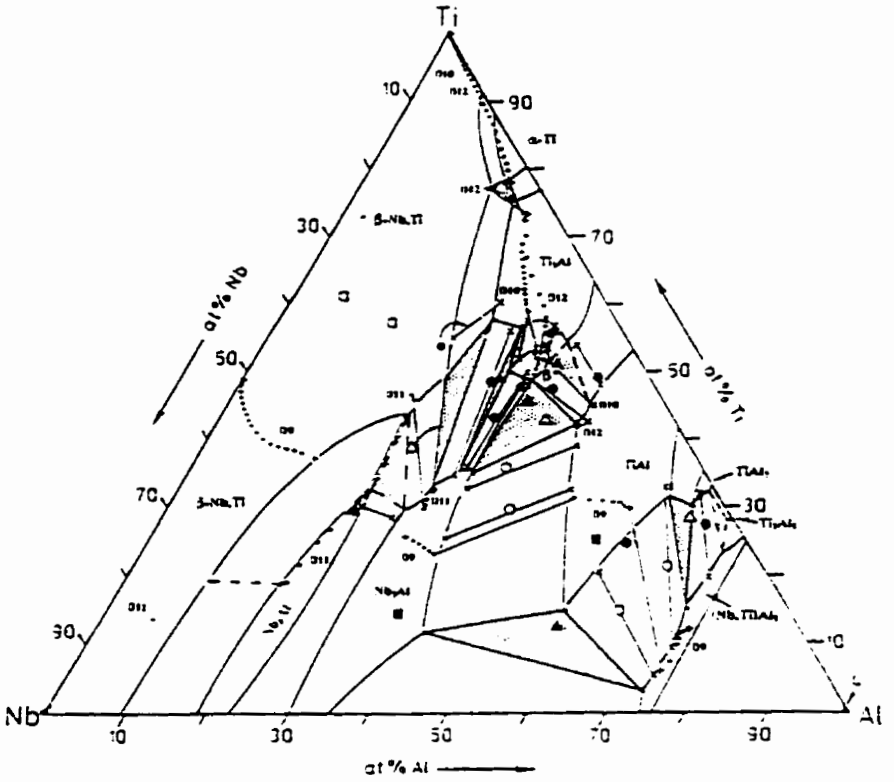

(a)

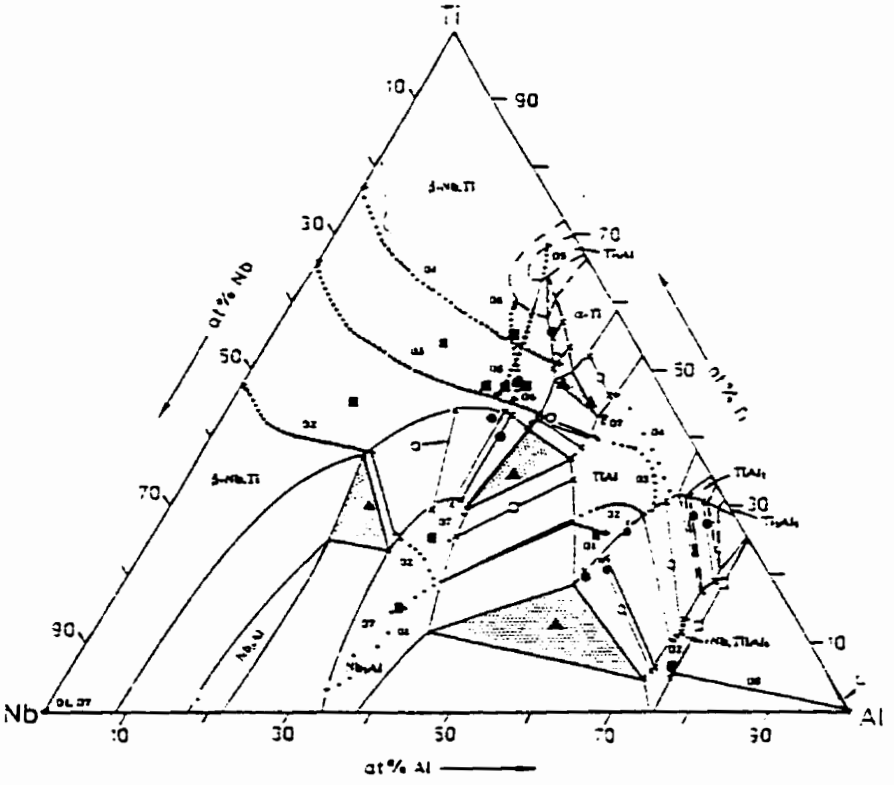

(b)

Fig.2.7 Ti-Al-Nb phase diagram at (a) 1000°C and (b)1200°C. [40]

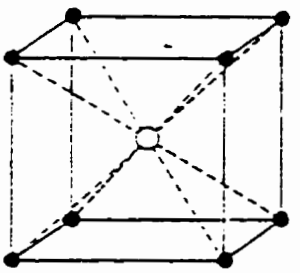

Fig.2.8 B2 unit cell.

Mechanical Properties

The M type elements when present either as individuals [27,28] or as a combination [26] increase the ductility of two phase alloys. For example, an addition of (1-3) at.% (V, Cr, Cr+Mn, or V+Cr) to the Ti-48Al alloy almost doubles its ductility [2,45-47]. To be effective in ductilization, the alloying elements should be limited to 1-3 at.% so that formation of excessive B2 phase is avoided, and the duplex structure should be maintained. V, Mn and Cr impart no ductilization to the single phase or fully lamellar structures [10]. Fig.2.9 shows the effect of ternary additions on the ductility of TiAl-based alloys. Various efforts have been made to identify the causes for ductilizing by elements such as Cr, V, and Mn in terms of phase stabilization, site occupation or γ/α volume fraction. The prediction that for a given grain size improved ductility is related to the decreased Al content due to the ability of these alloying elements to shift the phase boundary towards Ti-rich side, appears to be valid [2,4].

The addition of Nb and Ta increases the creep strength by slowing down the diffusion process whereas the addition of W and Si improves the creep resistance through microstructural modifications [48,49]. The addition of W tends to form β particles and promotes $\alpha_2+\gamma$ lamellar structure. It is, however not clear as to which aspect of the microstructural modification is more responsible for the improvement in creep resistance [23]. Addition of Cr reduces the creep rate of TiAl [50]. The effect of alloying elements on the creep curve of TiAl-based alloys is shown in Fig.2.10.

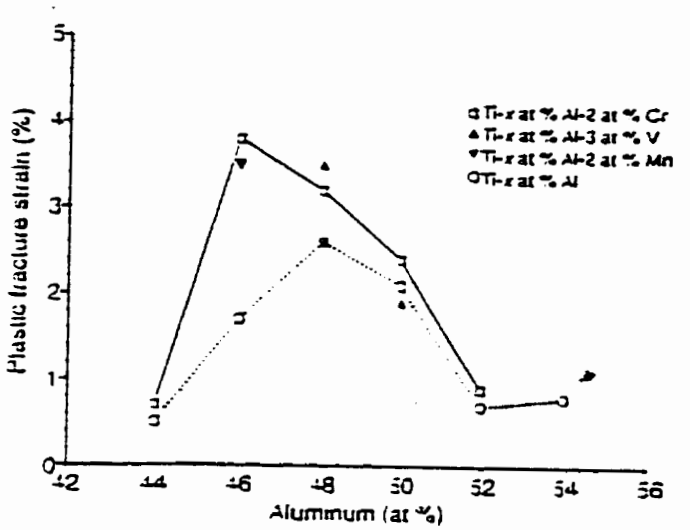

Fig.2.9 Effect ofalloying elements and Al content on the ductility of titanium aluminides. [23]

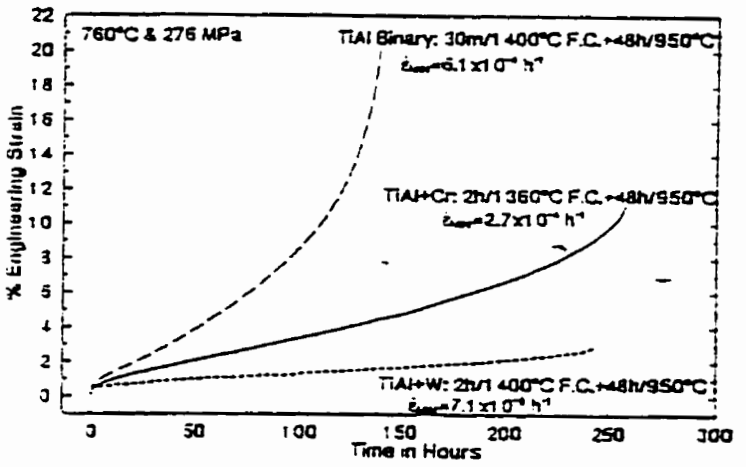

Fig.2.10 Comparison of creep curves for different alloying additions. [93]

Oxidation Resistance

A number of alloying elements have been reported to improve the oxidation resistance of TiAl-based alloys. One such element is Nb. The effect of Nb can be quite dramatic even when a small amount (1-2 %) of it is used. With only 2 at.% Nb it is possible to use the alloy at temperatures as high as 800°C without a need of protective coating [23,51]. W and Mo also have similar effects. Ta reduces oxidation rate but the oxide scale tends to spall under rapid thermal cycling conditions [52]. The effect of ternary additions on oxidation resistance of TiAl-based alloys is shown in Fig.2.11 [23]. The ability of these elements to improve oxidation resistance depends on the type of quaternary addition [51,53]. With the addition of 2 % Nb to the Ti-48Al-2Cr alloy, the oxidation resistance of the alloy can be considerably improved. On the other hand, addition of Nb to the Ti-48Al-2V alloy does not improve the oxidation resistance. Besides these refractory elements, P is also reported to decrease significantly the oxidation rate at 0.1 at.% level [54]. Si decreases the oxidation rate by forming an SiO_2 layer which is more protective than TiO_2, and Y improves the adhesion of surface oxide [55].

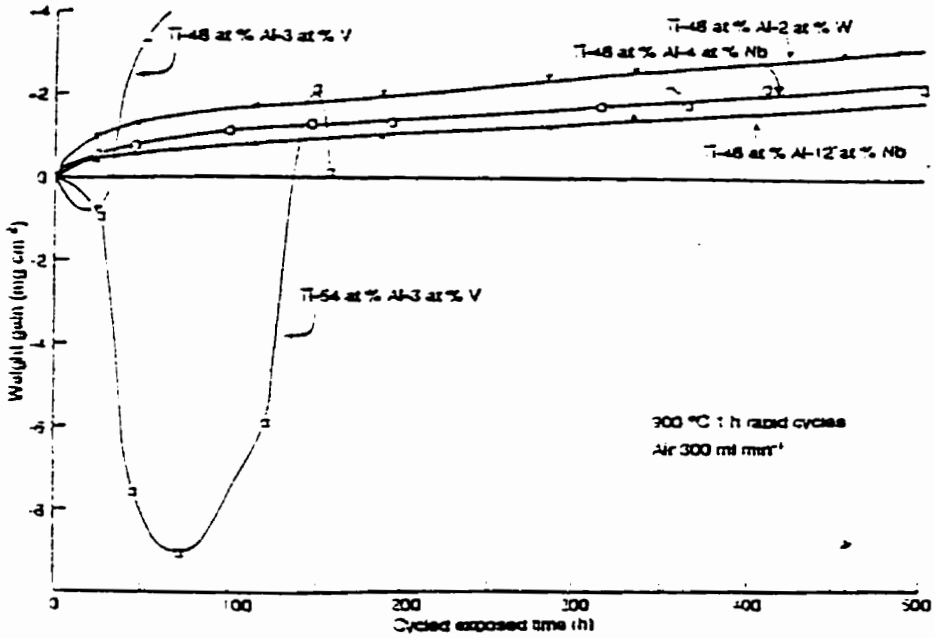

Fig.2.11 Effect of ternary additions on oxidation resistance of TiAl-based alloys. [23]

2.2 Phase Transformations

In order to understand the relationship between microstructure and mechanical properties of titanium aluminide alloys, investigations on phase transformations in the Ti-Al system have been carried out and numerous transformation modes have been identified to be operative during various heat treatments. The important transformations relate to the $\alpha \rightarrow \alpha_2$ ordering, formation of two phase γ/α_2 lamellar structure, $\alpha \rightarrow \gamma_m$ massive type transformation, discontinuous coarsening of the lamellar structure and formation of monolithic γ-grains [56].

2.2.1 $\alpha \rightarrow \alpha_2$ Ordering Reaction

The $\alpha \rightarrow \alpha_2$ transformation is a simple ordering reaction. The reaction involves ordering of a disordered hexagonal structure. Consequently, the transformation from α to α_2 can occur quickly and without any significant undercooling [57].

The nature of decomposition of the α phase during subsequent cooling is a strong function of both the composition and the cooling rate. The CCT diagrams reproduced in Fig.2.12(a-d) [18], show that the α phase can completely transform to α_2 phase upon water quenching for aluminum contents between 40 to 45 at.%. However, in the same composition range slower cooling rates yield two phase lamellar structure consisting of γ and α_2 . Also, for aluminum contents greater than 45 at.% it is almost impossible to have

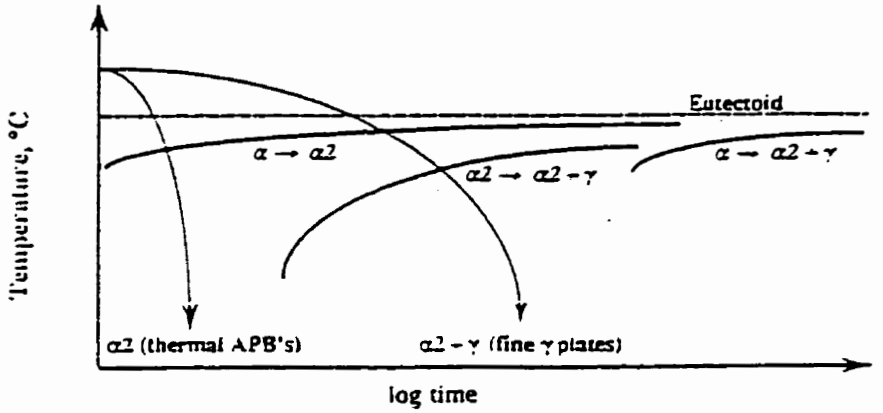
Temperature, °C
Eutectoid
α → α2
α2 → α2 + γ
α → α2 + γ
α2 (thermal APB's)
α2 + γ (fine γ plates)
log time

(a)

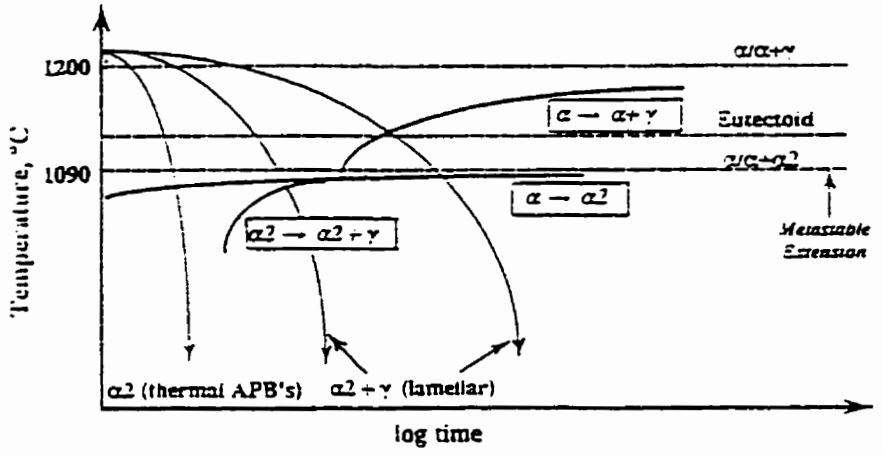
Temperature, °C
1200
1090
α/α+γ
α → α+γ
Eutectoid
α/α+α2
α → α2
α2 → α2 + γ
Metastable Extension
α2 (thermal APB's)
α2 + γ (lamellar)
log time

(b)

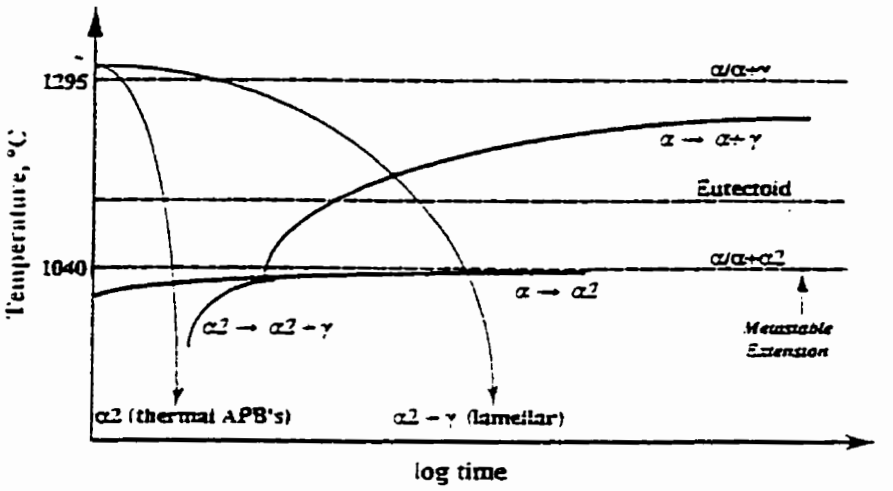

(c)

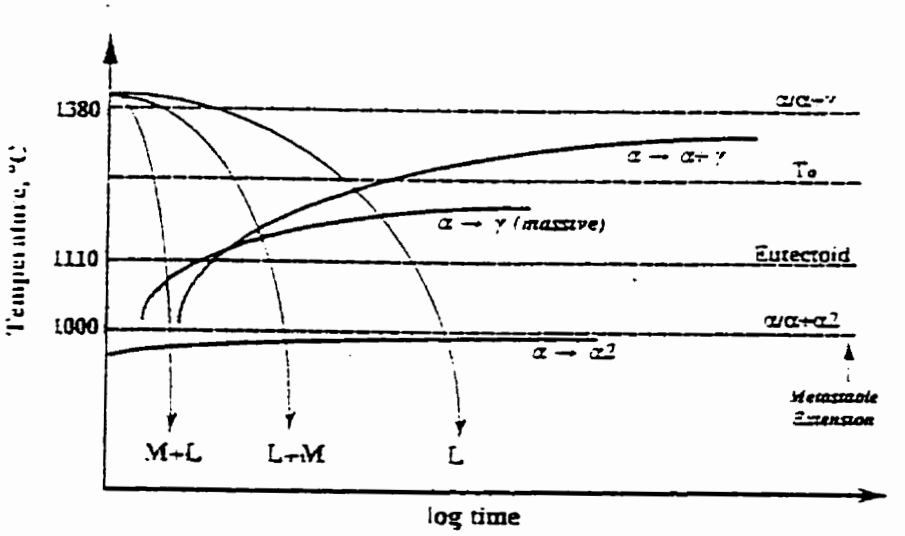

(d)

Fig.2.12 Schematic CCT diagrams for alloys containing (a) 40 at.% Al, (b) 42 at.% Al, (c) 45 at.% Al, and (d) 48 at.% Al. [18]

$\alpha \rightarrow \alpha_2$ transformation prior to other modes of transformation even with very high cooling rates.

2.2.2 $\alpha \rightarrow \alpha_2 + \gamma$ Eutectoid Reaction

Decomposition of the high temperature disordered hexagonal α phase during subsequent cooling gives rise to the formation of two ordered phases, γ (TiAl) and α_2 (Ti_3Al). The α_2 and γ lamellae have the orientation relation: $(0001)_\alpha$ // $(111)_\gamma$ and $<2110>_\alpha$ // $<110]_\gamma$. This relationship is known as Blackburn's relationship and has been confirmed in a number of studies [58-61]

Mechanism of the transformation: Several investigations have been carried out to establish the mechanism of decomposition of the α phase and the formation of $\alpha_2+\gamma$ lamellar structure [56,57,62,63,67]. The formation of the lamellar structure does not occur through a eutectoid reaction but results from the precipitation of the γ lamellae in either a disordered α or an ordered α_2 matrix [19,57,62,63] following one of the two reaction sequences: (1) $\alpha \rightarrow \alpha_2 \rightarrow \alpha_2 + \gamma$ or (2) $\alpha \rightarrow \alpha + \gamma \rightarrow \alpha_2 + \gamma$. The lamellar structure formation involves ordering of α to α_2, a crystal structure change from HCP to FCC type, a chemical composition change through atom transfer, and an ordering reaction of the FCC type structure leading to the final $L1_o$ γ phase [57,62]. A fully lamellar structure can be formed in both the $(\alpha+\gamma)$ and the $(\alpha_2+\gamma)$ phase fields [18,56].

The precipitation of the γ phase from the α or α_2 phase most likely starts by the propagation of Shockley partial dislocations in the hexagonal matrix. This mechanism

was initially proposed by Blackburn [64] and was confirmed by the presence of numerous stacking faults in the hexagonal matrix [61,62]. It has also been suggested that the initiation process of the transformation involves the dissociation of a perfect a/3<1120> dislocation into two Shockley partials bordering a stacking fault. Such a stacking fault locally creates an FCC type stacking sequence in the hexagonal matrix. Repeating this mechanism every two basal planes of the hexagonal matrix brings the crystal structure change (hcp→fcc) to completion. Since, the close-packed planes and directions of hcp and fcc are parallel to each other, planar and highly coherent interfaces are formed. The formation of a local fcc stacking sequence and the creation of highly coherent interfaces constitute a sort of prenucleation stage, strongly lowering the nucleation barrier to the precipitation of the γ phase.

The growth of γ lamellae involves both structural and compositional changes. Due to planar and coherent interfaces, transfer of atoms is quite restricted and takes place by "terrace-ledge-kink" mechanism [65-67]. Fig.2.13 [67] is a schematic illustration for explaining the formation mechanism of the γ plates. As can be seen in this figure, the growth of the γ plates proceeds by shear for plate lengthening and diffusion of atoms for plate thickening. It has, however, been shown that the transformation is mostly dominated by shear [57,62,67].

Effect of composition and temperature on the transformation: The Ti-Al phase (Fig.2.14) diagram shows three possible temperature ranges in which the transformation

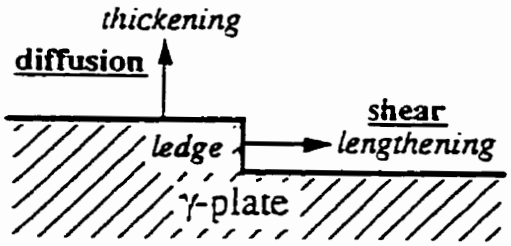

Fig.2.13 Schematic diagram showing growth of γ plates. [67]

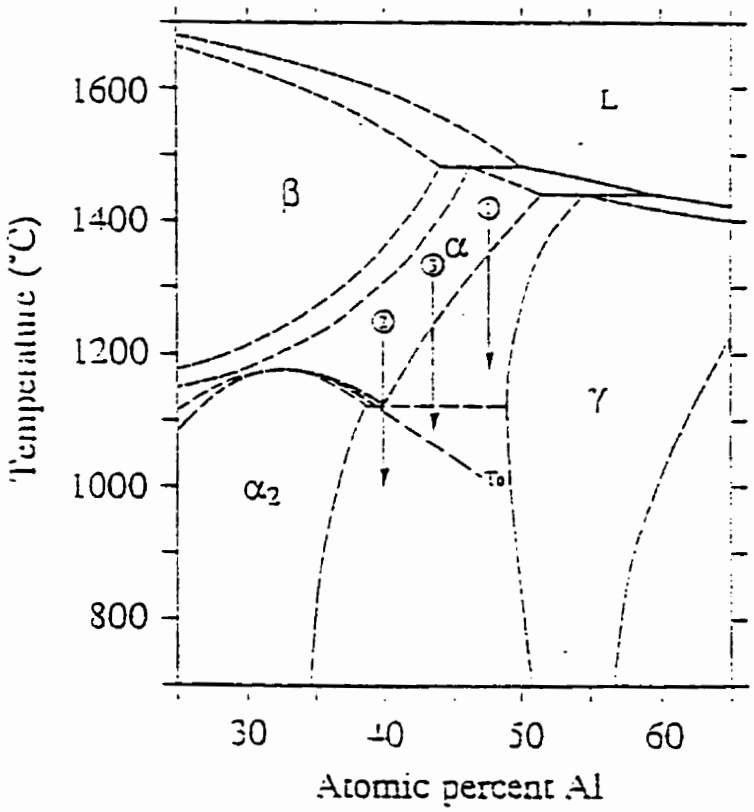

Fig.2.14 Central portion of the Ti-Al phase diagram. [63]

can take place [63]. If the α single phase is quenched to $\alpha+\gamma$ two phase field (alloy 1) above the eutectoid temperature and aged isothermally, the microstructure is lamellar $\alpha+\gamma$. On further cooling to room temperature α orders to α_2. Alternatively, when an alloy(2) is quenched to a temperature below the α/α_2 order-disorder transformation temperature (T_o), α first orders to α_2 and then precipitation of γ takes place in α_2. But, when the α phase (alloy 3) is quenched to a region between the eutectoid temperature and the order-disorder transformation temperature, no ordering of α takes place without a change in its composition. According to Jones and Kaufman [18,60] "the pearlitic mode of transformation might be expected in this region". In this region, initially, the precipitation of γ takes place in disordered α and as the precipitation proceeds, the aluminum concentration of the matrix decreases. When the matrix composition crosses the T_o line, ordering of α to α_2 takes place. The cooling rate from the α phase field has also been found to have a significant effect on the decomposition of α phase and formation of α_2/γ lamellar structure.

2.2.3 $\alpha \rightarrow \gamma_m$ Massive Transformation

Fast cooling or quenching of titanium aluminide alloys, containing more than 46 at.% Al, from the α single phase field results in a microstructure containing lamellar regions as well as "massively" transformed regions of γ. Fig.2.12(d) shows that massive γ can form along with lamellar structure when the Ti-48Al alloy is rapidly cooled from α single phase field. Several others have also reported this transformation in alloys having Al contents greater than 46 at.%. and discussed the mechanism involved in the

transformation [60,62,68-71].

Mechanism of massive Transformation: The mechanism involved in the massive transformation has been dealt with in detail by Zhang et al [71] and Denquin and Naka [62]. However, the mechanism involved in massive transformation is not yet completely understood. It has been proposed that upon quenching, the α phase becomes unstable and begins to decompose to γ_1 (fcc) via the Blackburn mechanism. Since α phase frequently has few dislocations, there is a tendency for γ_1 to nucleate preferentially in the vicinity of particular grain boundaries which are able to supply Shockley partial dislocations and associated stacking faults. The γ_1 nuclei form coherent interface with one grain and tend to grow into the neighbouring grain. The interface between the growing γ_1 and the grain into which it is growing is incoherent which favours the transfer of atoms across the interface and hence the growth.

The growth is generally achieved by thermally activated short-range jumps of atoms across an incoherent interface. The γ_1 continues to grow and stops only when the α phase orders to α_2 or the growing front impinges on a transformed area. The disordered γ_1 subsequently orders to massive γ_m with $L1_o$ structure.

Effect of cooling rate and composition on massive transformation: The transformation of high temperature disordered α phase to massive γ_m phase requires very high cooling rates [60,72]. This transformation also depends on the composition of the alloy. The aluminum content of the alloy should be close to the stoichiometric

composition of TiAl. For the same type of quenching treatment, massive transformation takes place in the alloys with aluminum content between 46 to 50 at.% whereas this transformation does not take place for aluminum contents below 46 at.% [60,62,70-72]. Massive transformation has also been observed in a Ti-48Al-2Mn-2Nb alloy [73] and Ti-45Al-2Mn-2Nb [74].

2.2.4 Decomposition of β phase to B2 phase and ω or ω-type phases

The B2 phase is an ordered bcc phase. It forms due to ordering of the high temperature disordered bcc β phase. This ordering reaction has long been known in titanium alloys [36], and has also been found in Ti-25Al-xNb [68,69,75] and Ti_4Al_3Nb alloys [76-78].

The critical temperature, T_c, at which the high temperature β phase orders has not been accurately determined for the Ti-25Al-xNb systems. However, it has been suggested that the critical temperature increases with Nb content [75]. The addition of β stabilizing elements suppresses the martensitic transformation of β to α′ which orders to form α_2 and allows the retention of β phase at lower temperatures where the ordering reaction (β→B2) takes place.

The β→B2 ordering reaction has also been observed in a number of γ-based titanium aluminide alloys in the presence of β-stabilizing elements such as Nb and Ta [79-82]. It may be concluded that β-stabilizing elements expand the β phase field by extending it to higher aluminum contents and also by lowering the $\beta+\alpha_2$ phase boundary.

Frost *et al.* [83] first observed the formation of the hexagonal ω phase during rapid quenching of the disordered β phase in Ti and Zr alloys. Since then, ω or "ω-type" phases have been reported in many different alloy systems, especially, those containing ordered B2 phases [36,68]. Formation of "ω-type" phase in the B2 phase of certain Ti-Al-Nb alloys has also been identified [41,42]. The exact nature of ω and ω type phases are not yet established.

The "ω-type" phase is formed on rapid quenching from the β phase field. Strychor et al. [41] have suggested that the formation of this phase occurs by the collapse of $\{111\}_{B2}$ planes. This collapse results in an ordered ω-type phase having an orientation relationship; $\{111\}_{B2}//(0001)_{\omega\text{-type}}$ and $<110>_{B2}//<1120>_{\omega\text{-type}}$. On ageing, this phase undergoes secondary ordering reaction to produce ω″ and further ageing results in the precipitation of another ω-type phase with $B8_2$ structure [41,42]. Bendersky *et al.* [42] have suggested the sequence for this transformation as $B2 \rightarrow (\omega', \omega'') \rightarrow B8_2$. The ω-type phase with $B8_2$ structure is considered to be more stable than ω′ and ω″.

2.3 MICROSTRUCTURAL EVOLUTION DURING HEAT TREATMENT

Classification of microstructures: The microstructure of γ-based alloys can be classified into four groups: near gamma, duplex, nearly lamellar and fully lamellar [2,23,26,27,84,85]. The four types of microstructures observed in γ-based titanium aluminide alloys are shown in Fig.2.15 (a-d).

The near gamma microstructure consists of entirely gamma grains in single phase alloys or predominantly gamma grains with finely dispersed grain boundary α_2 particles in two phase alloys. The alloys containing more than 52 at.% Al, lie in the single phase γ field over the entire temperature range of heat treatment, and are single phase γ after cooling to room temperature. But, for alloys between 46 and 50 at.% Al, heat treatments at temperatures just above the eutectoid temperature yield a near gamma structure.

Duplex microstructure is typically the finest microstructure and is produced after annealing treatments in the α+γ phase field at temperatures where the γ and α phases are approximately equal by volume. When cooled to room temperature the duplex structure consists of equal proportions of equiaxed γ grains and γ/α_2 lamellar grains.

For the alloys containing less than 48 at.% Al, heat treatment at temperatures close to the α-transus (α/α+γ phase boundary) results in nearly lamellar microstructures that primarily consist of coarse lamellar grains with small amounts of γ grains. Lastly, heat

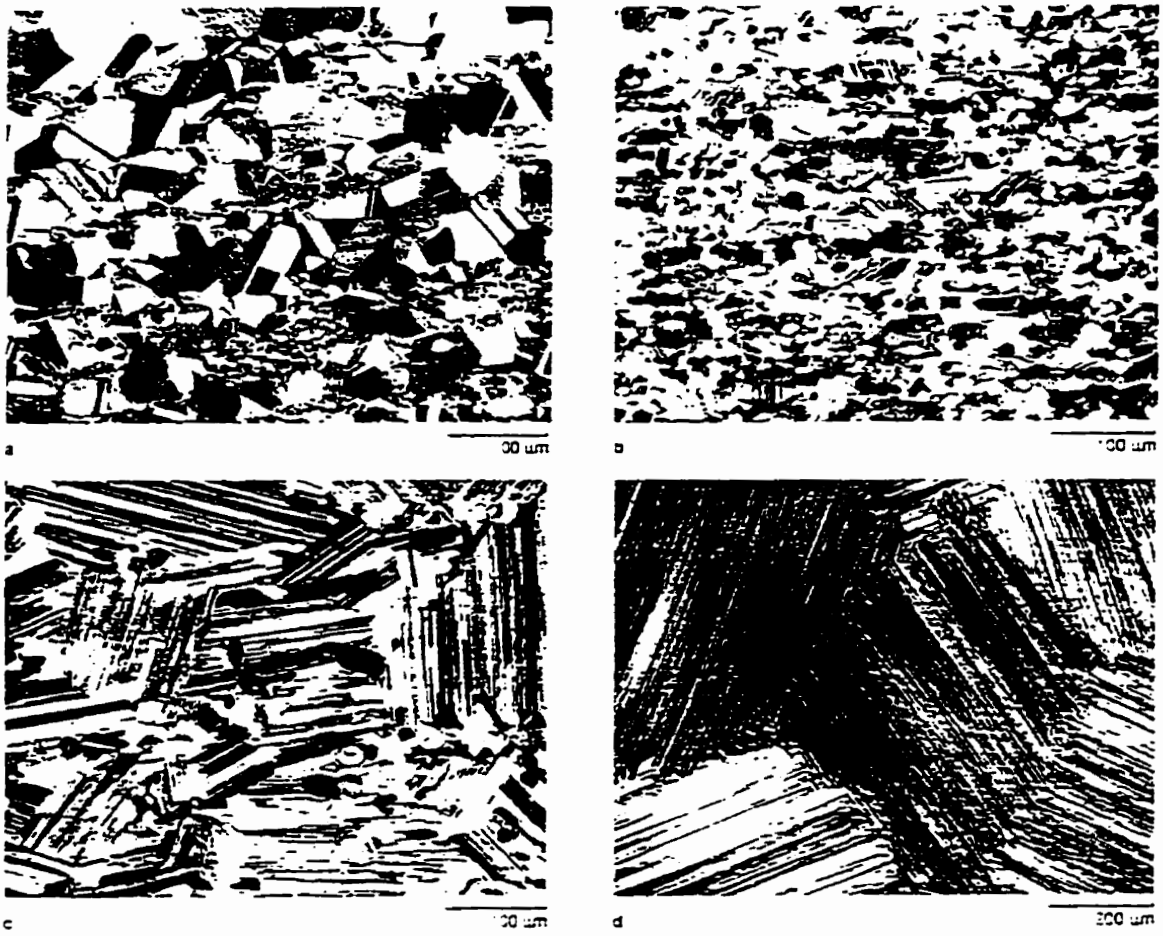

Fig.2.15 Four typical microstructures of gamma alloys: (a) Near gamma, (b) Duplex, (c) Nearly lamellar, and (d) Fully lamellar. [26]

treatments at temperatures above α-transus result in fully lamellar microstructures consisting of alternate layers of γ and α_2 plates. The lamellar grains have a relatively large grain size which reflects coarsening of α grains above the α-transus.

Three types of lamellar structures, designated; Type I, II, and III, have been identified through detailed microstructural development studies [27,86]. Types I and II structures are formed when the decomposition of high temperature α phase involves the precipitation of the gamma plates through reactions: $\alpha \rightarrow \alpha+\gamma \rightarrow \alpha_2+\gamma$ and $\alpha \rightarrow \alpha_2 \rightarrow \alpha_2+\gamma$, respectively. Both reactions result in alternating α_2 and γ plates having the orientation relationship $(0001)_\alpha // (111)_\gamma$ and $[2110]_\alpha // [110]_\gamma$. The fully lamellar microstructure and many of the nearly lamellar microstructures are of this type. Type II lamellar microstructures are typically observed in the duplex alloys and in low aluminum alloys (40-44 at.% Al) when cooled relatively fast [26]. Type III microstructures are formed by the growth of α plates in γ matrix when a hot worked two phase alloy is heated in the $\alpha+\gamma$ phase field. The resulting microstructure consists of alternating plates of α_2 and γ which have the usual orientation relationship. The only difference between the Types I and II, and the Type III is that in type I and Type II the γ plates are twin related whereas in Type III, the γ plates have the same orientation within a grain.

Processing and Microstructural Control: The γ-based alloys are processed by casting, ingot metallurgy, powder metallurgy and sheet forming methods. The cast microstructures in the casting process are normally fully lamellar with ocassional shrinkage pores and a small amount of pro-eutectoid γ phase. Hot isostatic pressing

(HIPping) is employed to remove the porosity. The ingot metallurgy process starts with ingot casting, followed by HIPping and /or a homogenization treatment and then hot working. HIPping removes shrinkage pores and also begins to homogenize the as-cast microstructures. Hot working is conducted near the eutectoid temperature in the case of forging or at higher temperatures for extrusion. Forging generally results in a banded structure consisting of a fine, partially recrystallized γ-grain matrix, dispersed with fine α_2 particles and some original lamellar grains which have survived hot deformation [84]. Extrusion at temperatures near the eutectoid temperature results in microstructures similar to, but less homogeneous than those produced by forging. Extrusion at higher temperature, where volume fractions of α and γ phases are equal, results in a fine duplex microstructure. Under certain conditions, high temperature extrusion yields fine, randomly oriented, fully lamellar grains with serrated boundaries. The γ-based alloys have been found to be difficult to roll [26,84]. Efforts are being made to make the rolling process easier.

The processed products are heat treated under appropriate conditions to develop the desired properties. The post processing heat treatments can be grouped into three schemes: I, II and III (Fig.2.16) [2]. Schemes I and II consist of annealing treatments and subsequent ageing treatments. Scheme III consists of ageing treatment only. The two step heat treatments, scheme I and II are used for hot worked materials having other than fully lamellar microstructure. Scheme III heat treatments are used when the as processed microstructures are not to be altered or are stable, as in the case of fully lamellar microstructures. Microstructure of γ-based alloys can thus be controlled by proper

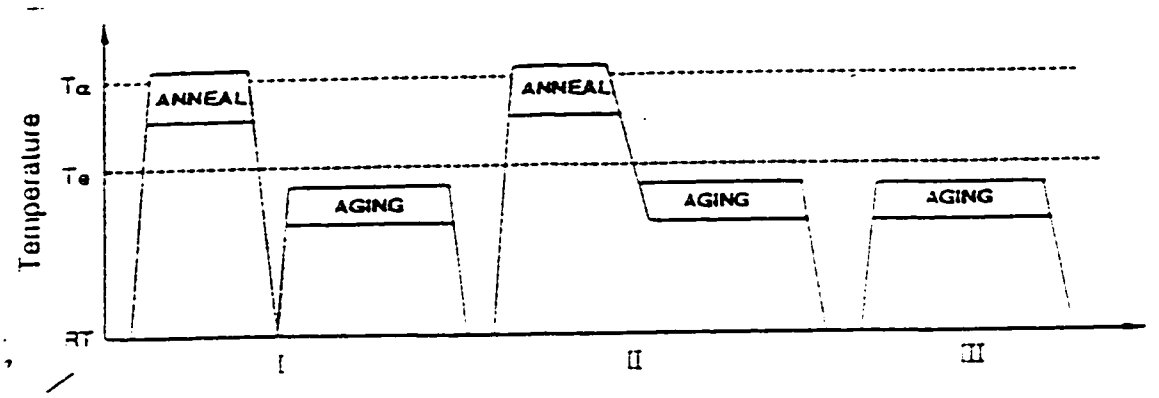

Fig.2.16 Three typical heat treatment schemes for gamma titanium aluminide alloys. All three can be used for wrought alloys, whereas cast products may need the scheme III treatment only. [27]

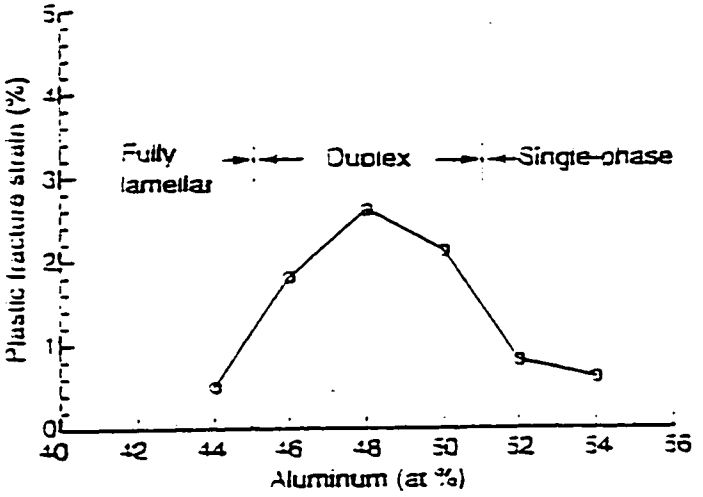

Fig.2.17 Variation of ductility with the microstructure type. [23]

processing and heat treatments. Microstructural control, generally, involves the control of relative proportion of the phases, grain size, grain boundary morphology and the interlamellar spacing in the lamellar structure.

Microstructure/Mechanical Property Relationships: Almost all mechanical properties, including the tensile properties, fracture toughness, creep and fatigue properties, strongly depend on microstructure of the alloy

The room temperature yield and ultimate tensile strengths vary from 250 to 990 MPa and 300 to 1030 MPa, respectively, depending on the alloy chemistry, processing, microstructure and grain size. The fully lamellar microstructure exhibits lower strength than the duplex structure. However, a decrease in grain size improves the tensile strength. A strong relationship between yield strength and grain size in the fully lamellar microstructure has been observed with a Hall-Petch constant, k ~5 $MPa(m)^{1/2}$ for grain sizes from 250 to 2600 μm, and yield strengths from 290 to 500 MPa [2,85]. The variation in strength with temperature also depends on the type of microstructure, with a better high temperature strength retention exhibited by a fully lamellar structure. The room temperature ductility of γ-based alloys varies from 0.3 to 4 % depending upon the alloy composition and the microstructure. The duplex alloys containing 45 to 50 at.% Al show appreciable ductility and the value of ductility is maximum for duplex alloy with 48 at.% Al (Fig.2.17) [23]. Ductility also depends on the grain size. The highest ductility is obtained in fine grained duplex microstructure. Fig.2.18 [2,4,27] shows the stress-strain curves for different grain size microstructures. It can be concluded that the fully lamellar

structure exhbits lower strength and ductility as compared to the duplex srtucture. The poor tensile properties of a fully lamellar structure have been attributed to large grain size [87], lack of slip/twinning activity [87], and low cleavage stresses [88].

The fully lamellar γ-based alloys exhibit highest fracture toughness ranging from 25 to 30 $MPa(m)^{1/2}$ [2]. The alloys with duplex microstructure have a toughness of ~ 15 to 20 $MPa(m)^{1/2}$ and the single phase γ alloys exhibit the lowest fracture toughness of ~10 $MPa(m)^{1/2}$ [2]. It has been suggested that the duplex microstructure exhibits small plastic strain at the onset of crack extension and no resistance to crack propagation, whereas, the fully lamellar structure shows crack-tip plasticity and increased resistance to crack propagation [89]. The fracture toughness of the lamellar structure depends on the orientation of the lamelae relative to the crack plane [90-92]. Highest toughness values were obtained when the crack was forced to traverse across the lamellar than when the crack growth was along the lamellar interfaces. The relation between microstructure, grain size , fracture toughness and tensile properties are shown in Fig.2.19.

Fully lamellar γ-based alloys exhibit better creep resistance than duplex or nearly lamellar alloy [93,94]. Beddoes *et al.* [93] reported that reducing the lamellar grain size improved creep resistance whereas, it was observed by Keller *et al.* [95] that the larger lamellar grains were associated with improved creep resistance. However, it has been recently [96] predicted that the lamellar grain size has no significant effect on creep resistance. Serrated grain boundary morphology also appear to increase the creep rupture life of a fully lamellar structure alloy [49,97].

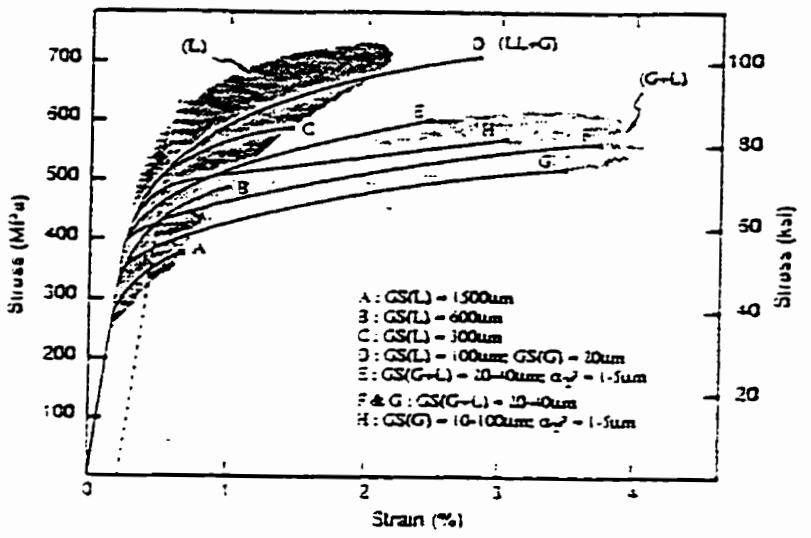

Fig.2.18 Room temperature stress-strain curves for; fully lamellar (L), nearly lamellar (LL+G), duplex (G+L), and equiaxed gamma microstructures. [26]

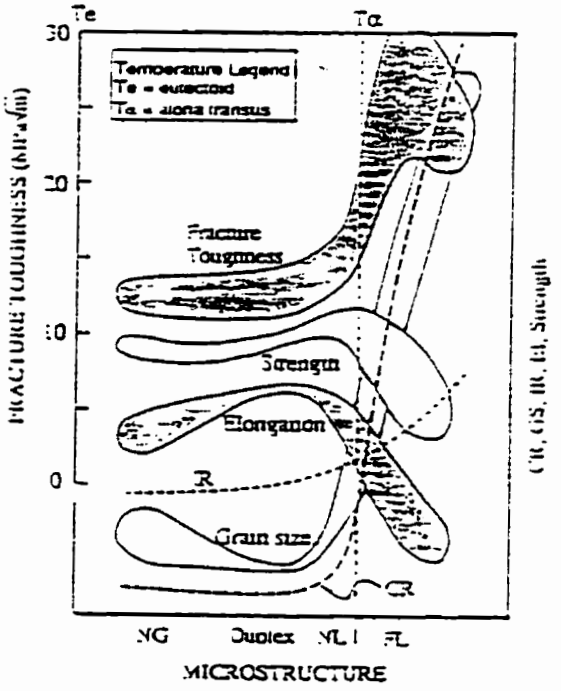

Fig.2.19 Schematic relationship between microstructure and grain size and mechanical properties including fracture toughness, tensile strength and elongation (El), impact resistance (IR) and creep resistance (CR). [2,26]

Duplex microstructures exhibit longer low cycle fatigue life than fully lamellar microstructures below 850°C [2,26]. For high cycle fatigue, duplex microstructures show better fatigue properties at lower temperatures, but fully lamellar structures exhibit longer lives at higher temperatures [2]. However, when the applied stress is normallized by the ultimate tensile strength, the duplex and lamellar alloys exhibit essentially identical fatigue lives at a given value of the normallized stress [100]. Fatigue behaviour of the fully lamellar alloys is a function of the inter-lamellar spacing. It has been reported that smaller interlamellar spacing increases the fatigue-crack-initiation life [101]

In summary, the fully lamellar microstructure consisting of large lamellar grains produces improved toughness and creep resistance, but poor tensile properties, while the duplex microstructure consisting of fine equiaxed γ and lamellar grains yields good tensile properties, but poor toughness and creep resistance. The tensile properties of fully lamellar microstructure can be improved by reducing the grain size. An optimum balance of all the mechanical properties can be achieved by controlling the proportions of equiaxed γ and lamellar grains and also by controlling the grain size.

2.4 OXIDATION RESISTANCE

Effect of temperature on oxidation behaviour: The oxidation resistance of titanium aluminides proceed in four characteristic modes depending upon the oxidation temperature [102] as illustrated in Fig.2.20. Mode I occurs at ambient temperatures with the formation of a thin titanium oxide layer. Some alumina has also been observed to form at these low temperatures [12]. Mode II occurs at higher temperatures upto 800°C with the formation of an alumina scale with some titania. The alumina formed in this mode completely covers the surface and offers rapid passivation, thus, minimizing the oxidation rate. At temperatures between 800 and 1100°C, the oxidation rate constants increase by several orders of magnitude and mode III occurs with the formation of a tri-layer scale. There is an outward growing TiO_2 layer, an inward growing two phase TiO_2/Al_2O_3 layer, and a stationary Al_2O_3 layer at their interface. Finally above 1100°C, mode IV occurs which is accompanied by internal oxidation resulting in even more rapid deterioration of the alloy. During service, the alloys are subjected to the temperatures in the temperature range corresponding to mode III. Oxidation rates during mode III are excessively high, causing rapid degradation of the material. It has also been reported that at temperatures below 850°C (e.g., 760 and 815°C), the oxide scale is adherent to the matrix whereas it spalls a little at a temperature of 870°C [13].

Effect of aluminum content: The oxidation rate decreases with increase in aluminum content but the morphology of the multilayered oxidized scale does not change [10].

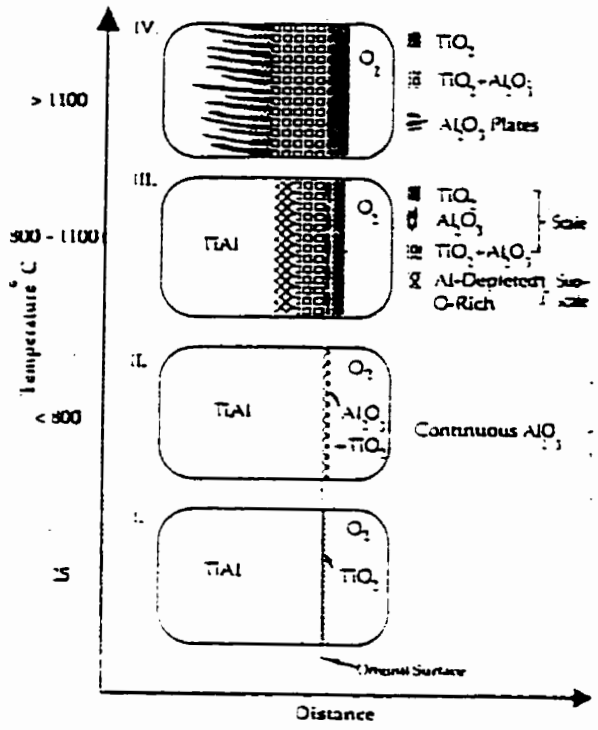

Fig.2.20 Schematic diagram showing four oxidation modes of γ-based titanium aluminides. [12]

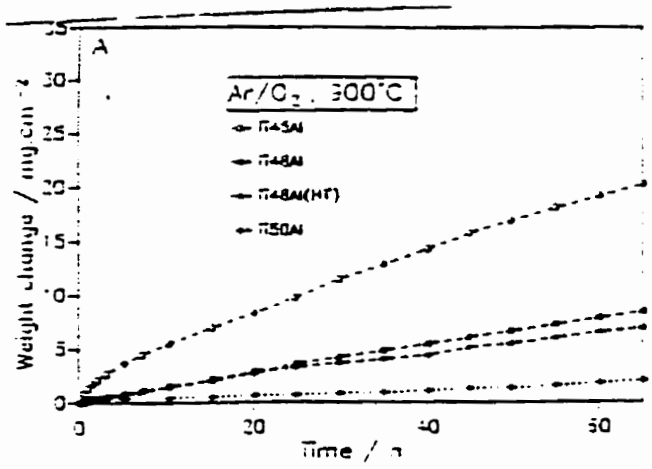

Fig.2.21 Mass gain as a function of time. [10]

However, the ratio of the thickness of outer TiO_2 and inner TiO_2/Al_2O_3 layers decreases with increase in Al content. Fig.2.21 [10] shows the result of oxidation of alloys containing 45, 48, and 50 at.% Al at 900°C in an atmosphere of argon containing 20 % oxygen. It was also found that a reduction of aluminum content of the alloy from 50 to 48 at.%, increases the oxidation rate by approximately a factor of four.

Effect of oxidizing atmosphere: In 100 % oxygen atmosphere, the gamma based titanium aluminides have good resistance to oxidation and show alumina forming kinetics upto 950°C. In air, however, the alloy oxidizes at a more rapid rate because of the formation of TiO_2 rich scale which grows at rates much faster than the alumina scale [53,104]. This effect was first shown by Choudhury *et al.* [105] who studied the oxidation of TiAl (50 at.% Al) in oxygen and air over the temperature range of 800 to 1200°C. Experiments to determine the species responsible for the difference between exposures in oxygen and air indicated that CO, CO_2 and H_2O impurities were not responsible. It was concluded that nitrogen was responsible for the increased rate of oxidation in air although no nitrogen containing phases were indentified in the scale. Similar observations have been made in a number of investigations [106]. It has also been observed that approximately 60-70 at.% Al is required to form a continuous layer of Al_2O_3 in air whereas only 47-49 at.% Al is needed in pure oxygen [10].

When γ-TiAl is oxidized in air, the presence of oxygen has been shown to result in the formation of intermixed layer of TiN and Al_2O_3 on the alloy surface which prevents the development of a continuous alumina layer [109]. TiN oxidizes to produce TiO_2 and

releases nitrogen which reacts to produce more TiN. TiO_2 provides an easy path for the transport of Ti, Al as well as oxygen atoms. Consequently the oxidation rate is increased.

Effect of partial pressure of oxygen: The oxidation resistance of titanium aluminides also depends on the partial pressure of oxygen in the oxidizing atmosphere [13,103]. Oxidation at ~1000°C in a low air pressure of $\sim 10^{-3}$ Pa yields a thin and dense alumina scale.

Improvement of oxidation resistance: The most widely used method for improvement of the oxidation resistance of titanium aluminides is by adding an alloying element. The alloying additions help in forming a continuous and protective Al_2O_3 rich layer by either reducing the rate of formation of TiO_2 or by suppressing the internal oxidation of Al to form discrete alumina platelets or by the formation of a barrier layer. Ternary and higher order alloying additions can reduce the rate of oxidation of γ-alloys [13,26,53,105,107-109]. Of particular benifits are small (1-4 %) ternary additions of tungsten, niobium and tantalum [26,105,110]. When combined with quarternary additions of 1-2 % chromium or manganese, further improvement in oxidation resistance has been observed [110]. Addition of Hf and Zr has also been found to improve the oxidation resistance significantly even under cyclic conditions with temperature varying between room temperature and 1300K for at least 100 cycles [111]. Besides these alloying additions, P and Y are also reported to improve oxidation resistance of γ-alloys [23]. A small addition of Si has been reported [55] to be effective in decreasing the oxidation rate by forming discrete SiO_2 aggregates in the scale/substrate interface. The SiO_2-rich layer works as a

barrier to further oxidation.

Several surface treatments have also been developed for improving the oxidation resistance of γ-alloys. One such surface treatments is the surface application of Nb by ion implantation [101]. It is very effective in forming a protective Al_2O_3 scale on TiAl. Heat treatment at ~1000°C in a low air pressure (5×10^{-3} Pa) yields an external alumina scale of about 1 μm thickness. The oxidation resistance of a structure controlled Ti-46.5Al-2.1Cr-3.0Nb-0.2W was found to be greatly improved by this treatment [13]. Yoshihara *et al.* [103] suggested that a combined treatment consisting of the above surface treatment followed by diffusion coating with aluminum shows excellent resistance to cyclic oxidation. The diffusion coating of the specimens was performed by a powder pack method at a temperature of 730°C for 10 hrs using a mixture of Al, Al_2O_3 and NH_4Cl with a composition of 25.0:73.5:1.5.

A series of Ti-Al-Cr oxidation resistant coating alloys has also been developed [108]. Sputtered Ti-44Al-28Cr coating is shown to successfully protect Ti-47Al-2Cr-2Ta under long term cyclic oxidation at 900°C in air [112]. Coating composition optimization studies [108] identified Ti-50Al-20Cr as holding the most promising oxidation resistant coating for γ-alloys. However, the best current option of reducing Ti-Al-Cr coating alloy brittleness is to base the alloy on the γ phase[113,114].

2.5 SURFACE DAMAGE DURING HEAT TREATMENT

Zheng *et al.* [11] have reported a two phase depletion layer formation during oxidation of Ti-48Al in Ar+20 % oxygen at 900°C. Qualitative electron probe micro-analysis showed that one of the phases had higher Al and O concentration. On the other hand, when Ti-50Al was oxidized for 24 hrs at 900°C in Ar+20 % oxygen, a single phase depletion layer was formed. Single phase depletion layer was also formed in ternary alloy Ti-48Al-5Cr. Based on the X-Ray diffraction data, it was suggested that one phase was α_2 and the other was a new Z phase. This Z phase can be related to cubic lattice with a=0.69 nm. By wavelength dispersive spectrometry, it was also found that Z phase contained more oxygen than α_2.

The existence of two phases in the depletion layer beneath the mixed titania/alumina scale was also reported by Beye and Gronsky [102]. Later, Beye *et al.* [12] characterized the two phase depletion layer by electron microscopy and microanalysis. The alloy used by them was Ti-47 at.% Al which was annealed in oxygen at 1000°C for 24 hrs. The depletion layer was found to consist of two phases: one hexagonal with unit cell dimensions a=0.5nm, c=0.47nm, and a composition close to $Ti_6Al_3O_4$ and another a simple cubic with a=0.69nm and composition $Ti_3Al_2O_3$.

Change in microstructure has also been observed during heat treatment of titanium aluminides of varying compositions but this aspect has not been dealt in detail. Baeslack

et al. [9] observed a completely lamellar structure at the outer edge of the specimen when a Ti-48Al-2Mn-2Nb alloy was forged and then vacuum heat treated at 1300°C for 4hrs. This change in microstructure was attributed to either loss of Al, or increase in oxygen experienced during heat treatment. No detailed analysis was done to explain the change in microstructure.

A change in microstructure at the outer edge of the specimen was also observed during vacuum annealing of Ti-47Al after annealing for 1 week at 800°C [8]. Beneath the cut surface of the sample, a layer of recrystallized γ grains was observed in many regions. This was assumed to be the effect of near surface deformation introduced during specimen cutting. After ageing for one week at 1000°C, α case was found to be formed at the edge of the specimen. At 1200°C, a thick (60-100 μm) layer of equiaxed γ grains was observed to be formed. The layer beneath the cut surface of the specimen was referred to as "damaged layer". However, there is a lack of information about the mechanism operative in the change in microstructure at the outer edge during various heat treatments.

2.6 SCOPE OF PRESENT INVESTIGATION

In summary, γ-based titanium aluminides have attracted a great deal of attention from the aerospace community and the automobile industry ever since they were first identified by the U.S Air Force as potential candidate for jet engines. The γ-based titanium alumindes have attractive properties for high temperature structural application, such as high temperature strength retention, good oxidation resistance and low density. Titanium aluminides also have some drawbacks: low ductility and low fracture toughness. However, attempts are being made to overcome these drawbacks by appropriate thermal and thermo-mechanical treatments. These treatments require exposure of the material to high temperature for longer periods of time.

As shown in the preceding sections of literature review, changes in microstructure have been observed during various heat treatments [8,9] and also during oxidation in air/oxygen at various temperatures [10-13]. However, there is a lack of information regarding the mechanism operative in such microstructural changes.

Keeping this background in view, the present investigation was undertaken in order to acquire comprehensive understanding of the mechanism involved in surface damage during heat treatment, and also to rationalize the presence of various phases in the damaged layer. The Ti-45Al-2Mn-2Nb alloy was used and the effect of annealing at 1200°C and oxidation at 850°C on the changes in composition and microstructure of the material was studied

Chapter 3
EXPERIMENTAL PROCEDURES

3.1 MATERIAL

The material used in the present study was a γ-based titanium aluminide with the nominal composition of Ti-45Al-2Mn-2Nb (all compositions in atomic %). The material was cast and then HIPped at 1250°C and 172MPa pressure for 4 hours. The alloy was prepared and supplied by Howmet Corporation in the form of slabs of 1.2 cm thickness.

3.2 SAMPLE PREPARATION AND HEAT TREATMENT

Small cuboid samples of size 12mm x 8mm x 5mm were cut from the cast and HIPped slab by electric discharge machine. These cuboid samples were wrapped in Ta foil, which serves as a getter for oxygen, and then sealed in vycor capsules backfilled with 160 torr of commercial argon. The vycor capsules containing alloy samples were then placed in a horizontal tube furnace with alumina refractory lining. The temperature of the furnace was maintained constant at 1200°C (with an accuracy of ±5°C). The encapsulated samples were annealed at 1200°C for varoius periods of time, viz. 15 hrs, 30 hrs, and 50 hrs. The vycor capsules containing alloy specimens were air cooled following the annealing treatment. Samples were then released by breaking the capsules and unwrapping the Ta foil. Two specimens, one wrapped in Ta and the other without Ta wrapping, were also annealed at 1200°C for 25 hrs.

3.3 OXIDATION TEST

Oxidation tests were carried out at 850°C in air to study the effect of service environment

on the stability of microstructure beneath the oxide scale. The samples used were of the same size and shape as those used for heat treatments. Before oxidation the samples were ground with 1200 grit abrasive paper and cleaned with alcohol.The samples were then exposed to air at 850°C for 7 days and 15 days.

3.4 SCANNING ELECTRON MICROSCOPY

The samples for SEM investigation were prepared by cutting the heat treatted specimens by electric discharge machine as shown in Fig.3.1. The cross section samples were ground with 1200 grit abrasive paper and then polished with 6μm and 1μm diamond paste. The microstructure of the as received material and the heat treated materials were studied using JEOL-840 scanning electron microscope in back scattered electron mode. The cross sections of oxidized samples were observed both in back scattered and secondary electron mode. Concentration profile of Al in the depletion layer was determined by measuring the Al content as a function of depth from the outer edge of the sample. All the SEM/EDS x-ray aquisition were done with a JEOL-EDS system equipped with a Tracor Northern 5500 multichannel analyzer. All the SEM/EDS spectral quantification for the determination of concentration profile were done using the Micro-Q software (supplied by Tracor Northern), which incorporates ZAF correction and deconvolution of the overlapped peaks from acquired spectral standards of the elements of concern by using pure metal standards. X-ray line scanning was done to obtain the distribution of Al, Mn and Nb in the damaged layer. SQ software was also used for quantification of EDS spectrum obtained from various locations in the cross section of the Ta foil and also of the oxidized specimen. This software uses built-in standards.

3.5 TRANSMISSION ELECTRON MICROSCOPY

Thin foils were prepared to characterize the Al-depletion layer in TEM. One mm thick

slices were cut from the surface of the heat treated specimens using the electric discharge machine and were then reduced to ~100μm thickness using 600 grit abrasive paper. 3 mm diameter discs were punched out and were further thinned and polished using twin jet polishing unit. The electrolyte used for twin jet polishing was a solution of 5 % perchloric acid, 30 % but-1-enol, and 65 % methanol. Twin jet polishing was carried out at –30°C to –35°C and 30 volts.

The thin foils were examined in JEOL-2000X TEM, operated at 200 KV. This was done to characterize the depletion layers formed during heat treatment of the alloy at 1200°C for various periods of time. The microstructural characterization of the depletion layer was done by bright and dark field imaging, and SADP. Chemical composition of each phase present in the depletion layer was measured by TEM/EDS. The EDS was equipped with a high purity Ge detector and Tracor Northern 5400 system.

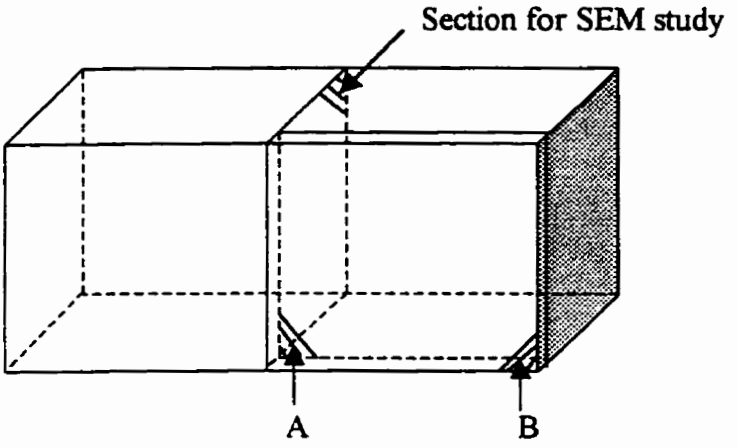

Fig.3.1 Schematic sketch of the specimen showing section for SEM study and thin foil preparation. Thin foils were prepared by grinding off the surface A or B of the sample cut from the specimen. All the outer surfaces of the specimen were damaged.

Chapter 4

RESULTS

4.1 MICROSTRUCTURE AND COMPOSITION OF THE AS RECEIVED MATERIAL

Fig.4.1 shows the microstructure of the as received material. It consists of primarily a lamellar micro-constituent. The lamellae are known to be of the γ phase and the α_2 phase. In addition to the lamellar constituent, a small volume fraction of the γ phase in between the lamellar grains is also present. The lamellar structure appears to have a range of interlamellar spacing. However, this is likely to be due to the relative orientation of the lamellae with respect to the polished surface.

In order to obtain the bulk composition of the as received material, EDS analysis was performed in scan mode in which areas of about 100μm x 100μm on the specimen were scanned. The average composition of the bulk was then obtained by quantification of the EDS spectrum acquired from these areas. Micro-Q software was used for the quantification of the spectrum. Such analysis was carried out at six different random locations showing lamellar structure. The results of the analysis are given in Table 4.1 along with the scatter in each value. The scatter in these values are not appreciable. The analyzed composition is consistent with the nominal composition of 51% Ti, 45% Al, 2% Mn and 2% Nb (all compositions in at.%).

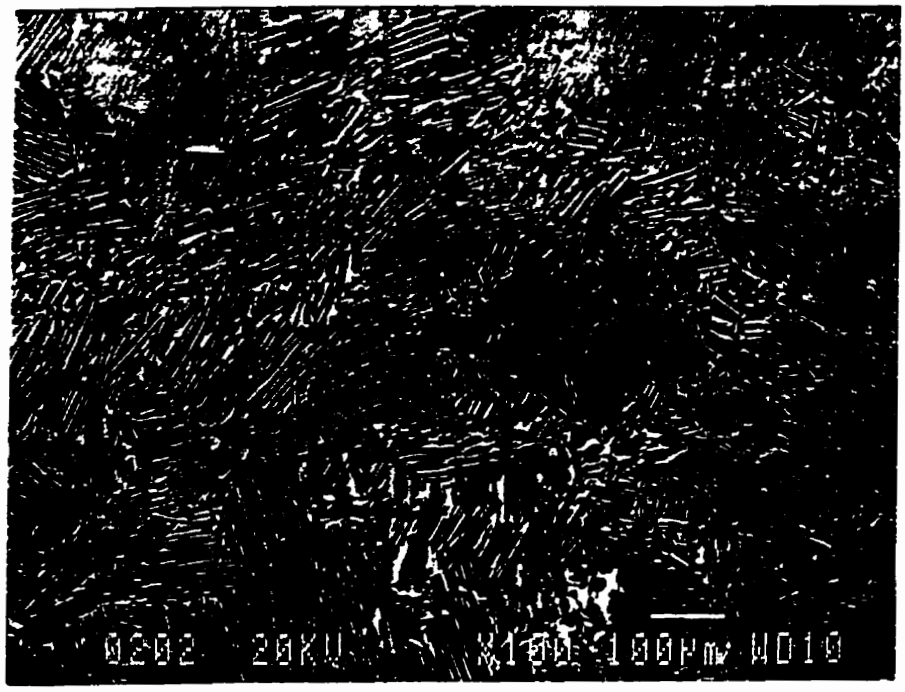

Fig.4.1 As received microstructure showing lamellar ($\gamma + \alpha_2$) structure with patches of γ (black regions) in between the lamellar grains

Element	Concentration (wt.%)
Titanium	51.07 ± 0.335
Aluminum	45.16 ± 0.558
Manganese	1.72 ± 0.027
Niobium	2.06 ± 0.0522

Table 4.1. Average composition of the as received material

4.2 DAMAGE OF ALLOY SPECIMENS DUE TO ANNEALING AT 1200°C

The vycor capsules, in which the specimens were sealed with tantalum foils under argon, did not give any evidence of change of shape after annealing at 1200°C. The samples were released by breaking the vycor capsule. No deposits were found on the inner walls of the capsule and also no loss of transparency of the tube was observed. It is thus evident, that the glass remained chemically inert during the high temperature annealing. The Ta foil was unwrapped to release the specimen. The foil appeared to have retained its ductility, however, the outer surface of the foil lost its metallic lustre. Shiny, metallic particle like deposits were observed on the inner surface of the foil that was exposed to the sample. Fig.4.2 shows the photograph of the tantalum foil before heat treatment and the inner and outer surface of the foil after heat treatment.

The cut surface of the specimen, particularly those obtained by silicon carbide wheels, were bright and shiny prior to the high temperature annealing. However, after annealing all the surfaces felt rough to the touch and appeared to have a thin brown adherent surface layer suggesting surface damage. Fig.4.3 shows the photograph of the surface of a specimen before and after the high temperature annealing.

The alloy specimens were weighed before the heat treatment and also after the heat treatment. The data listed in Table 4.2 show that the specimens lost weight following the

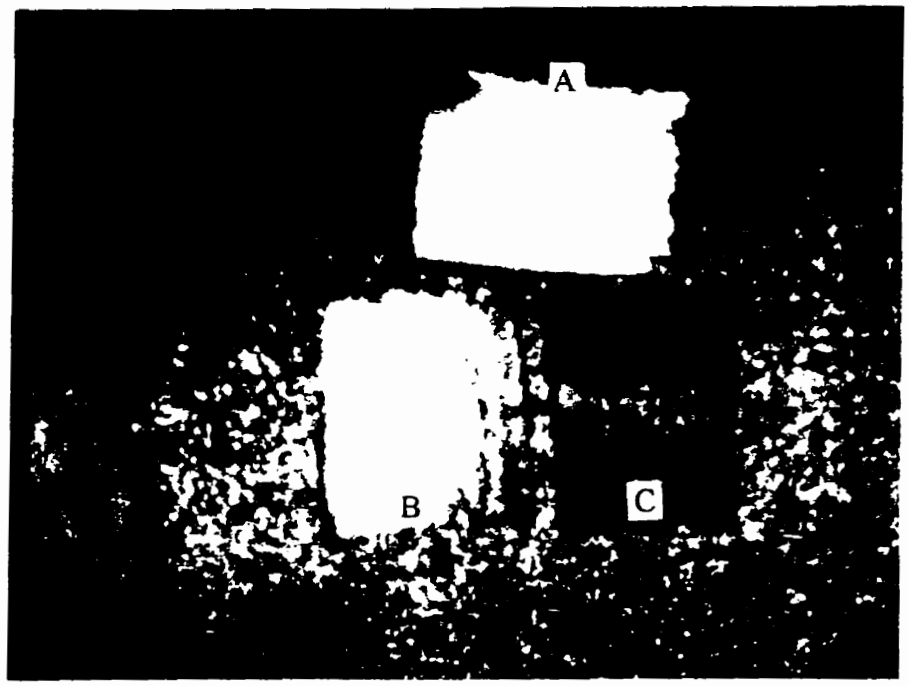

Fig.4.2 Photograph of the Ta foil before heat treatment (A) and the inner (B) and outer (C) surface of the foil after heat treatment.

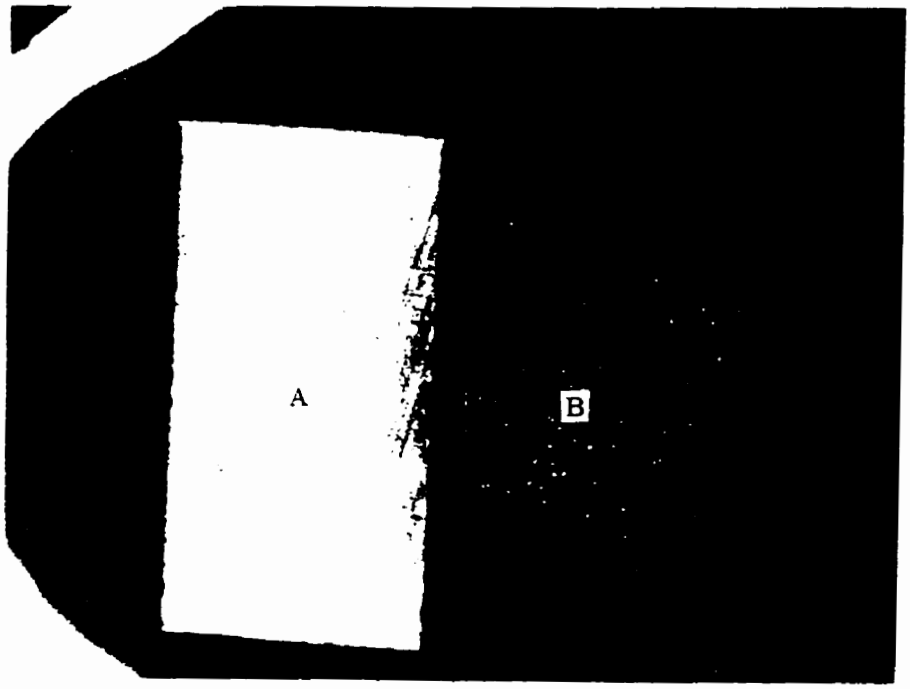

Fig.4.3 Photograph showing specimen surface before heat treatment (A) and after heat treatment (B).

Heat Treatment Time (hrs)	Weight (gm)		
	Before H.T	After H.T	Weight loss
15	1.9387	1.8987	0.0400
30	1.4054	1.3431	0.0623
50	1.5116	1.4480	0.0636

Table 4.2. Weight loss data for the three different times

Heat Treating Time (hrs)	Thickness of damaged layer (μm)
15	90
30	120
50	145

Table 4.3. Thickness of damaged layer measured as a function of heat treating time

heat treatment. These results show that the specimens lost some of the components through their exposed surfaces and suffered the surface damage. An appreciable decrease in thickness was also observed in the specimen that was heat treated at 1200°C for 50 hrs. The thickness of the specimen before heat treatment was 9.06mm and it decreased to 8.97mm after heat treatment, the net decrease in thickness was, thus, 0.09mm.

4.3 THICKNESS OF THE DAMAGED LAYER

The three specimens that had been sealed with tantalum under exactly the same argon pressure, were annealed at 1200°C for 15, 30 and 50 hrs. The cross sections of these annealed specimens were examined in the SEM in the BSE mode. The BSE images are shown in Figs. 4.4-4.6 . The interior of each of the specimen exhibits the typical lamellar structure. However, the region near the outer surface does not show any lamellar structure. This damaged layer has two distinct regions. The region next to the lamellar structure appears gray and the region beyond the gray region appears white. The white region extends upto the outer most surface of the specimen. However, the boundary between the gray region and the white region is highly irregular. By comparing Fig. 4.4, 4.5, and 4.6, it is seen that the damaged layer thickness increases with the increase in annealing time. Table 4.3 lists the thickness of the damaged layer as a function of time.

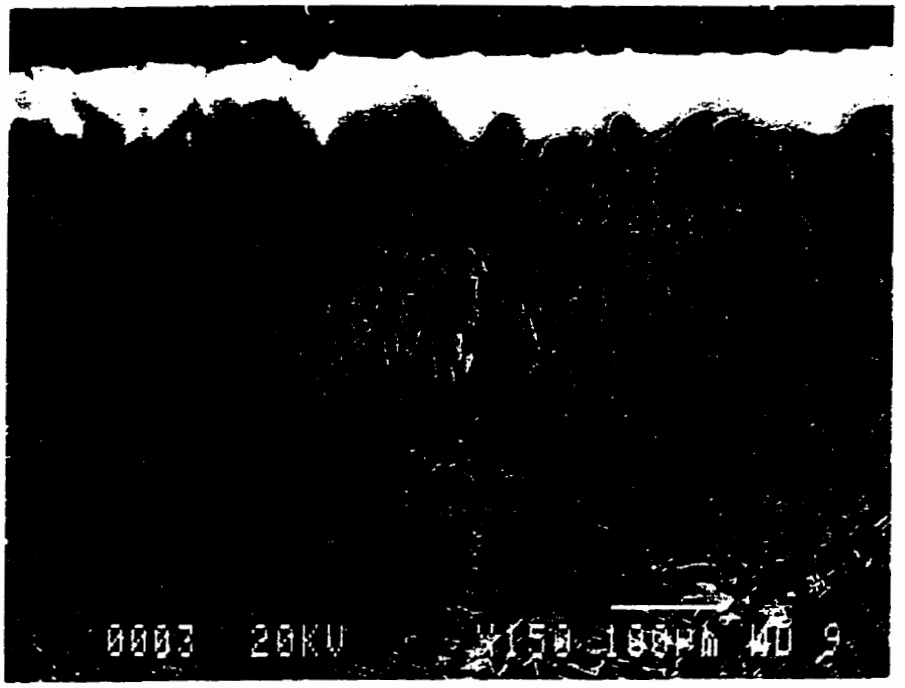

Fig.4.4 Back scattered electron image of cross section of the specimen annealed for 15 hrs at 1200°C.

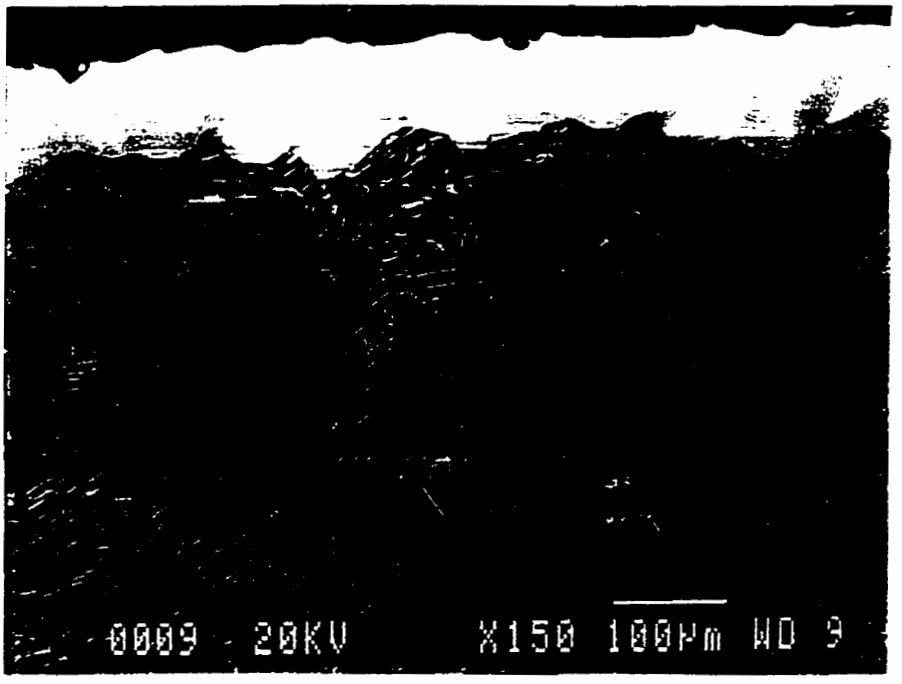

Fig.4.5 Back scattered electron image of cross section of the specimen annealed for 30 hrs at 1200°C.

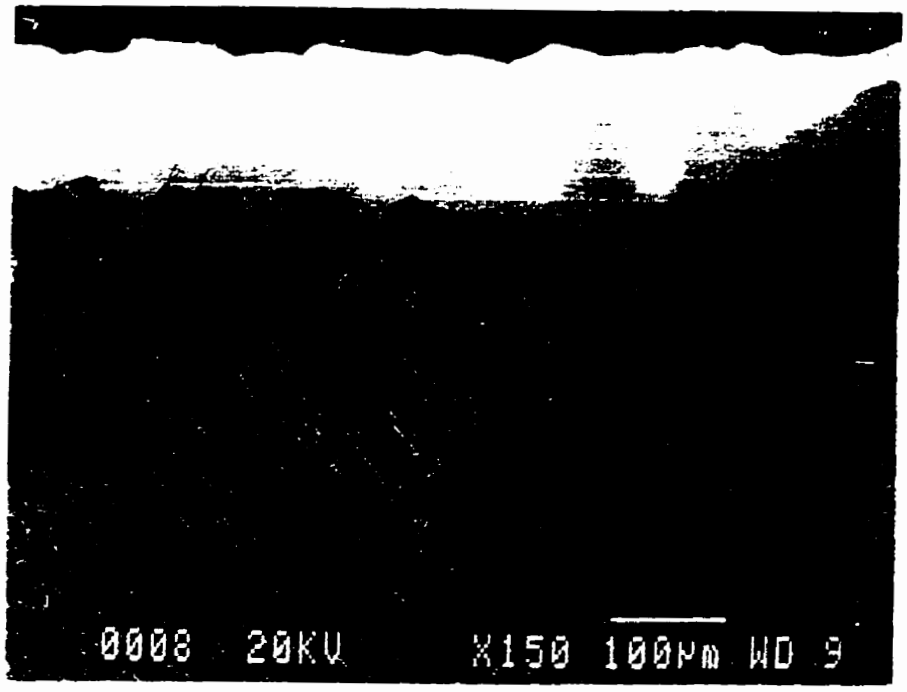

Fig.4.6 Back scattered electron image of cross section of the specimen annealed for 50 hrs at 1200°C.

4.4 CONCENTRATION PROFILE OF SOLUTES IN THE DAMAGED LAYER

Concentration profiles of aluminum in the damaged layers were obtained by measuring the Al content in the layer as a function of depth from the "outer edge" of the specimen. All EDS quantifications were done using the Micro-Q software. Figures 4.7-4.9 show the aluminum concentration profile in the damaged layer of the specimens heat treated for the three different periods of time. It is seen that the Al content of the damaged layer increases with distance from the outermost surface of the specimen. It is highest at the depletion layer/bulk interface and decreases as the distance from this interface increases towards the outer edge of the specimen. Although the damaged layers show two regions, gray and white, the composition profile of aluminum does not show any discontinuity at the gray/white phase interface.

Fig.4.11 shows the distribution of the three solutes, manganese, niobium and aluminum, along the line AB shown in Fig.4.10. There is a continuous increase in Al content with the increase in distance from the outer surface of the specimen. However, the Mn and Nb contents show a sharp decrease at the white/gray phase interface. Fig.4.12 shows the distribution of the three solutes Mn, Nb, and Al, along the line marked XY in Fig.4.10. At a particular distance from the outer edge of the specimen, Al content is the same, whereas, Mn and Nb concentration is higher in the white phase than the gray phase.

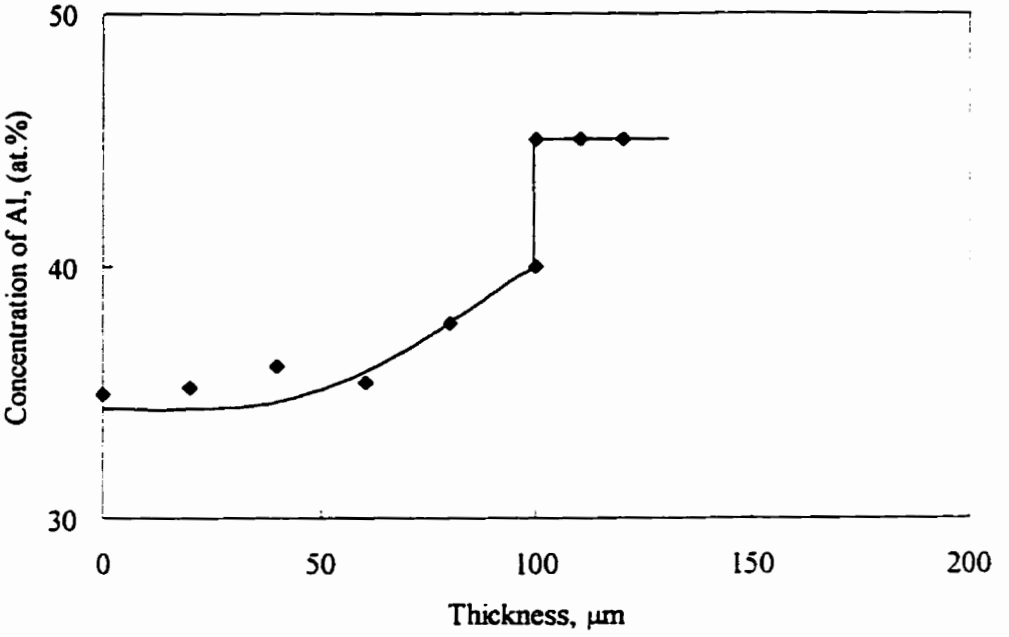

Fig.4.7 Concentration profile of Al in the damaged layer after 15 hrs of annealing.

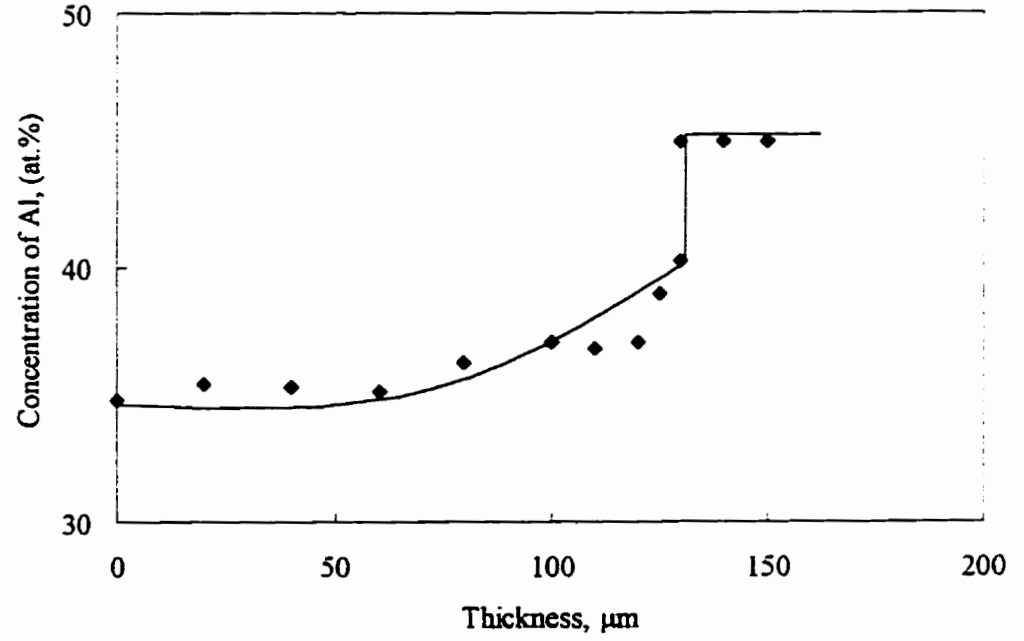

Fig.4.8 Concentration profile of Al in the damaged layer after 30 hrs of annealing.

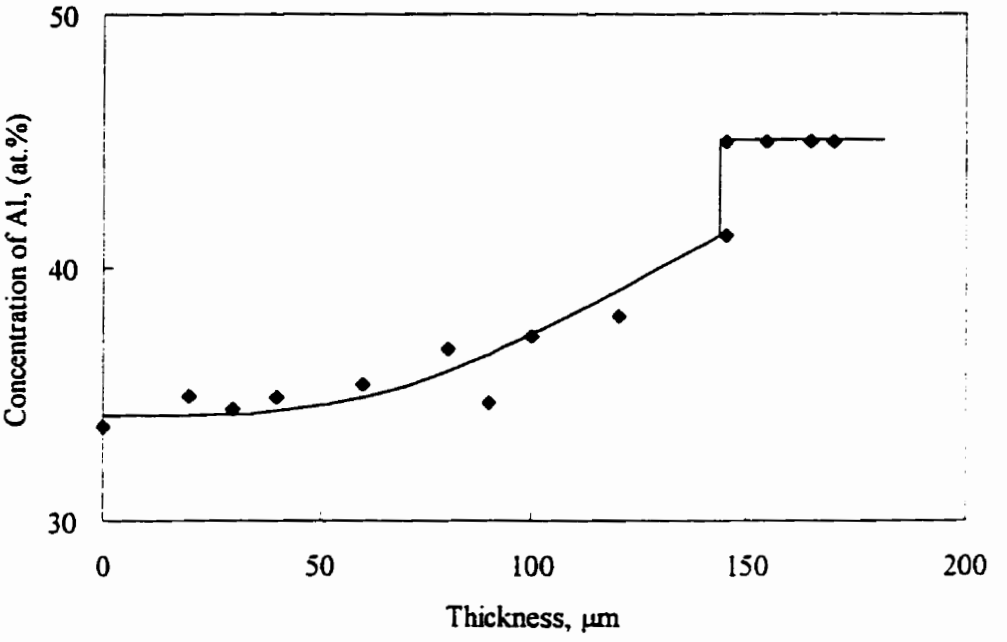

Fig.4.9 Concentration profile of Al in the damaged layer after 50 hrs of annealing.

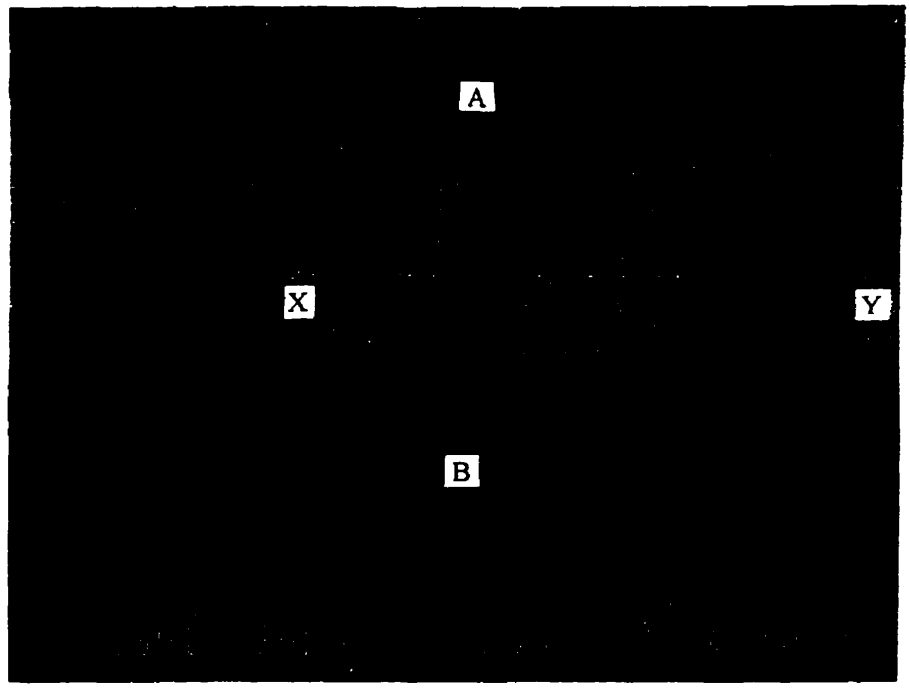

Fig.4.10 Back scattered image of the damaged layer. The diagram shows two lines AB and XY along which the distribution of elements was determined by line scanning.

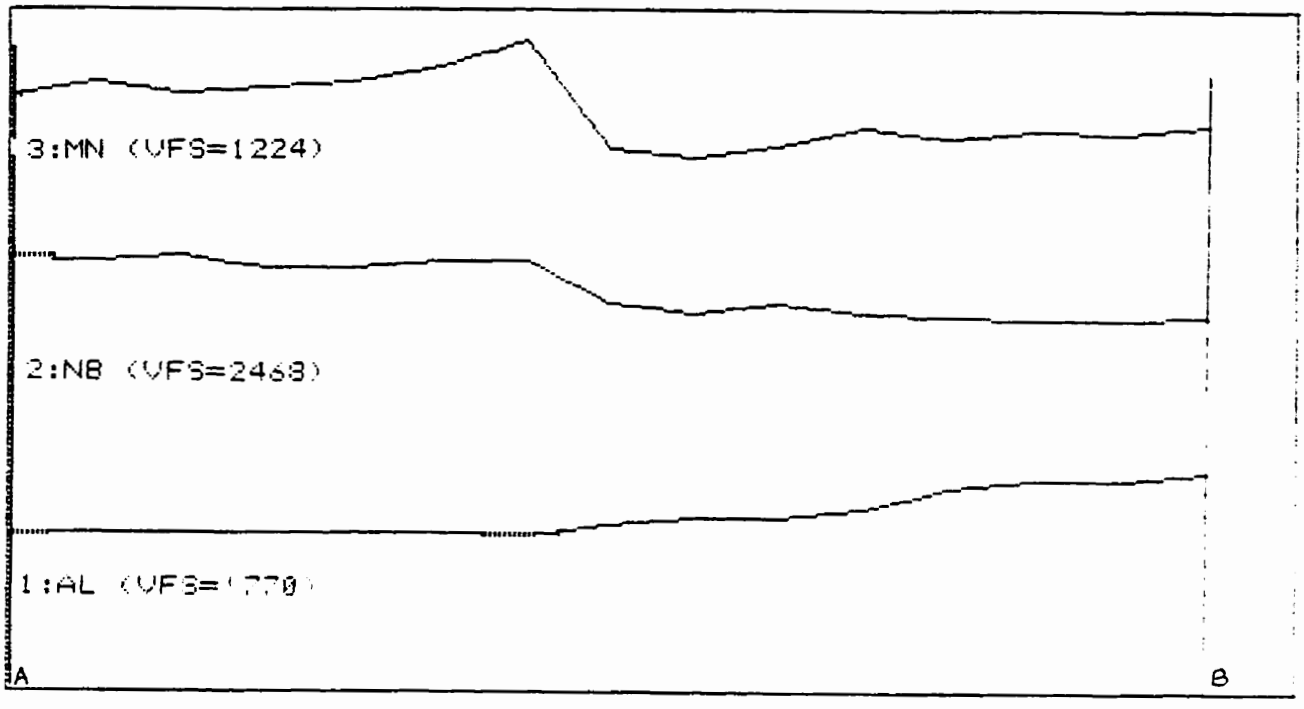

Fig.4.11 Distribution of the alloying elements Mn, Nb, and Al along the line AB shown in Fig.4.10.

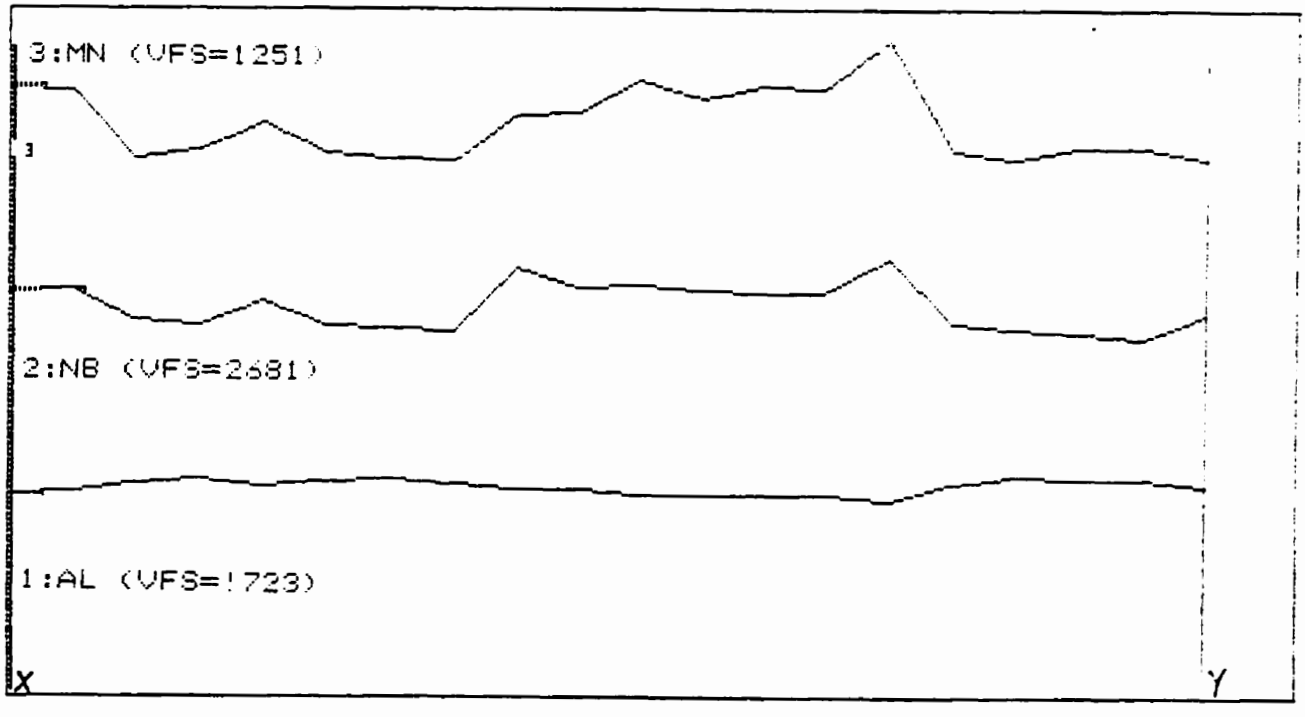

Fig.4.12 Distribution of the alloying elements Mn, Nb, and Al along the line XY shown in Fig.4.10.

4.5 MICROSTRUCTURAL CHARACTERIZATION OF THE DEPLETION LAYER

Different regions of the damaged layer was found to consist of different phases. These phases were identified by detailed investigatrion of the thin foils representing these regions.

Fig.4.13 shows the bright field image of the region close to the outer edge of the specimen.The micrograph shows the existance of two distinct phases, one dark and the other bright. Selected area diffraction patterns taken from the bright phase are shown in Fig.4.14 (a,b). By comparing these diffraction patterns with the standard patterns of ordered hexagonal α_2 phase (Fig4.15 (a,b)), it was confirmed that the bright phase was the α_2 phase. The composition of this phase, as measured by EDS in TEM, is given in Table 4.4. The selected area diffraction patterns obtained from the dark phase are shown in Fig.4.16 (a,b). These diffraction pattern corresponded to the [110] and [111] zone axes of the ordered B2 phase. This was confirmed by comparing these diffraction patterns with the standard [110] and [111] patterns of B2 phase (Fig4.17 (a,b)). The spots in excess of those corresponding to the B2 phase are known [49,54,55] to belong to a ω-type phase which is present as precipitates in the B2 matrix. ω-type phase, whenever present as precipitates in the B2 phase matrix, has the orientation relationship: $[1120]_\omega // [110]_{B2}$ and $(0001)_\omega // (111)_{B2}$. Some of the extra spots are the result of double diffraction, e.g. the forbidden 1/3 001 and 1/3 110 spots that appear in the diffraction pattern corresponding to the $[110]_c$ zone axis. The bright field image and the dark field image taken with a

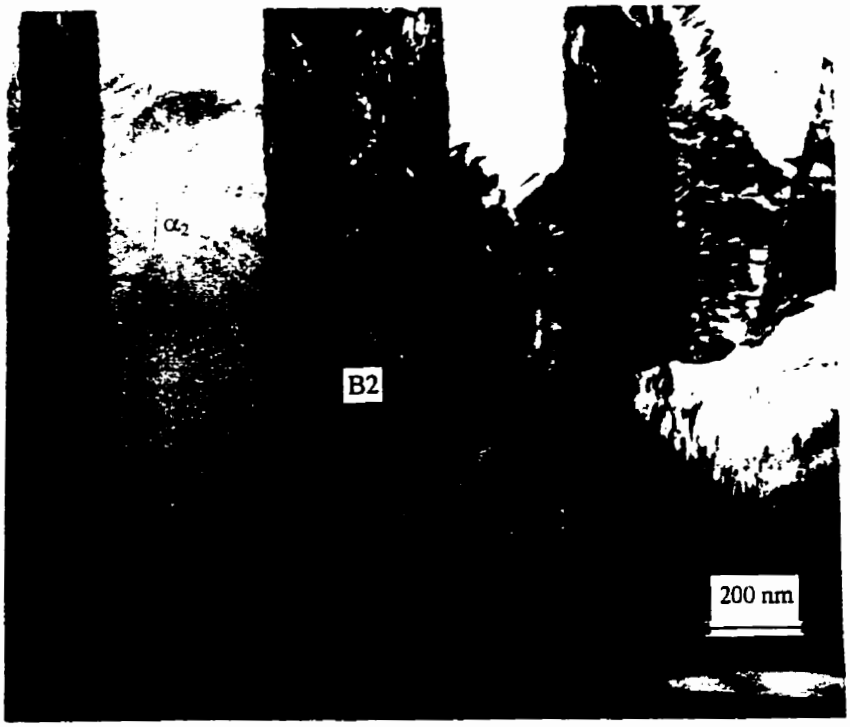

Fig.4.13 Bright field image representing the region close to the outer edge of the specimen.

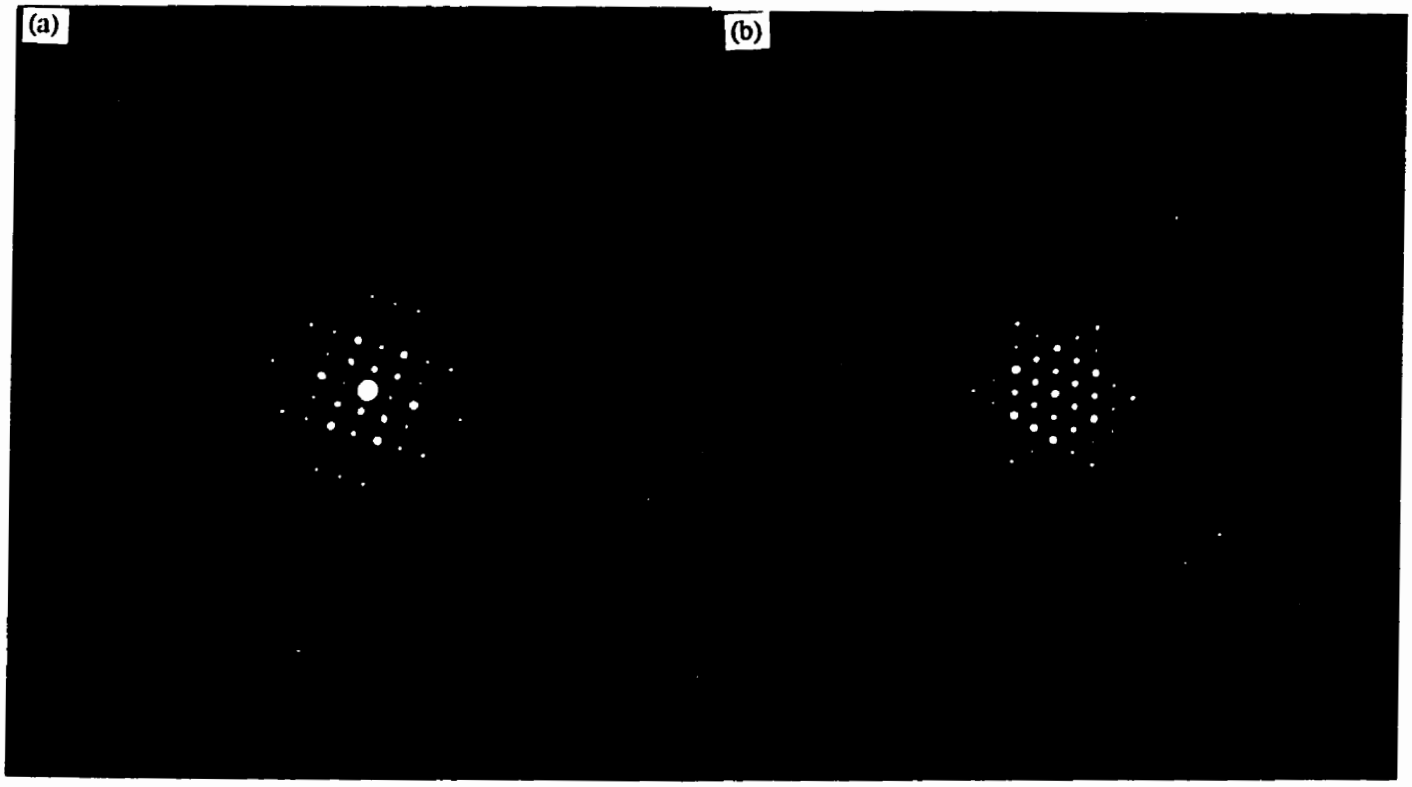

Fig.4.14 Selected area diffraction patterns corresponding to (a) [$1\bar{2}10$] and (b) [0001] zone axes of the α_2 phase.

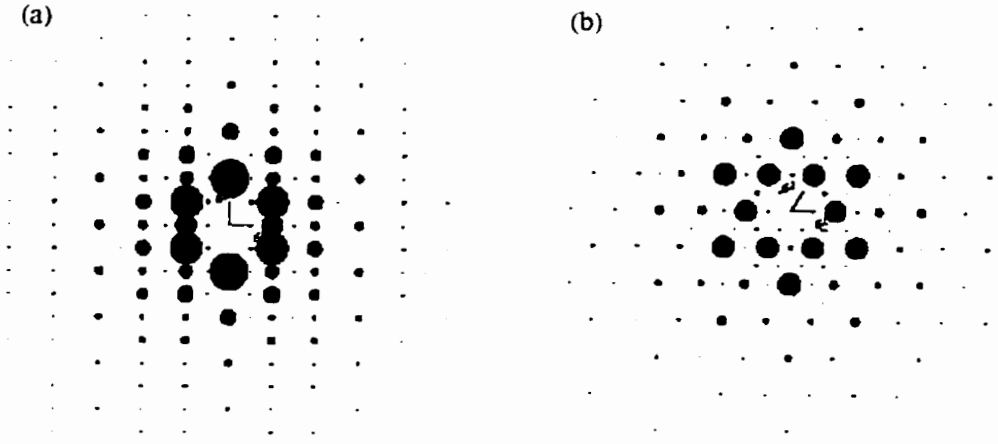

Fig.4.15 Standard diffraction patterns of (a) [$1\bar{2}10$] and (b) [0001] zone axes of α_2 phase.

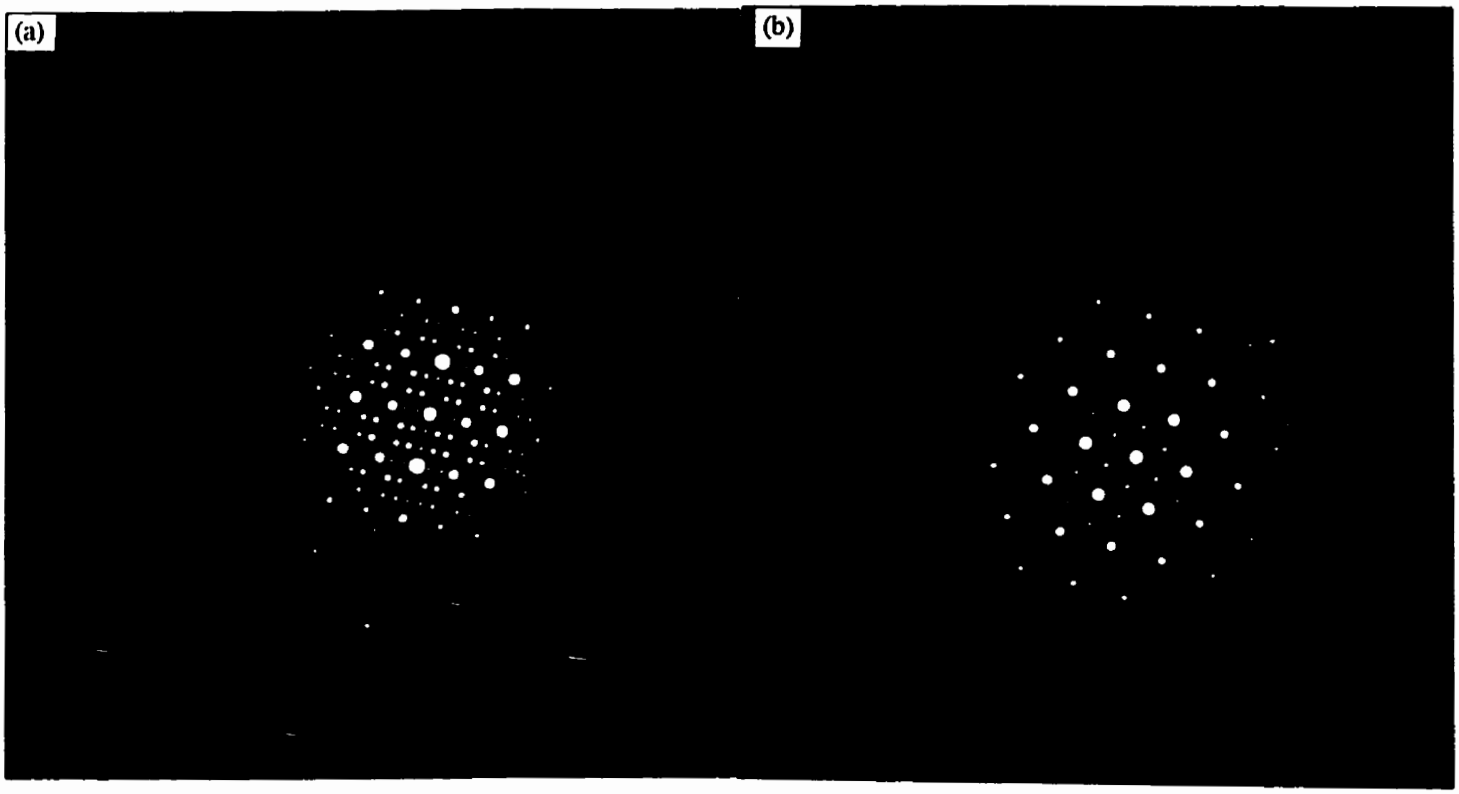

Fig.4 16 Selected area diffraction patterns corresponding to (a) [110] and [111] cubic zone axes.

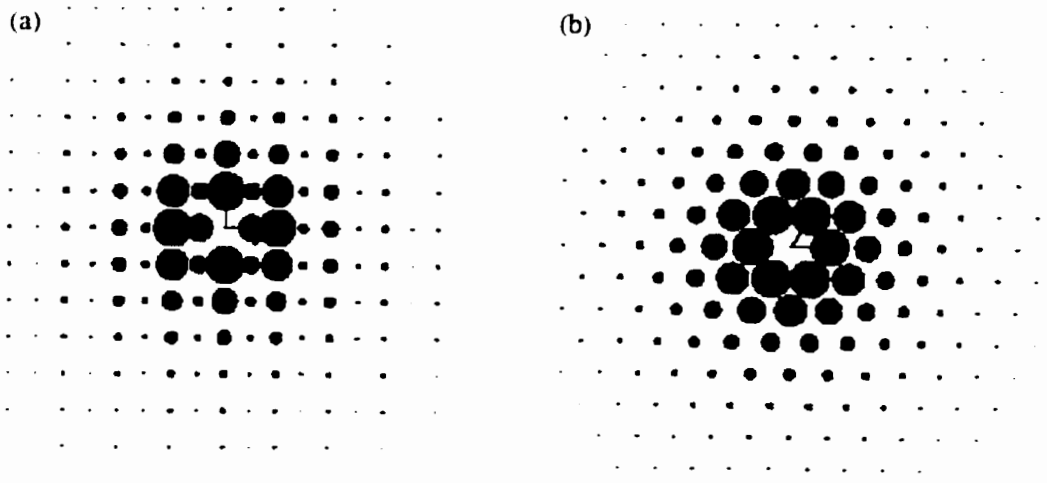

Fig.4.17 Standard diffraction patterns showing (a) [110] and (b) [111] zone axes of ordered bcc structure.

(a)

(b)

Fig.4.18 (a) Bight field image, (b) dark field image showing ω-type phase domains in the region close to the outer edge of the specimen.

reflection belonging to the ω-type phase are shown in Fig.4.18 (a,b). The dark phase was thus identified as the B2 phase containing ω-type precipitates. This ω-type phase has been reported to have $B8_2$ structure [55]. The composition of the B2 phase containing ω-type precipitates was measured by EDS in TEM. The measured composition is given in Table 4.4.

The bright field image of the central region of the damaged layer is shown in Fig.4.19. The microstructure shows two phases, white and gray, with a relatively large grain size. The selected area diffraction patterns obtained from the gray phase fully conformed with the standard diffraction patterns of the ordered hcp phase. The phase was thus identified as α_2. The composition of this phase was measured by EDS and is given in Table 4.4. The selected area diffraction patterns of the white phase are shown in Fig.4.20 (a,b). The bright spots belong to the B2 phase. Along with these bright, sharp spots, some extra diffuse spots are also observed. It is seen that these diffuse spots appear at the same locations as those belonging to the ω-type phase in Fig.4.16. These diffuse spots have been reported [55] to be the characteristic of the early stage of ω-type phase formation and the phase has been designated as ω″. The SADP's also show diffuse maxima at ½ 110 positions. The composition of the B2 phase containing ω″ phase is given in Table 4.4.

The bright field image of the region closest to the undamaged lamellar bulk is shown in Fig.4.21. It is seen that the region close to the undamaged bulk consists of only one phase. The SADP's taken from this phase conformed well with the standard diffraction

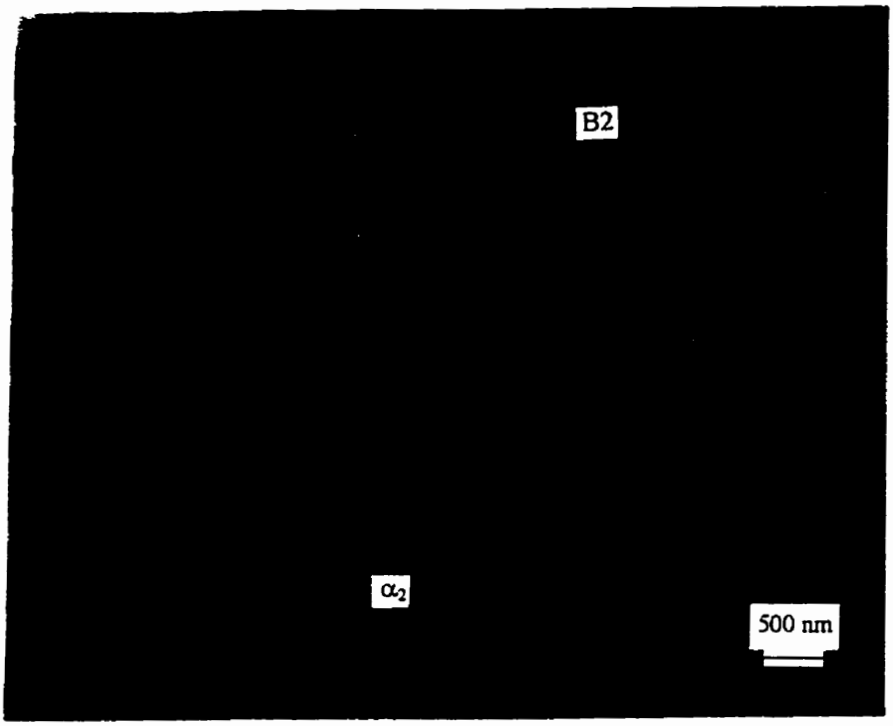

Fig.4.19 Bright field image showing α_2 and B2 phase in the central region of the damaged layer.

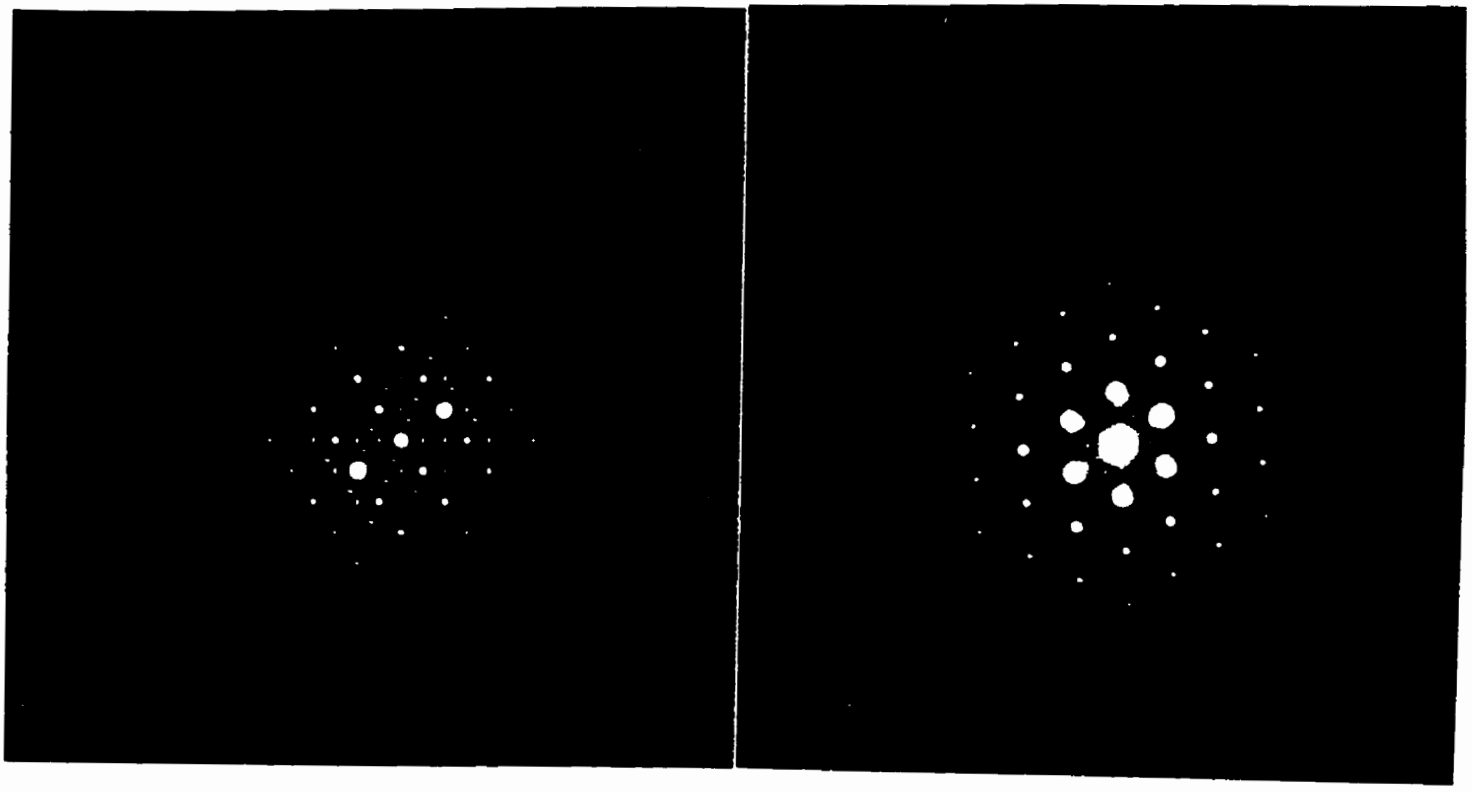

Fig.4.20 Selected area diffraction patterns corresponding to [110] and [111] cubic zone axes taken from the B2 phase in the central region of the damaged layer.

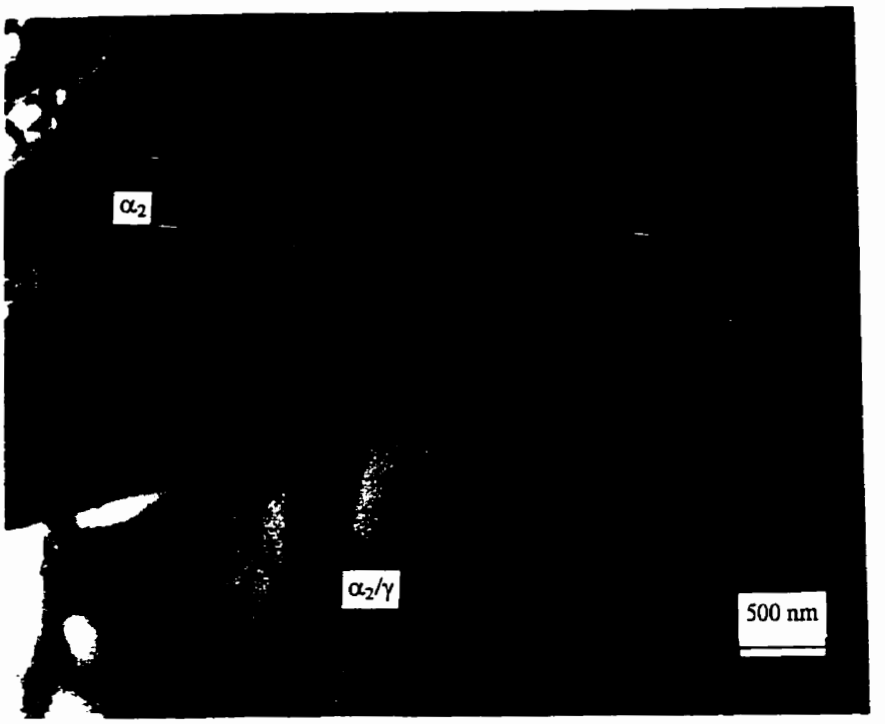

Fig.4.21 Bright field image showing α_2 phase near the undamaged lamellar bulk.

Region of the damaged layer	Phase	Concentration (at %)		
		Al	Mn	Nb
Close to the outer edge	α_2	33.63	1.14	2.33
	B2 + ω-type phase	33.90	2.5	2.8
Central region	α_2	37.10	1.10	2.18
	B2+ω″	37.17	2.17	2.61
Close to the undamaged bulk	α_2	41.2	1.67	1.89

Table 4.4 Composition of various phases present in different regions of the damaged layer

patterns of ordered hexagonal α_2 phase. The measured composition of this phase is given in Table 4.4. No specific orientation relationship was observed to exist between the α_2 of the damaged layer and the α_2 and γ lamellae of the lamellar structure.

4.6 ANALYSIS OF Ta FOIL

Fig.4.22(a) shows the secondary electron SEM image of the surface of the Ta foil that was exposed to the specimen during heat treatment. This inner surface of the Ta foil was found to consist of metallic deposits. The EDS spectrum acquired from this surface is shown in Fig.4.22(b). It indicates the presnce of large amount of Ti and some Al. Ta and Mn are present in small amounts. Fig.4.23(a&b) show the cross section of Ta foil before and after the annealing treatment. Fig.4.23(b) shows that after heat treatment, a distinct layer deposited on the inner surface of the foil whereas no such deposit was observed on the outer surface of the foil. The compositions at various locations in the deposited layer as well as the Ta foil are given in Table 4.5. It is seen that titanium content decreased with distance from the outer surface of the deposited layer whereas tantalum content increased with the distance.However, there was an appreciable decrease in Al content and manganese was uniformly distributed throughout the deposited layer. The compositions are indicative of outward diffusion of Ta and inward diffusion of Ti and Al.

The EDS spectrum acquired from the outer most surface of the foil after heat treatment is shown in Fig.4.24. The spectrum indicates the presence of tantalum, oxygen and an

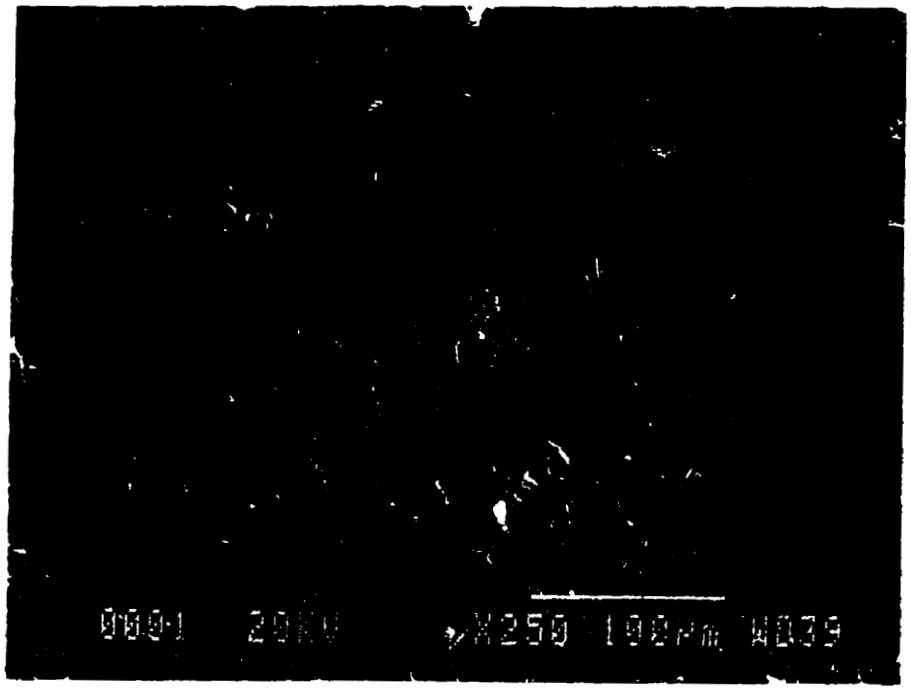

(a)

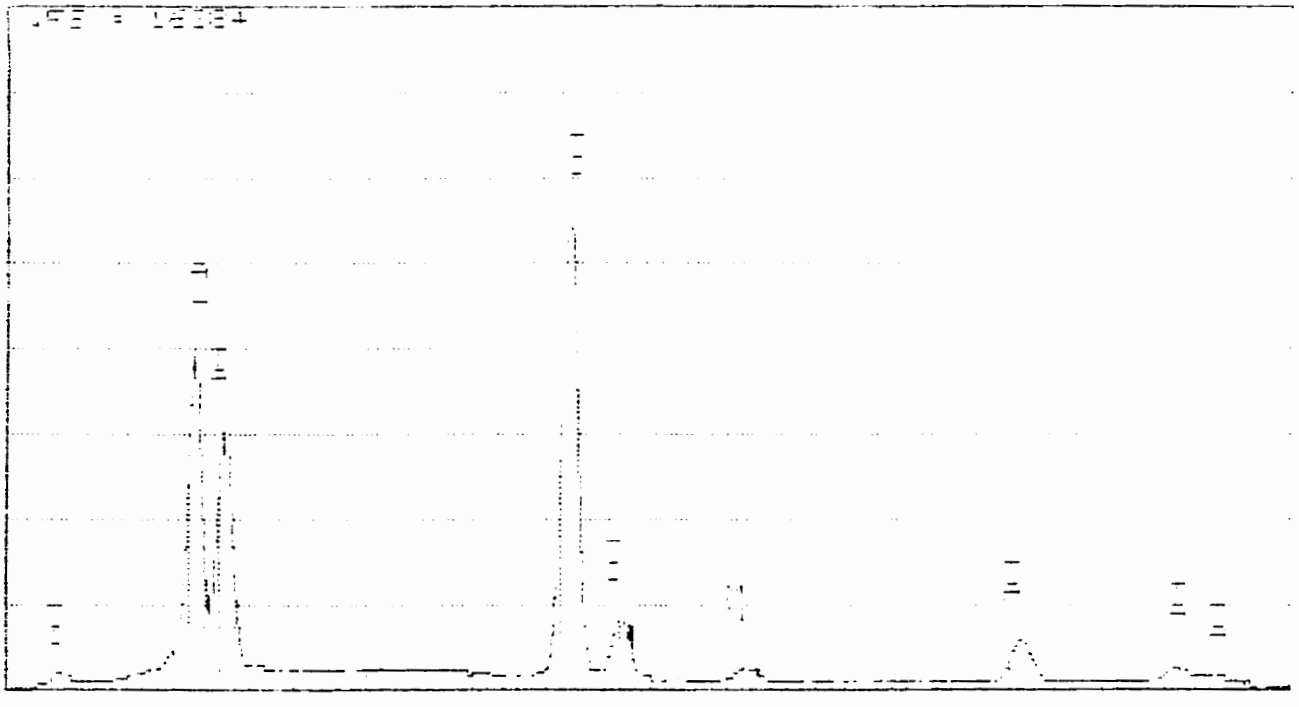

(b)

Fig.4.22 (a) Secondary electron image of the surface of the Ta foil exposed to the specimen during heat treatment, and (b) EDS spectrum obtained from the surface of the Ta foil shown in (a).

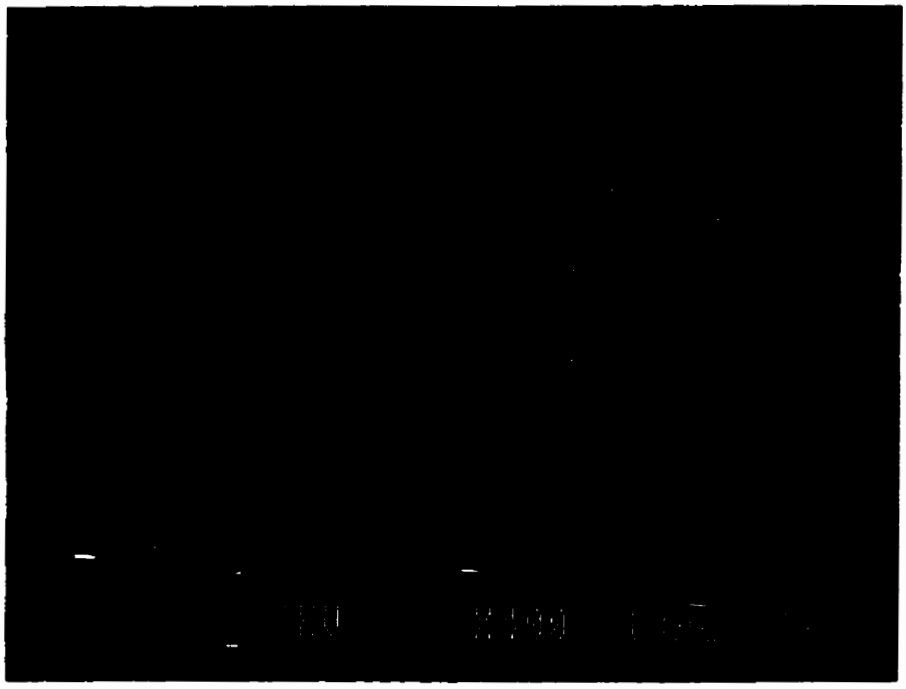

(a)

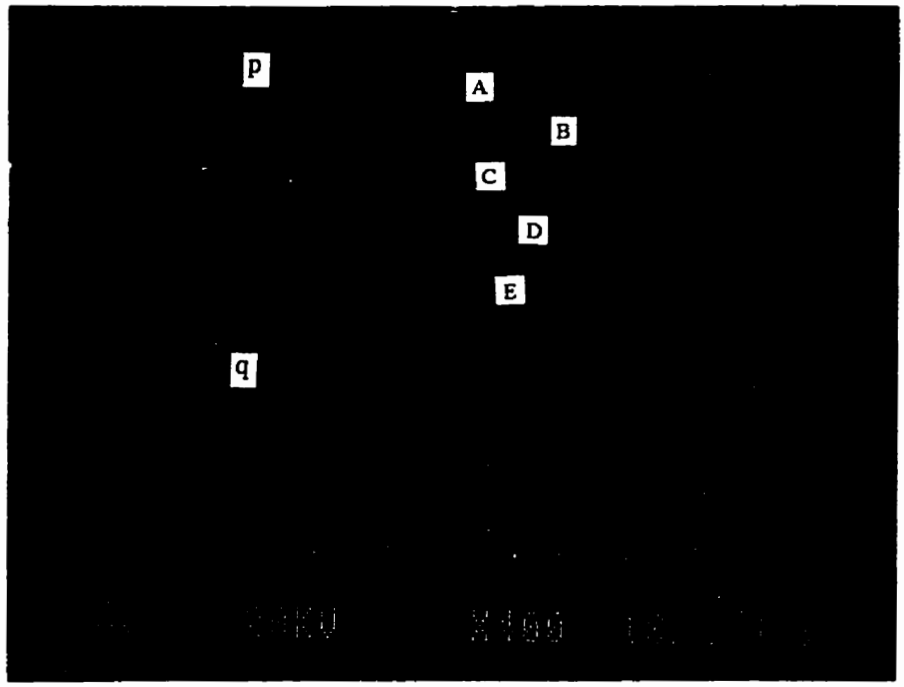

(b)

Fig.4.23 Secondary electron image of the cross section of Ta foil (a) before and (b) after heat treatment.

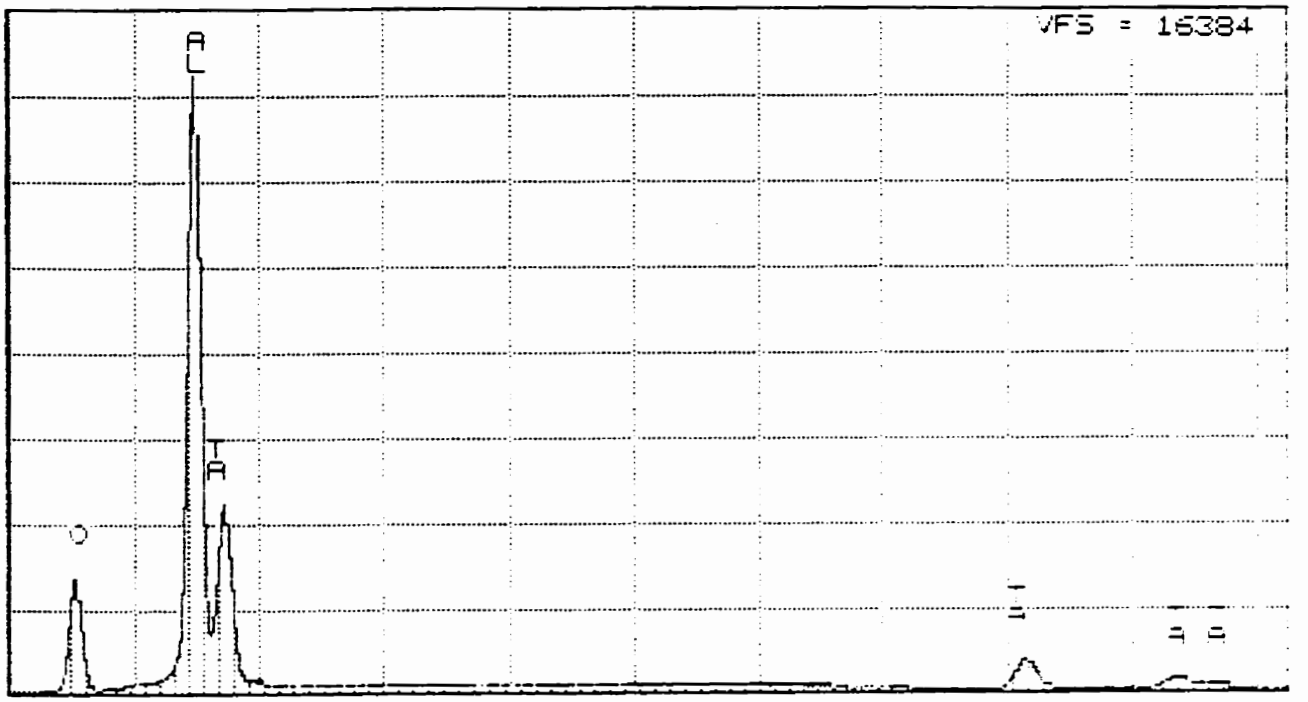

Fig.4.24 EDS spectrum obtained from the outer surface of the Ta foil.

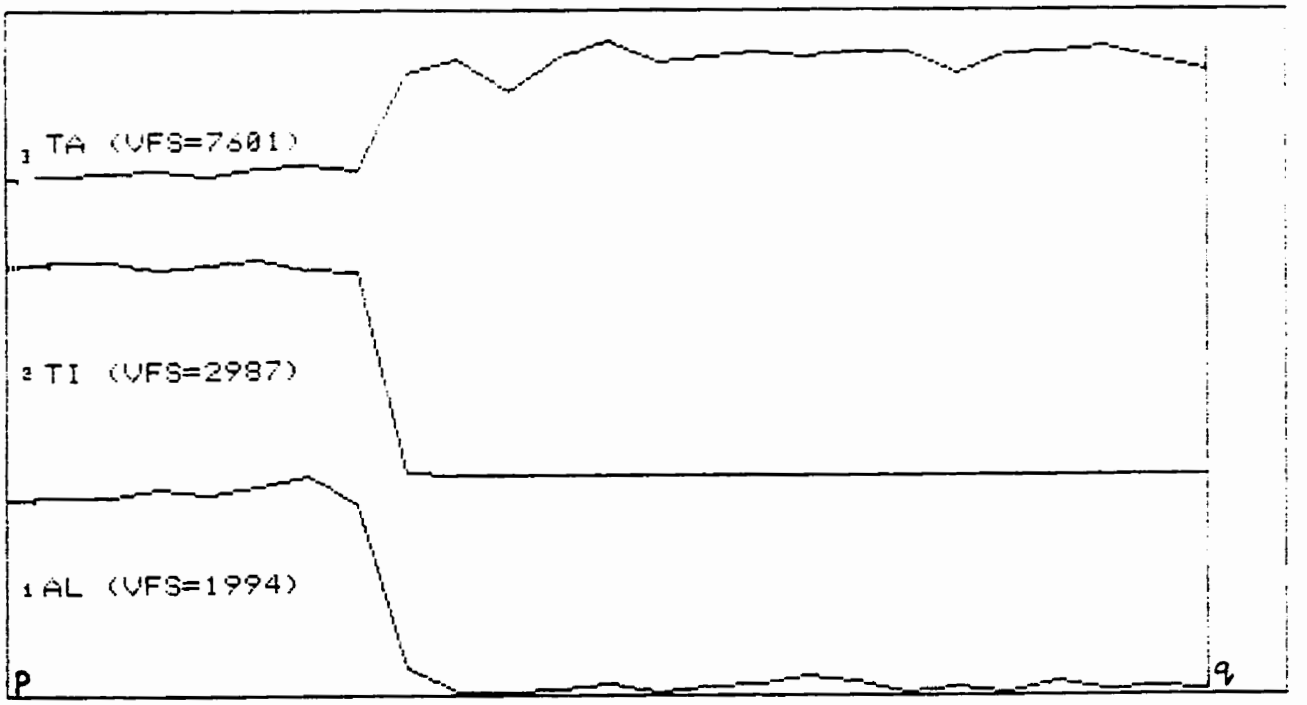

Fig.4.25 Line scanning along the line pq shown in Fig.4.23b.

Location	Concentration in at.%			
	Ta	Ti	Al	Mn
A	11.03	53.40	33.57	2.00
B	22.12	45.29	30.49	2.10
C	33.26	37.24	27.43	2.07
D	100	-	-	-
E	100	-	-	-

Table 4.5. Compositions at various locations in the cross section of the Ta foil after heat treatment.

appreciable amount of aluminum. However, no oxygen was found to be present on the surface of the foil that was exposed to the specimen during heat treatment.

Line scanning along the line pq, shown in Fig.4.23(b), was done to obtain the distribution of Ta, Ti, and Al in the foil. The line scan along the line pq is shown in Fig.4.25. It is seen that the Ti and Al contents drop almost to zero at the deposited layer/foil interface.

4.7 DAMAGED LAYER IN THE SPECIMEN HEAT TREATED WITHOUT Ta WRAPPING

One of the specimens was also heat treated in an atmosphere of commercial argon without wrapping it in tantalum foil. The BSE-SEM image of two samples, one wrapped in Ta and the other without Ta wrapping, heat-treated for the same time under the same conditions of pressure and temperature, are shown in Fig.4.26 and Fig.4.27, respectively. The thickness of the damaged layer is observed to be almost the same in both the specimens. The damaged layer of the specimen wrapped in Ta foil consists of white phase in the region close to the outer edge of the specimen and gray phase near the interface between the damaged layer and the undamaged lamellar bulk. On the other hand, in the case of the specimen that was not wrapped in Ta foil during heat treatment, the damaged layer has a different morphology. Right at the outer edge of the specimen, the damaged layer consists of the gray phase instead of the white phase. Also, almost 33 % of the damaged surface layer consists of cracks both horizontal and vertical. Also,

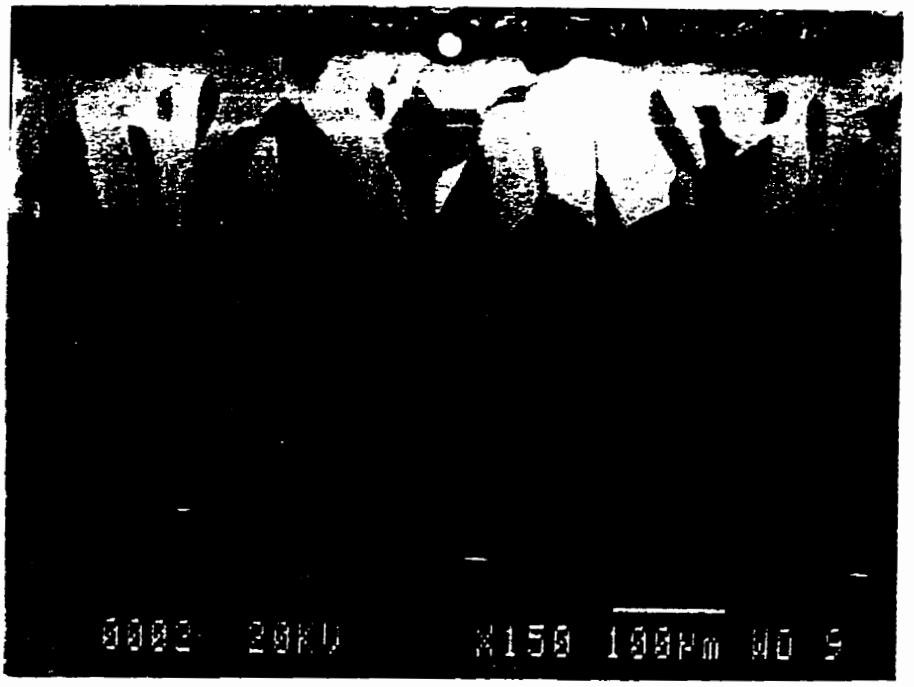

Fig.4.26 Back scattered electron image of the specimen wrapped in tantalum and annealed at 1200°C for 25 hrs.

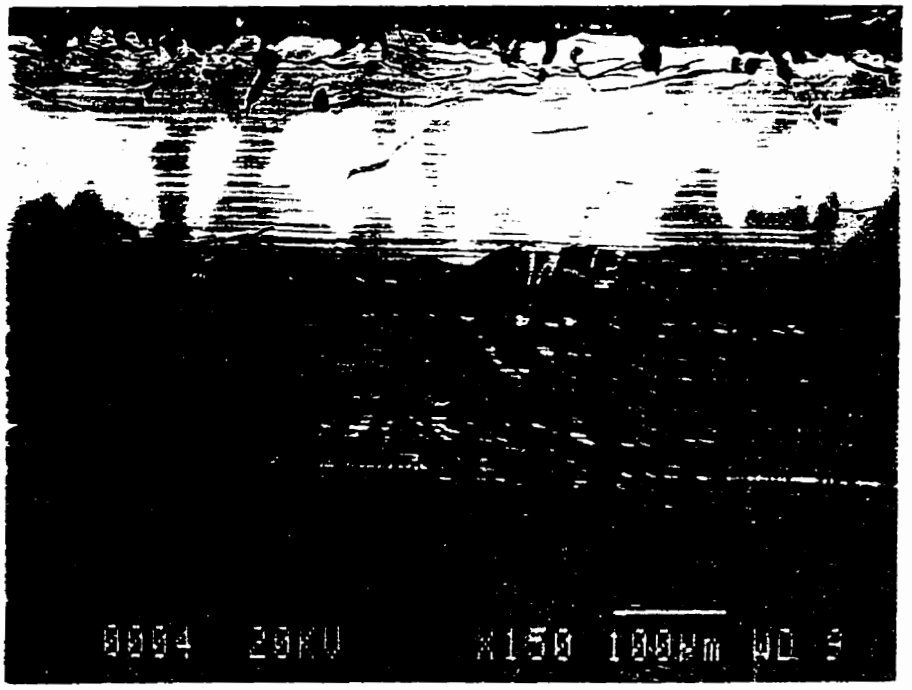

Fig.4.27 Back scattered electron image of the specimen annealed at 1200°C for 25 hrs without wrapping in tantalum foil.

Elements	Concentration in at.%
Ti	67.26
Al	29.46
Mn	0.41
Nb	2.87

Table 4.6. Composition of the gray phase near the outer edge of the specimen heat treated at 1200C for 25 hrs without Ta wrapping.

outer damaged gray layer was found to be joined to the inner gray layer by "links" or "bridges".

The result of the EDS analysis of the gray region near the outer edge (Fig.4.27) is given in Table 4.6. It is seen that this phase has very low concentration of Al and Mn.

4.8 OXIDATION BEHAVIOUR AT 850°C IN AIR

Oxidation tests were carried out at 850°C in air for 7 days and 15 days. The cross sections of oxidized specimens were observed in SEM in both back scattered and secondary electron modes. Fig.4.28 and Fig.4.29 show the secondary electron and BSE images of the samples oxidized for 15 days, respectively. It is seen that the oxide scale has three distinct layers, and the scale is not adherent to the specimen surface. The EDS spectra obtained from each of these regions are shown in Fig.4.30 to Fig.4.33. They show that the outermost white layer (a) consists of titanium and oxygen only. The layer below the titanium oxide layer (c) consists of primarily aluminum oxide with small amount of titanium. The interface between these two layers (b) consists of Ti, Mn, small amount of Al and oxygen. The innermost layer of the oxide scale (d) is a mixture of titanium and aluminum oxide.

The back scattered electron image of the cross section of the oxidized specimen (Fig.4.29) shows that surface damage took place due to oxidation in air at 850°C which is close to the expected service temperature of γ-titanium aluminides. The region below the

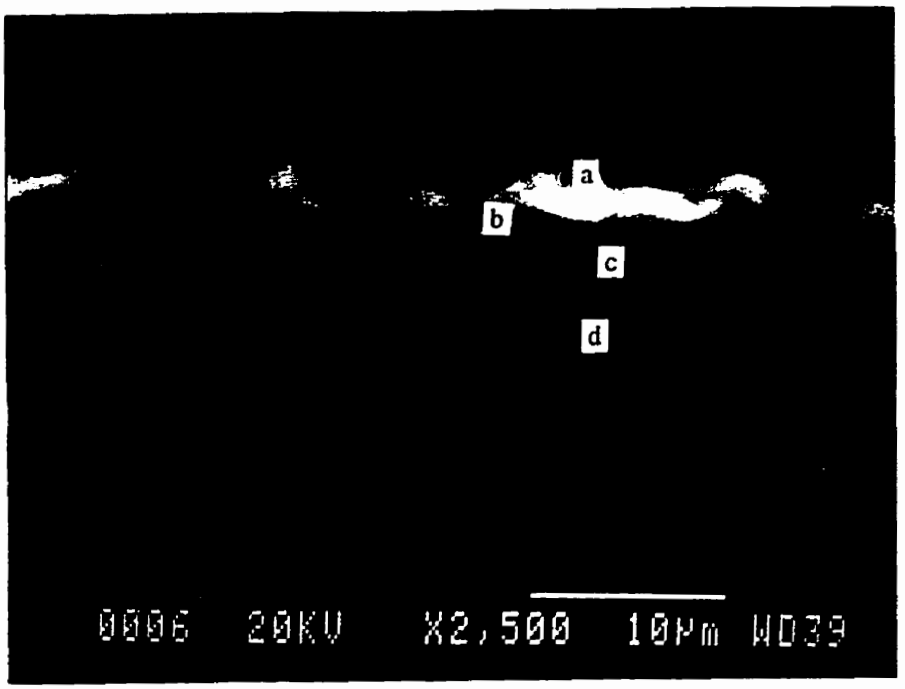

Fig.4 28 Secondary electron image of the specimen oxidized at 850°C in air showing the oxide scale which is not adherent to the specimen.

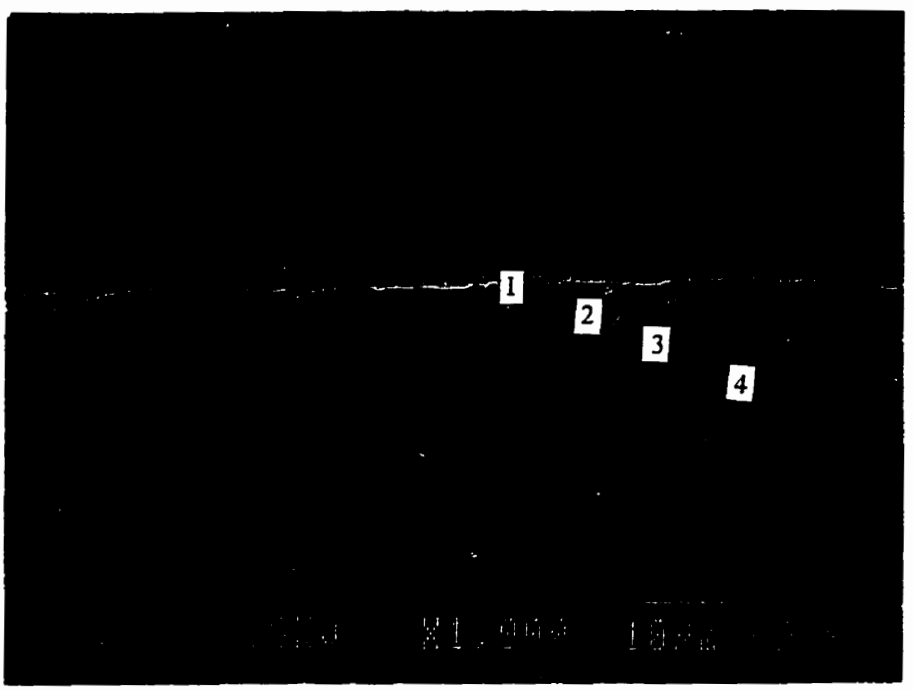

Fig.4.29 Back scattered electron image of the specimen oxidized at 850°C in air.

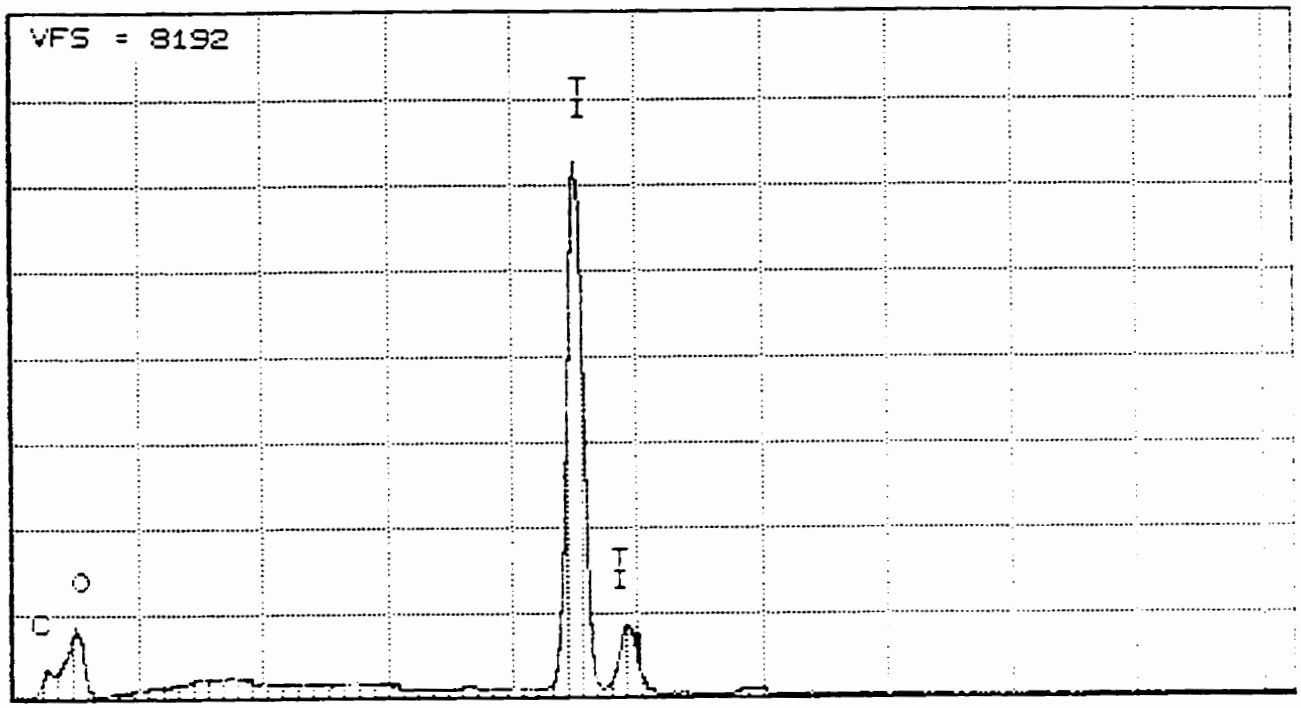

Fig.4.30 EDS spectrum from the point a (in Fig.4.28).

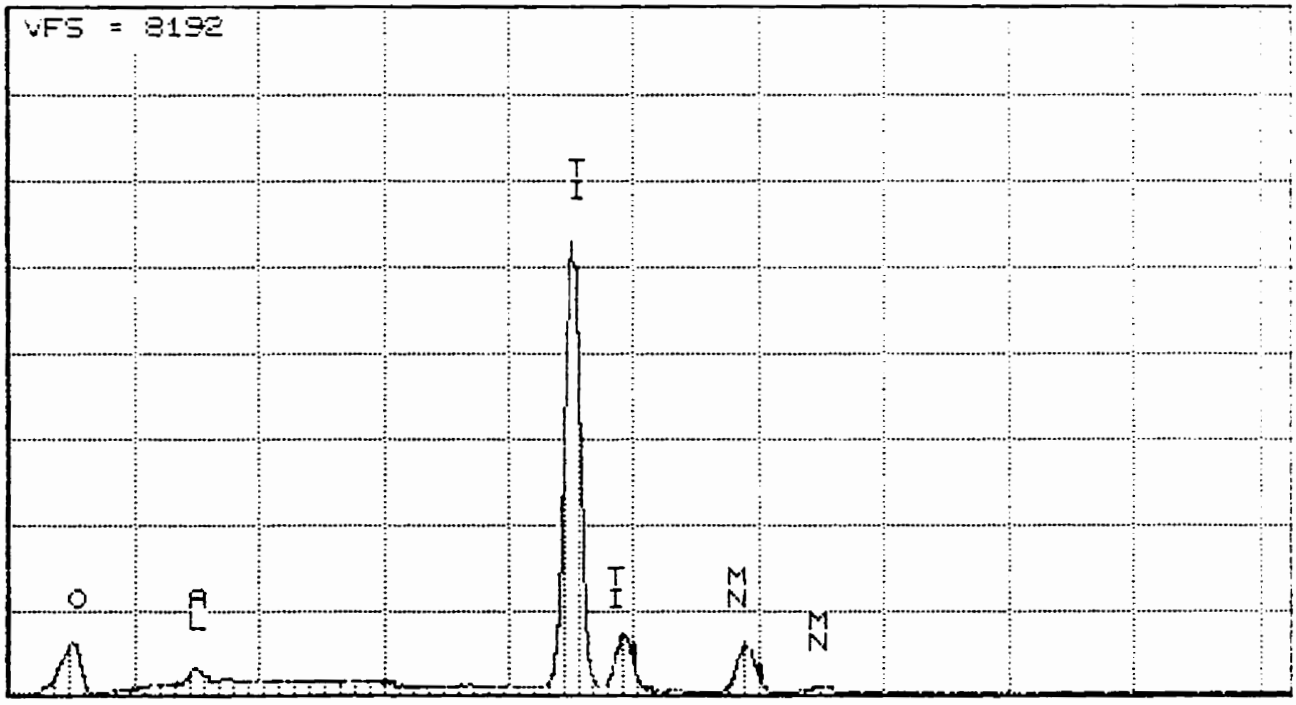

Fig.4.31 EDS spectrum from the point b (in Fig.4.28).

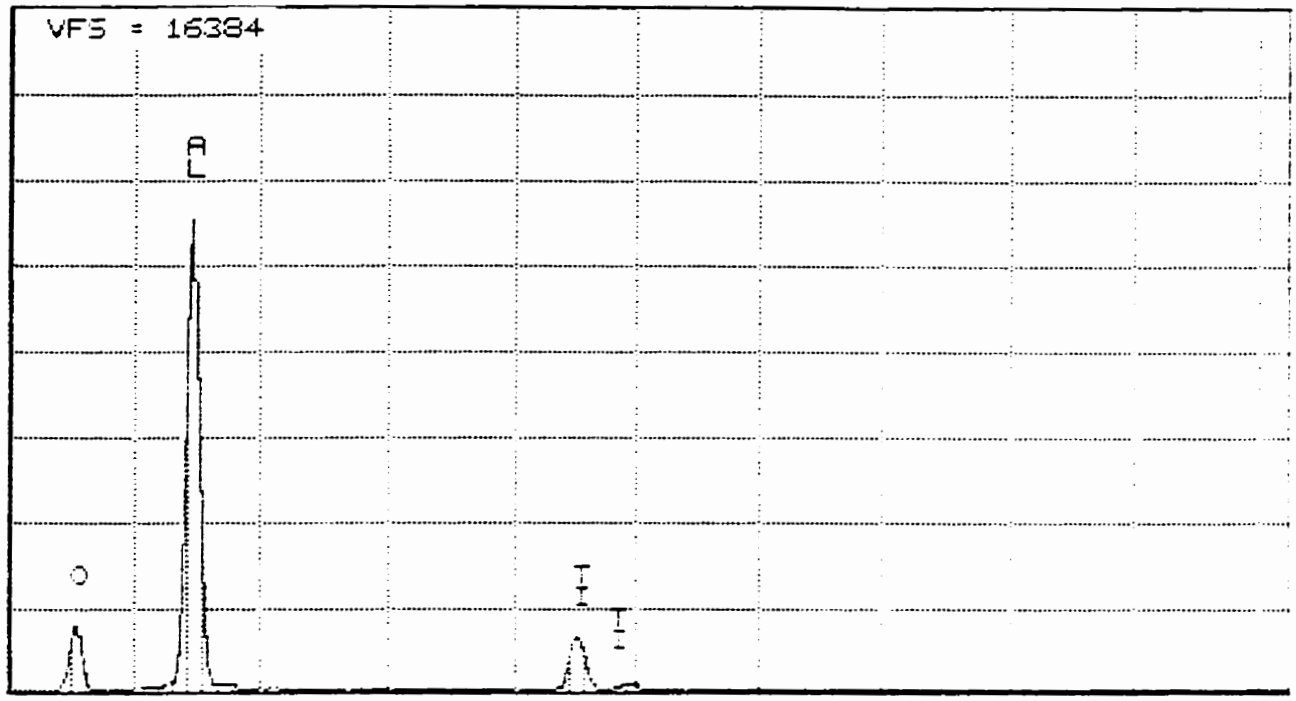

Fig.4.32 EDS spectrum from the point c (in Fig.4.28).

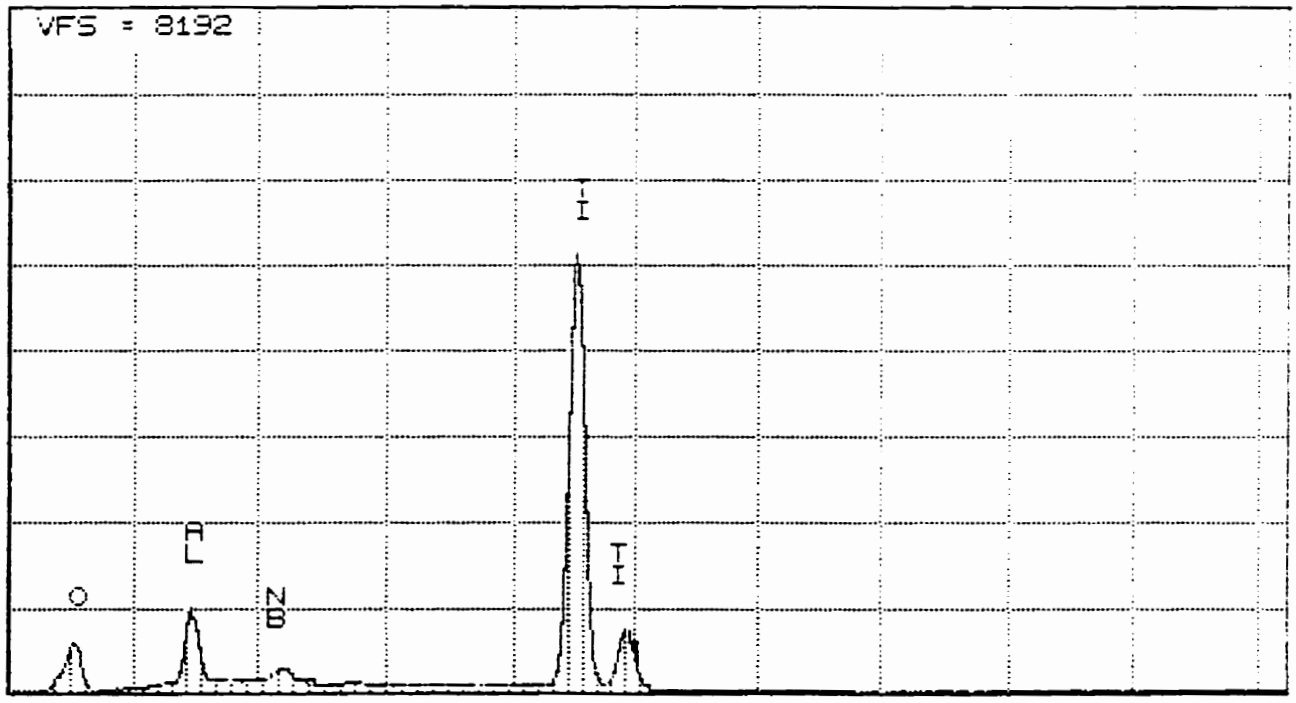

Fig.4.33 EDS spectrum from the point d (in Fig.4.28).

Locations	Concentrations (at.%)			
	Ti	Al	Mn	Nb
1	48.69	37.67	6.77	6.87
2	44.26	50.77	1.82	3.15
3	45.54	49.97	1.79	2.70
4	47.62	47.99	1.77	2.62

Table 4.7. Compositions at various locations in the damaged layer formed during oxidation at 850C in air for 15 days.

oxide scale appears white in Fig.4.28 and 4.29. The composition analysis of this layer shows that there is a high concentration of titanium in the layer. Below this titanium rich layer there is a region (~10 μm thick) with a morphology significantly different from the base material. This layer has a relatively higher concentration of aluminum than the base material. The compositions at various locations in this damaged layer are given in Table 4.7. All the composition measurements in this case were done using the SQ software.

Chapter 5

DISCUSSIONS

5.1 MECHANISM OF LOSS OF SOLUTES FROM THE SPECIMEN DURING HEAT TREATMENT

At the onset of the heat treatment, the vapour pressures of different solutes are almost zero. With increase in time the vapour phase tries to establish equilibrium with the specimen. Thus causing loss of solutes from the surface of the specimen. The equilibrium vapour pressure data of Ti, Al, Mn and Nb at 1200°C are given in Table 5.1. The vapour pressures of the elements Ti, Al, Mn and Nb in equilibrium with the alloy at 1200°C were calculated assuming their activities to be equal to the atom fractions of various elements in the alloy. The vapour pressures of Al and Mn are observed to be the highest and of the same order of magnitude. The vapour pressure of Ti is about four orders of magnitude lower than that of Al and Mn. The vapour pressure of Nb is the smallest and is very small as compared to the other elements.

Although vapour pressures of both Al and Mn are high and comparable, Al_2O_3 is more stable than the oxides of Mn and Ti. The free energies of formation of one mole of Al_2O_3 , one mole of TiO_2 and one mole of MnO at 1200°C are 288 kCal, 156 kCal, and 89 kCal, respectively. Therefore, Al vapour reacts with oxygen that might be present in the vycor capsule to form Al_2O_3. The resulting oxide deposits on the outer surface of the tantalum

Elements	Vapour pressure at 1200 (atm)	Vapour pressure in equilibrium with the alloy at 1200C (atm)
Ti	$\sim 10^{-9}$	$\sim 5.1 \times 10^{-10}$
Al	$\sim 10^{-5}$	$\sim 4.5 \times 10^{-6}$
Mn	$\sim 10^{-3}$	$\sim 17 \times 10^{-6}$
Nb	$\sim 10^{-18}$	$\sim 2 \times 10^{-20}$

Table 5.1. Vapour pressure data of various elements.

foil. This was confirmed by the EDS analysis of the outer surface of the foil (Fig.4.24). Once oxygen is eliminated from the vycor capsule, Al, Ti and Mn vapours react with the inner surface of Ta foil. This was confirmed by the examination of microstructure of the cross-section of the Ta foil after the heat treatment (Fig.4.23b). During heat treatment the Ta foil was closely wrapped to the specimen and hence the reaction took place on the inside surface. Also, the presence of Al_2O_3 on the outside surface would prevent the reaction of the vapours with the Ta foil. A deposited layer was observed on the inside surface of the foil whereas no deposits were observed on the outer surface of the foil. Also, the EDS analysis of the inside surface of the foil showed the presence of Ti, Al, Mn and some Ta (Table 4.5).

The line scan along a line across the cross section of the foil (Fig.4.25) showed that there was very little penetration of Ti and Al into the Ta foil. The Al and Mn content in the deposited surface layer was almost constant (Table 4.5). The sum of Ti and Ta contents remained almost constant throughout the layer. However, Ti content decreased into the surface layer and Ta content decreased outward. Ti and Ta have complete solid solubility in each other, therefore, Ta replaced Ti in its sublattice whereas Al content remained constant at ~30 at.% throughout the deposited layer.

Specimens lost Ti, Al and Mn from the surface. No loss of Nb took place because of its very low vapour pressure. Due to the loss of elements from the surface of the specimen, the composition of the surface changed. The measured composition of the surface were ~61 at.% Ti, ~33 at.% Al, ~2.5 at.% Mn and 2.8 at.% Nb. Same concentration was

maintained for all the three annealing times. The loss of solutes from the surface resulted in the migration of solutes towards the surface of the specimen. This reduced the solute content of the material and caused the formation of a solute depleted layer near the surface of the specimen. The Al content of the damaged layer increased from 33 at.% at the surface to 41 at.% near the interface between the damaged layer and the undamaged bulk. At the interface there was a step increase in the Al content from 41 to 45 at.% Al. This step increase in composition is due to the phase change from α_2 phase to a two phase lamellar structure consisting of α_2 phase and γ phase. At the interface, the compositions of the α_2 phase and the α_2/γ lamellar are those corresponding to the equilibrium compositions of these phases.

Fig.5.1 shows a schematic diagram illustrating the mechanism involved in the loss of solutes from the surface of the specimen and formation of damaged layer. The EDS analysis suggested that the concentration at the outer surface of the specimen is always maintained at 33 at.% Al, and near the interface between the damaged layer and the lamellar bulk at 41 at.% Al for all the three times of annealing. However, the thickness of the damaged layer increases with the increase in the annealing time (Table 4.3). Therefore, a steady state condition for diffusion is maintained both at the outer edge of the specimen and the interface. It is suggested and schematically shown in Fig.5.1 that, under this steady state condition, the solute atoms escape from the surface of the specimen and diffuse in the vapour state towards the Ta foil. The tantalum atoms then try to diffuse outwards through the deposited layer, hence, decreasing the activities of Al and Ti at the surface of the foil. This causes more and more solute atoms to leave the surface

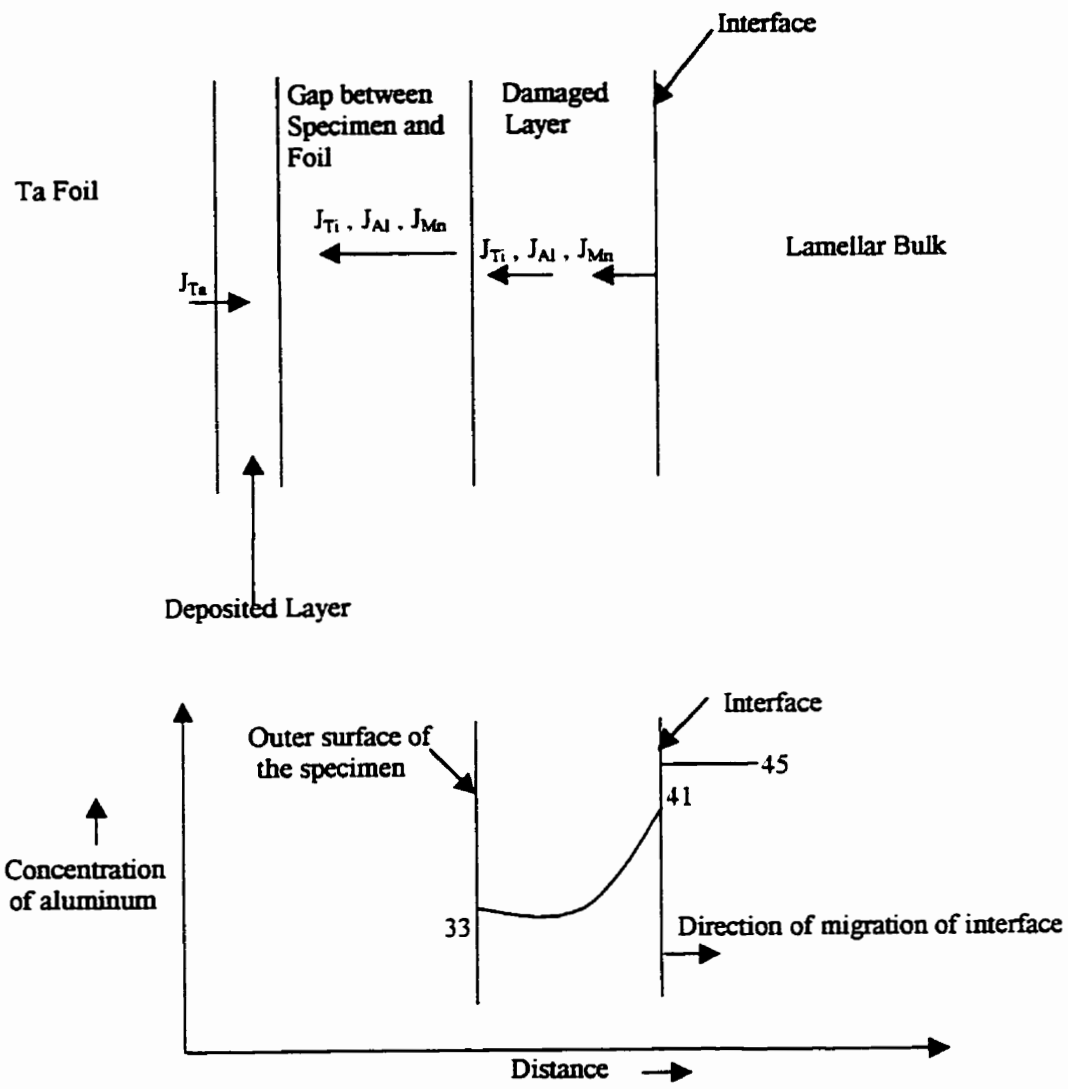

Fig.5.1 Schematic illustration of mechanism of Al loss.

of the specimen. Consequently, migration of solute atoms takes place from the interface to the outer edge of the specimen and the interface migrates in a direction away from the outer edge of the specimen.

5.2 ANALYSIS OF DIFFUSION PROCESS INVOLVED IN THE TRANSFER OF SOLUTE ATOMS FROM THE INTERFACE TO THE OUTER SURFACE OF THE SPECIMEN

Fig.5.2 shows the concentration profile of the solute diffusing from the interface i to the outer surface ,s. In the figure,

C_o = Concentration of the diffusing species in the bulk,

C_i = Concentration of the diffusing species at the interface, i,

C_s = Concentration of the diffusing species at the outer surface, s,

x = Thickness of the damaged layer,

dx = Increase in the thickness in time dt.

The amount of solute rejected into the damaged layer per unit area when the interface moves by a distance dx in a direction away from the outer surface of the specimen, is equal to $dx(C_o-C_i)$. The amount of solute rejected per unit area per unit time is equal to $(dx/dt)(C_o-C_i)$. For steady state diffusion, this should be equal to the flux of the solute, J, in the damaged layer which is given by,

$$J = -D\,(\delta C/\delta x)$$

$$= -D\,(\Delta C/x)$$

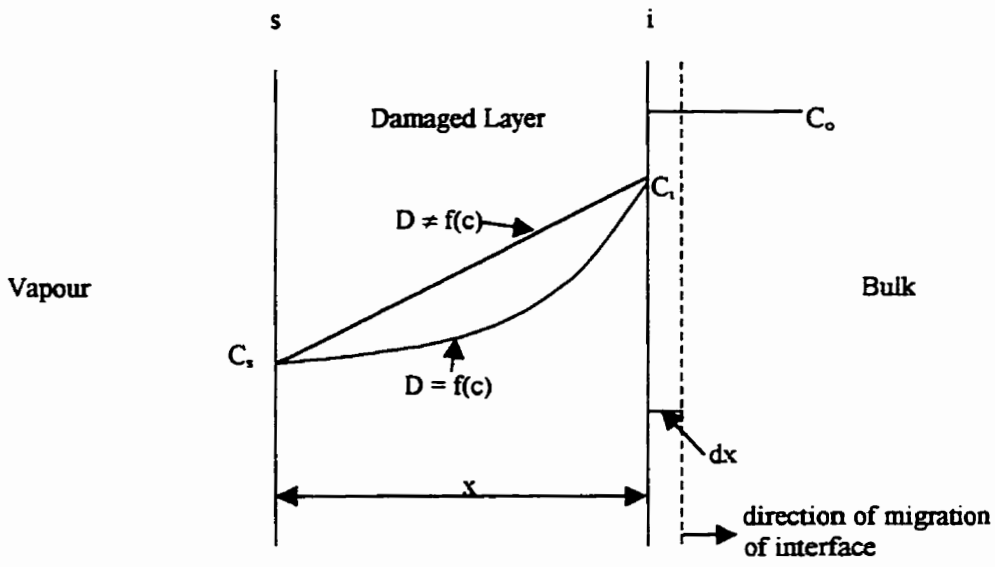

Fig.5.2 Schematic concentration profile of Aluminum.

$$= D (C_i-C_s)/x$$

Therefore,

$$(dx/dt)(C_o-C_i) = D (C_i-C_s)/x \quad \text{..... [5.1]}$$

or, $xdx = D(C_i-C_s)/(C_o-C_i)dt$

Integrating both sides of the above equation, we get

$$x^2 = 2D(C_i-C_s)/(C_o-C_i).t + \text{constt.}$$

or, $x^2 = K.t + \text{constt.}$ ..... [5.2]

where $K = 2D(C_i-C_s)/(C_o-C_i)$

The constant in the equation [5.2] should be equal to zero if there is no deviation from the parabolic relation between the thickness of the damaged layer and time.

In this solution it is assumed that the diffusion coefficient is independent of composition and hence the concentration profile is linear. However, in this system, the diffusion coefficient varies with composition. Therefore, the concentration profile would be curved rather than a straight line. Curved concentration profile was indeed observed in the case of diffusion of Al in the damaged layer (Fig.4.7-4.9).

Equation [5.2] indicates a linear relationship between the square of the thickness of the damaged layer and the annealing time. Fig.5.3 shows the plot of square of the thickness of damaged layer against time. This plot yields a straight line intercepting the ordinate axis at 2879.4. This deviation from the exact parabolic time dependence of the thickness implies that the $x^2 - t$ law is applicable only after a certain transient period. The ordinate axis intercept corresponds to the initial value of thickness. The approximate value of the

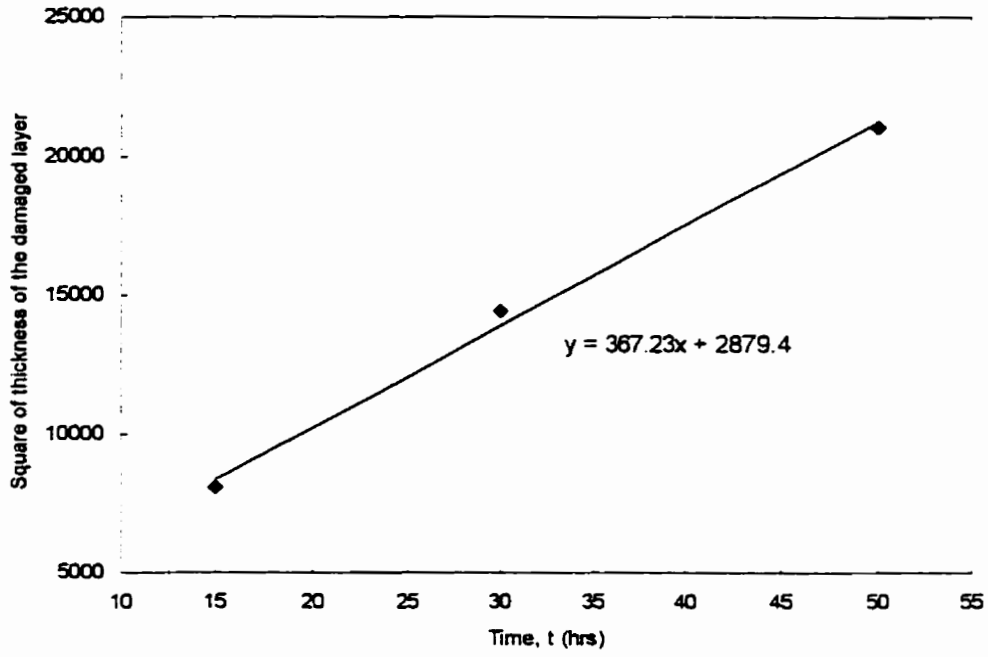

Fig.5.3 Plot of square of the thickness of the damaged layer versus the time of annealing.

diffusion coefficient for the diffusion of Al in the damaged layer, calculated from the slope of the straight line is ~10^{-10} cm^2/sec. This value of D is consistent with the value of diffusion coefficient for the interdiffusion of Al and Ti in Ti_3Al when the parabolic law holds

5.3 ANALYSIS OF PHASE FORMATION IN THE SOLUTE DEPLETED DAMAGED LAYER

During heat treatment, a damaged layer formed due to evaporation of solutes from the surface of the specimens. The damaged layer had a morphology remarkably different from the lamellar structure of the base material. The region close to the outer edge of the specimen consisted of ordered bcc phase (B2 phase) along with ω-type phase precipitates. The region close to the interface between the damaged layer and the undamaged bulk consisted of α_2 phase while the bulk phase contained lamellar structure of α_2 and γ. The boundary between the α_2 phase and the B2 phase was quite irregular with a phase extending upto the regions close to the outer edge of the specimen in some areas. The aluminum content in the damaged layer increased with distance from the outer edge of the specimen. The aluminum content was minimum (~33 at.%) at the outer edge of the specimen and maximum (~41 at.%) near the interface of the damaged layer and the lamellar bulk.

In order to explain the presence of various phases in the damaged layer, one needs to have the Ti-Al-Mn-Nb quaternary phase diagram. Unfortunately, no information about the quaternary system is available. However, the isothermal sections of Ti-Al-Mn system at 1277°C and 1000°C, and those of Ti-Al-Nb system at 1200°C and 1000°C are available [20,34,40]. The ternary diagrams are shown in Figs. 5.4 to 5.7. With the help of these ternary diagrams, it is possible to predict the effect of Mn and Nb on phase transformations in the quaternary system.

Table 5.2 shows the quantitative effect of the two alloying elements on various phase boundaries of the binary Ti-Al system at a temperature close to 1200°C. As can be seen from the ternary Ti-Al-Mn system shown in Fig.5.4, presence of a small amount of Mn in the alloy considerably shifts the $\beta/\beta+\alpha$ and $\beta+\alpha/\alpha$ phase boundaries towards Al-rich side. On the other hand, Fig.5.6 shows that Nb shifts these boundaries towards Al-lean side. However, the effect of Mn is much more significant than that of Nb. As a result, there is a net increase in the aluminum content and the $\beta/\beta+\alpha$ and $\beta+\alpha/\alpha$ phase boundaries shift towards higher Al side. The Mn and Nb content near the outer edge of the specimen were 2.5 and 2.8 at.%, respectively. Assuming the effect of Mn and Nb to be additive, the presence of 2.5 at.% Mn and 2.8 at.% Nb would increase the Al content of the $\beta/\beta+\alpha$ phase boundary from ~27.8 to 34.7 at.% and that of the $\beta+\alpha/\alpha$ phase boundary from 29.7 to 37.5 at.% Al (Table 5.2 and Fig.5.8). The Al content near the outer edge was observed to be ~33 at.%. In the binary Ti-Al system, alloy containing 33 at.% Al would lie in the α single phase field. However, the above estimates show that the presence of alloying elements would shift the $\beta/\beta+\alpha$ phase boundary to 34.7 at.% Al and hence the

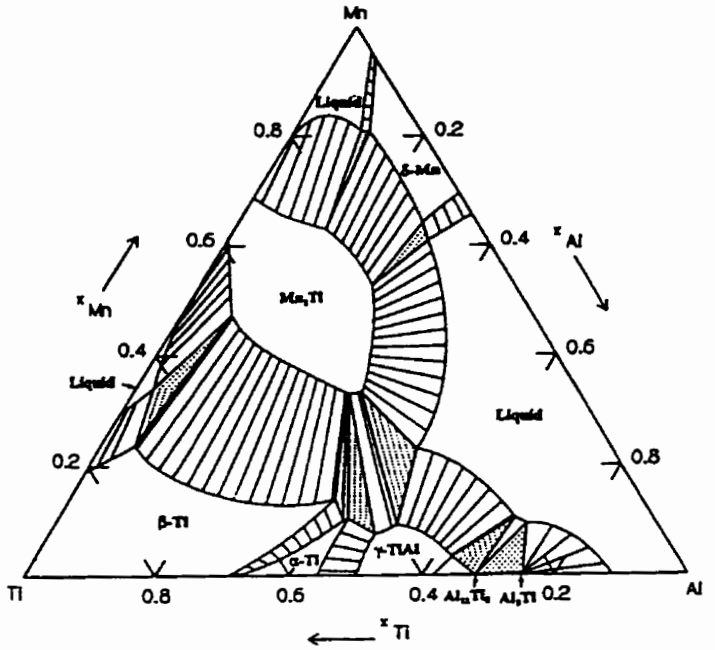

Fig.5.4 Isothermal section of Ti-Al-Mn system at 1277°C.

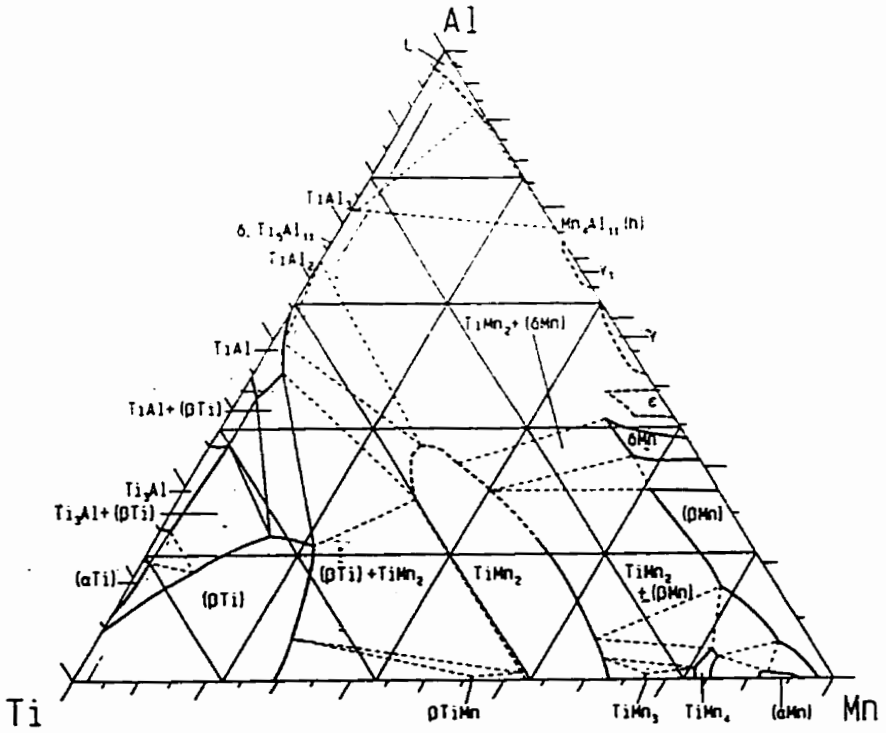

Fig.5.5 Isothermal section of Ti-Al-Mn system at 1000°C.

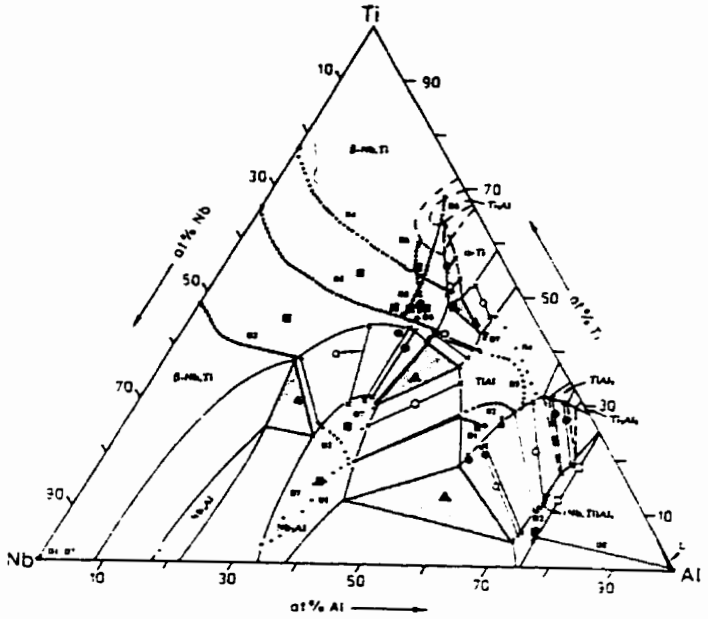

Fig.5.6 Isothermal section of Ti-Al-Nb system at 1200°C.

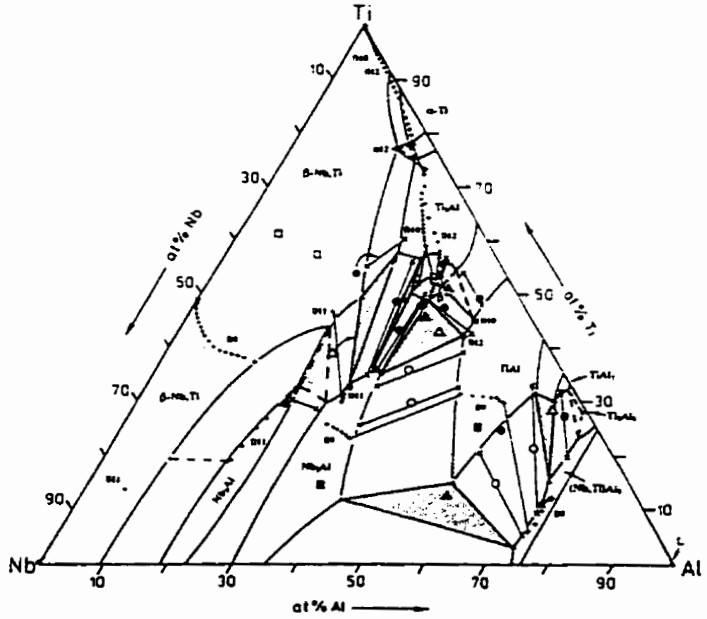

Fig.5.7 Isothermal section of Ti-Al-Nb system at 1000°C.

Alloying elements	Al content of the phase boundaries (at %)			
	β/β+α	β+α/α	α/α+γ	α+γ/γ
From phase diagrams				
0 %	27.87	29.7	40.6	47.8
2 % Mn	36	39	46	52
2 % Nb	25.5	27	41	47
Estimated				
2 % Mn + 2 % Nb	33.6	36.3	46.4	51.2
2.5 % Mn + 2.8 % Nb	34.7	37.5	47.9	51.9
1.7 % Mn + 2 % Nb	32.4	34.7	45.5	50.5

Table 5.2 Effect of the two alloying elements, Mn and Nb, on various phase boundaries of the Ti-Al system at a temperature close to 1200°C

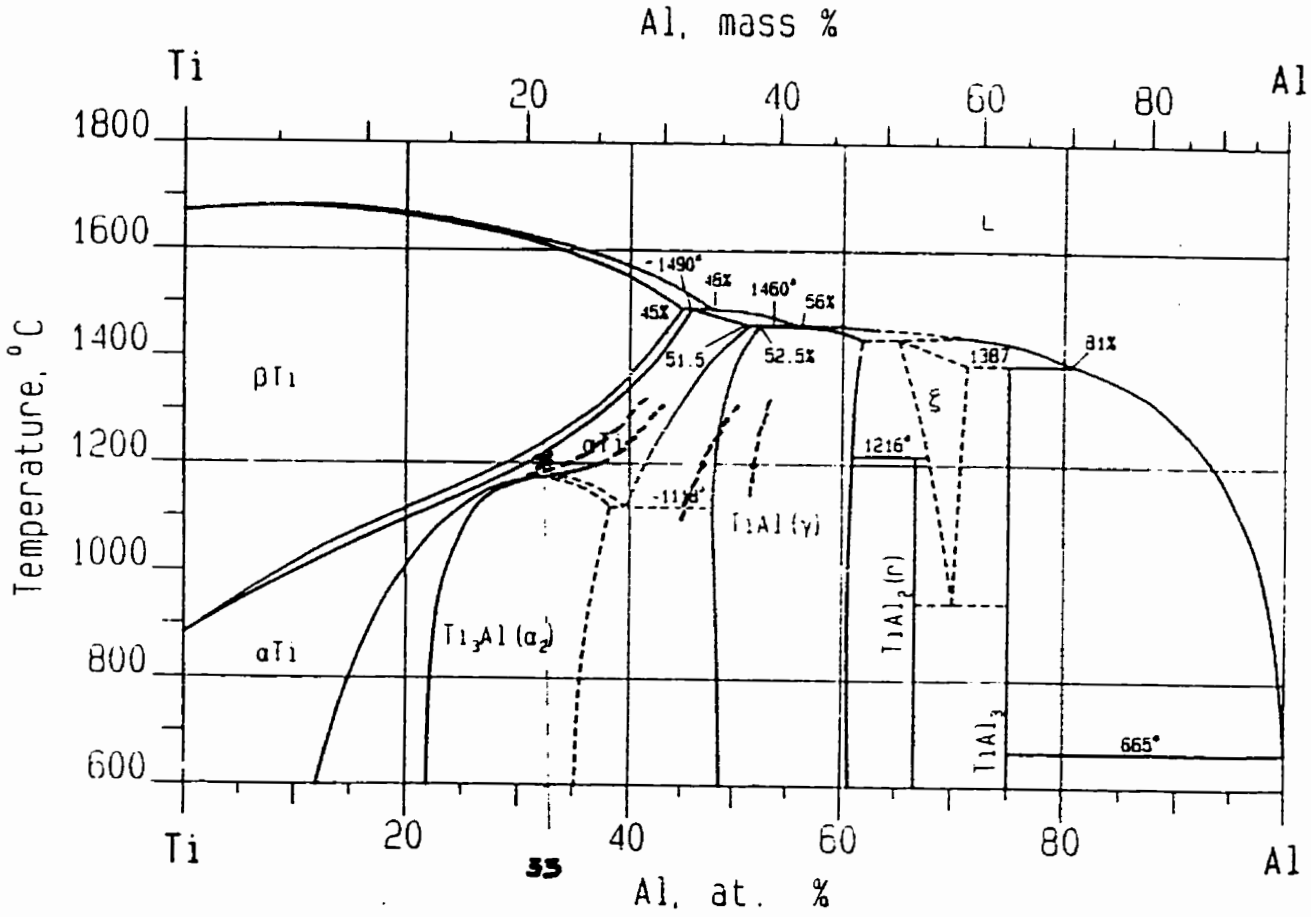

Fig.5.8 Ti-Al phase diagram showing the effect of 2.5 at.% Mn + 2.8 at.% Nb on the binary phase boundaries. New phase boundaries are constructed assuming that the boundaries shift parallel to the existing boundaries.

alloy containing 33 at.% Al would lie within the β phase field as shown in Fig.5.8. This high temperature phase has disordered bcc structure. It has been shown [18,41,42,83] that rapid cooling of β phase results in its ordering to the B2 phase. Furnace cooling of the same phase results in the transformation, $\beta \rightarrow \alpha_2$. Air-cooling, being faster than furnace cooling may result in either the $\beta \rightarrow \alpha_2$ transformation or the β→B2 transformation. The β→B2 transformation involves only the ordering of the lattice, whereas, the $\beta \rightarrow \alpha_2$ also involves a change in crystal structure as well as ordering of the lattice. As a result β→B2 transformation is much faster than $\beta \rightarrow \alpha_2$. Also, the alloying elements, Mn and Nb slow down the transformation rate of the β phase to the α_2 phase. Thus air-cooling is more likely to result in the ordering reaction rather than the transformation of β phase to α_2 phase. In the present investigation, air cooling of the alloy containing ~33 at.% Al, 2.5 at.% Mn and 2.8 at.% Nb from 1200°C resulted in the ordering of the β phase to the B2 phase. Hence, the region near the outer edge of the specimen consisted of the B2 phase. The B2 phase also contained ω-type precipitates. The formation of ω phase during rapid cooling of disordered β phase has long been known in alloys of Ti and Zr. The ω phase has the orientation relationship: $(0001)_\omega$ // $(111)_\beta$ and $[1120]_\omega$ // $[110]_\beta$, whenever it is present in the β phase. ω-type phases have also been observed in many different alloy systems especially those which contain ordered β (B2) phase, e.g., Cu-Zn, Ag-Cd, Ag-Zn, Fe-Al, Ni-Al, etc [41]. ω-type phases have also been observed in Ti-Al-Nb system [41,42]. The selected area diffraction patterns obtained from the region containing the B2 phase conform well with those obtained from the B2 phase containing ω-type precipitates in Ref.[42]. The diffraction patterns obtained from the region close to the outer edge of

the specimen corresponded to those of $B8_2$ structure. The diffraction patterns taken from the B2 phase present in the central region of the damaged layer confirmed the presence of ω″ phase.

Mn and Nb also modify the $\alpha/\alpha+\gamma$ and the $\alpha+\gamma/\gamma$ phase boundaries and their estimated quantitative effects are given in Table 5.2. Nb has no significant effect on these phase boundaries whereas Mn shifts both the boundaries towards the higher Al side. The Al content near the interface between the damaged layer and the bulk was observed to be ~41 at.%. In the binary Ti-Al system alloy containing 41 at.% Al would lie in the $\alpha+\gamma$ two phase field at 1200°C. When air cooled from the two phase field the alloy should transform to a lamellar structure. However, the region close to the interface between the damaged layer and bulk did not show lamellar structure rather a single phase α_2 structure. This region also contained about 1.7 at.% Mn and 2 at.% Nb. The presence of 1.7 at.% Mn and 2 at.% Nb would shift the $\alpha/\alpha+\gamma$ phase boundary from 40.6 to 45.5 at.% and the $\alpha+\gamma/\gamma$ phase boundary from 47.8 to 50.5 at.% Al. Thus in the presence of Mn and Nb, the alloy containing 41 at.% Al would lie well within the α single phase field (Fig.5.9). The transformation of α, upon cooling to room temperature depends on the composition of α relative to the eutectoid composition. The presence of Mn and Nb also shift the $\alpha_2/\alpha_2+\gamma$ and the $\alpha_2+\gamma/\gamma$ phase boundaries towards higher Al content, as seen from the ternary Ti-Al-Mn and Ti-Al-Nb diagrams at 1000°C in Fig.5.5 and 5.7, respectively. The data extracted from these diagrams are listed in Table 5.3. Assuming the effect of Mn and Nb to be additive, positions of $\alpha_2/\alpha_2+\gamma$ and $\alpha_2+\gamma/\gamma$ phase boundaries are estimated in the alloy containing 1.7 at.% Mn and 2 at.% Nb. The aluminum content of these boundaries

Alloying element	Al content of the phase boundary (at.%)	
	$\alpha_2/\alpha_2+\gamma$	$\alpha_2+\gamma/\gamma$
From phase diagrams		
0 %	37.5	48
2 % Mn	38	45
2 % Nb	38	47.5
Estimated		
2 % Mn + 2 % Nb	38.5	44.5
2.5 % Mn + 2.8 % Nb	38.8	43.5
1.7 % Mn + 2 % Nb	38.4	45

Table 5.3 Effect of alloying elements on the $\alpha_2/\alpha_2+\gamma$ and $\alpha_2+\gamma/\gamma$ phase boundaries at a temperature close to 1000°C

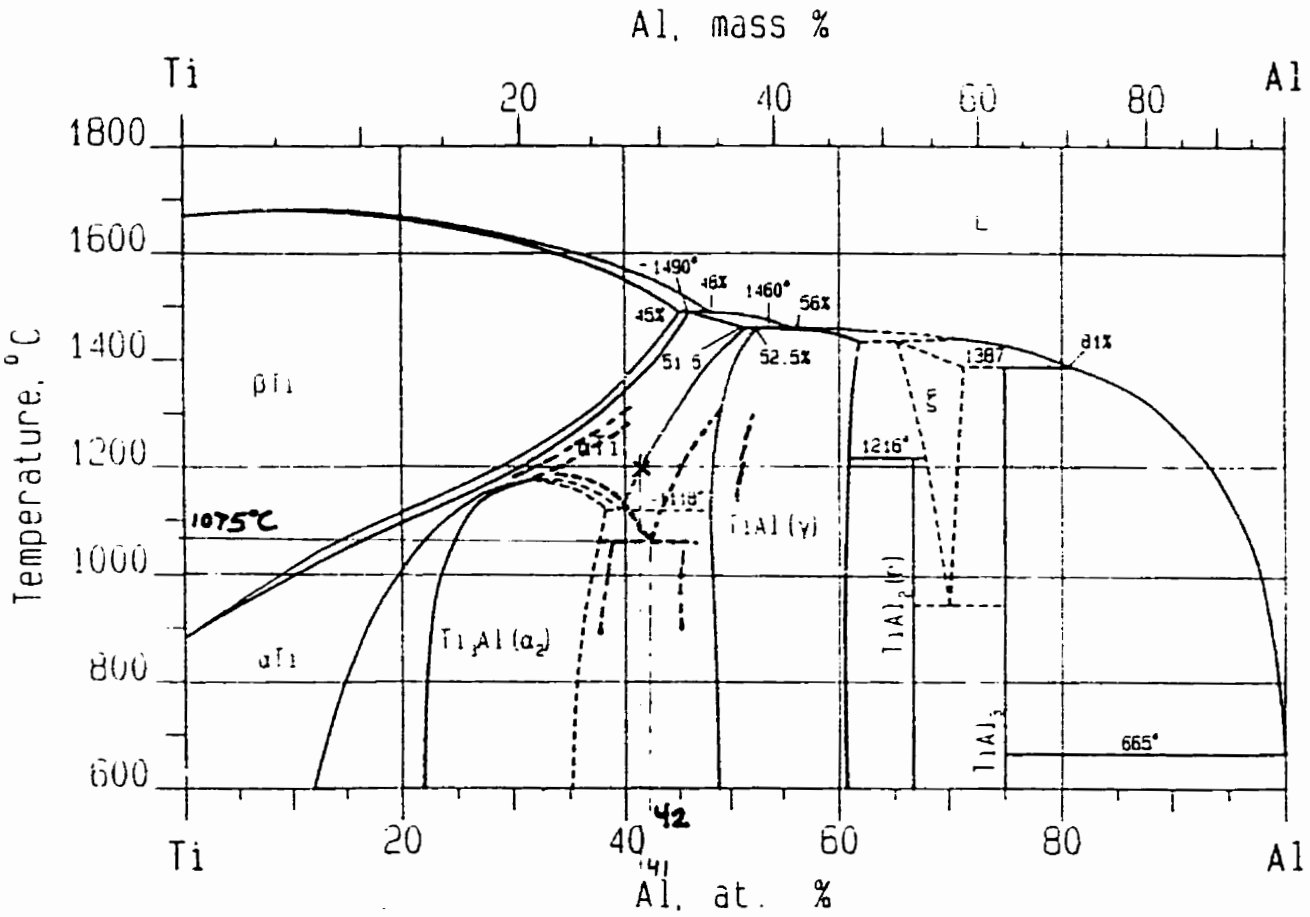

Fig.5.9 Ti-Al phase diagram showing the effect of 1.7 at.% Mn + 2 at.% Nb on the phase boundaries, and the eutectoid composition and temperature. New boundaries are constructed assuming that the phase boundaries shift parallel to the existing phase boundaries.

is estimated to be 38.4 and 45 at.%, respectively. These data are plotted in Fig.5.9. Assuming the shift in the $\alpha_2+\alpha/\alpha$ phase boundary to be similar to that of the $\alpha_2/\alpha_2+\gamma$ boundary and assuming the boundaries to be parallel to those of binary Ti-Al system, the eutetcoid composition and temperature can be estimated. The new estimated eutectoid composition and temperature are shown in Fig.5.9. The eutectoid composition in the alloy containing 1.7 at.% Mn and 2 at.% Nb would be close to 42 at.% Al, which is higher than the observed composition of ~ 41 at.% Al at the interface. It has been shown in literature [18] that when Al content is less than the eutectoid composition, cooling the alloy from the α phase field results in the formation of α_2 phase. Thus, α_2 phase is observed near the interface between the damaged layer and the lamellar bulk.

To summarize, the phases present in the damaged layer, when the specimen was air cooled from 1200°C to room temperature, cannot be explained simply on the basis of the binary Ti-Al system. However, when the effect of Mn and Nb is taken into account, the formation of various phases can be rationalized.

5.4 OXIDATION BEHAVIOUR

The EDS analysis of the various layers of the oxide scale (Fig. 4.30 to 4.33) showed that: the outer most layer consisted of TiO_2, the layer just below the TiO_2 layer consisted of Al_2O_3 and the innermost layer was a mixture of TiO_2 and Al_2O_3. The structure of the oxide scale is quite consistent with the oxidation mode suggested for oxidation of TiAl in

the temperature range of 800°C to 1100°C [12,107]. Al-depletion leading to the formation of damaged layer has been reported in literature [11-13] during oxidation of TiAl. Formation of damaged layer was observed in the present investigation when the alloy was oxidized in air at 850°C. The layer just below the oxide scale was rich in Ti and the damaged layer just between this Ti rich layer and the lamellar bulk was rich in Al. This was confirmed by microanalysis at various locations of the damaged layer (Table 4.7).

Chapter 6

CONCLUSIONS

On the basis of the results and discussions of the present work, presented in the preceding chapters, the following conclusions can be drawn:

- Loss of Al, Mn and Ti took place during annealing of the Ti-45Al-2Mn-2Nb alloy at 1200°C resulting in the formation of a damaged surface layer.
- Solutes evaporated from the surface of the specimen and deposited on the inner surface of the Ta foil that was used to wrap the specimen to minimize oxidation.
- The thickness of the damaged layer increased with increase in time and was proportional to the square root of time.
- The damaged layer consisted of α_2 phase near the interface and B2 phase along with ω-type phase precipitates near the outer surface of the specimen. Right at the outer edge of the specimen, the B2 phase consisted of ω-type phase having $B8_2$ structure whereas B2 phase in the centre of the damaged layer consisted of ω'' phase.
- Surface damage occurred even during oxidation in air at 850°C which is close to the service temperature of the γ-based titanium aluminides.

Suggested future work:

1. The solutes evaporate from the surface of the specimen during heat treatment. The amount of solute evaporating from the surface of the specimen would depend on the pressure inside the capsule in which the specimens were sealed during heat treatment.

The future work could include the study of the effect of pressure of loss of solutes and surface damage during heat treatment.

2. As suggested in section 5.1, the solute atoms diffuse out to the surface of the specimen and evaporate, thus causing solute depletion. A suitable surface modification treatment could be devised which would reduce the movement of solute atoms to the surface and thus prevent surface damage during heat treatment and during service.

REFERENCES

1. P.Bartolatta, J.Barret, T.Kelly, and R.Smashey, Journal of Metals, May 1997, pp.48.

2. Y.W.Kim, Journal of Metals, 46, No.7 (1994), pp.30.

3. Helmet Clemens, Z. Metallkd., 86 (1995) 12, pp.814.

4. Y.W.Kim, Journal of Metals, 41, No.7 (1989) pp.24.

5. D.M.Dimiduk, Gamma Titanium Aluminides, eds. Y.W.Kim, R. Wagner, and M. Yamaguchi, TMS, (1995), pp.3.

6. C.M.Austin and T.J.Kelly, Gamma Titanium Aluminides, eds. Y.W.Kim, R.Wagner and M Yamaguchi, TMS (1995), pp.21.

7. S.E.Hartfield-Wunsch, A.A.Sperling, R.S.Morrison, W.E.Dowling, Jr., and J.E.Allison, Gamma Titanium Aluminides, eds. Y.W.Kim, R.Wagner, and M.Yamaguchi, TMS (1995), pp.41.

8. R.V.Ramanujan, P.J.Maziasz and C.T.Liu, Acta. Met., vol.44, No.7, (1996), pp.2611.

9. W.A.Baeslack, P.A.McQuay, D.S.Lee, and E.D.Fletcher, Materials Characterization, 31, (1993), pp.197.

10. V.Shemet, H.Hoven and W.J.Quadakkers, Intermetallics, 5, (1997), pp.311.

11. N.Zheng, W.Fischer, H.Grubmeier, V.Shemet, and W.J.Quadakkers, Scripta Met., Vol.33, No.1, (1995), pp.47.

12. R.Beye, M.Verwerft, J.T.M.DeHosson, and R.Gronsky, Acta Met., Vol.44, No.10, (1996), pp.4225.

13. M.Yoshihara, K.Miura, and Y.W.Kim, Gamma Titanium Aluminides, eds. Y.W.Kim, R.Wagner, and M.Yamaguchi, TMS, (1995),pp.93

14. H.R.Ogden, D.J.Maykuth, W.L.Finlay, and R.I.Jaffee. Journ. Metals, 3 (12), (1951), pp.1150.

15. E.S.Bumps, H.D.Kessler and M.Hansen, Journ. Metals, 4 (6), (1952), pp.609.

16. J.L.Murray, Met. Trans., Vol.19A, (1988), pp.243.

17. C.McCullough, J.J.Valencia, C.G.Levi, and R.Mehrabian, Acta Met., Vol.37, No.5, (1989), pp.1321.

18. S.A.Jones and M.J.Kaufmann, Acta Met., Vol.41, No.2, (1993), pp.387.

19. J.J.Ding, G.W.Qin, S.M.Hao, X.T.Wang, and G.L.Chen, Journal of Phase Equilibria, Vol.17, No.2, (1996), pp.117

20. A Comprehensive Compendium of Evaluated Constitutional Data and Phase Diagram, eds.G.Petzow and G. Effenberg, Vol.7.

21. D.Veeraraghavan, U.Pilchowski, B.Natarajan, and V.K.Vasudevan, Acta Met., Vol.46, No.2, (1998), pp.401.

22. F.H.Froes, C.Suryanarayana, and D.Eliezer, Journal of Material Science, Vol.27, (1992), pp.5113.

23. S.C.Huang, and J.C Chesnutt, Intermetallic Compounds, eds. J.H.Westbrook and R.L.Fleischer, Vol.2, (1994), pp.73.

24. D.Banerjee, Intermetallic Compounds, eds. J.H.Westbrook and R.L.Fleischer, Vol.2, (1994), pp.91.

25. V.M.Imayev, G.A.Salishchev, R.M.Imayev, N.K.Gabdullin, and A.V.Kuznetsov, Structural Intermetallics, (1997), pp.505.

26. Y.W.Kim, MRS Symp. Proc., (1991), Vol.213, pp.777.

27. Y.W.Kim, JOM, (1991), pp.40.

28. J.H.Perepezko, Y.A.Chang, L.E.Seitzman, J.C.Lin, N.R.Bonda, T.J.Jewett, and J.C.Mishurda, High Temperature Aluminides and Intermetallics, eds. S.H.Whang et al., TMS, (1990), pp.19.

29. Y.G.Li and M.H.Loretto, Acta Met., Vol.42. No.6, (1994), pp.2009.

30. R.F.Domagala, and W.Rostoker, Trans. ASM, Vol.47, (1955), Pp.565.

31. D.J.Chakrabarti, Metall. Trans., Vol.8B, (1977), pp.121.

32. I.Jacob and D.Shaltiel, Mat. Res. Bull., Vol.13, (1978), pp.1193.

33. K.Hashimoto, H.Doi, K.Kasahara, T.Tsujimoto, and T.Suzuki, J. Jpn. Inst. Met., Vol.52, (1988), pp.816.

34. C.J.Butler, D.G.McCartney, C.J.Small, and N.Saunders, Acta Met., Vol.45, No.7, (1997), pp.2931.

35. K.Kaltenbach, S.Gamma, D.G.Pinatti, K.Schulze and E-Th. Henig, Z. Metallkd, Vol.80, (1989), pp.535.

36. C.H.Ward, Int. Mat. Rev., Vol.38, No.2, (1993), pp.79.

37. T.J.Jewett, J.C.Lin, N.R.Bond, L.E.Seitzman, K.C.Hsiech, Y.A.Chang and J.H. Perepezko, MRS Symp. Proc., Vol.133, (1989), pp.133.

38. A.Zdziobek, M.Durand-Charre, J.Driole, and F.Durand, Z. Metallkd., Vol.86, (1995), pp.334.

39. E.S.K.Menon, P.R.Subramanian, and D.M.Dimiduk, Scripta Met., Vol.27, (199), pp.265.

40. A.Hellwig, M.Palm, and G.Inden, Intermetallics, Vol.6, No.2, (1998), pp.79.

41. R.Strychor, J.C.Williams, and W.A.Soffa, Met. Trans. Vol.19A, (1988), pp.225.

42. L.A.Bendersky, W.J.Boettinger, B.P.Burton, F.S.Biancaniello, and C.B.Shoemaker, Acta Met., Vol.38, (1990), pp.931.

43. D.Banerjee, A.K.Gogia, T.K.Nandi, and V.A.Joshi, Acta Met., Vol.36, (1988), pp.871.

44. K.Muraleedharan, A.K.Gogia, T.K.Nandy, D.Banerjee, and S.Lele, Met. Trans., Vol.23A, (1992), pp.401.

45. S.C.Huang and E.L.Hall, Met. Trans., Vol.22A, (1991), pp.2619.

46. S.C.Huang and E.L.Hall, Acta Met, Vol.39, (1991), pp.1053.

47. T.Tsujimoto and K.Hashimoto, MRS Symp. Proc., Vol.133, (1989), pp.391.

48. P.L.Martin, M.G.Mandiratta and H.A.Lipsitt, Met. Trans., Vol.14A, (1983), pp.2170.

49. S.Tsuyama, S.Mitao, and K.Minakawa, Mater. Sci. Eng. A, Vol.153, (1992), pp.451.

50. M.Es-souni, A.Bartels and R.Wagner, Mat. Sci. and Eng., A171, (1993), pp.127.

51. D.W.Mckee and S.C.Huang, Corrosion Science, Vol.33, (1992), pp.1899.

52. J.B.McAndrew and H.D.Kessler, J.Met, Vol.8, (1956), pp.1348.

53. R.A.Perkins, K.T.Chiang and G.H.meier, Scripta Met., Vol.21, (1987), pp.1505.

54. Y.Ikematsu, T.Hanamura, H.Morikawa, M.Tanino and J.Takamura, In Intermetallic Compounds-Structure and Mechanical Properties, ed. O.Izumi, The Jpn. Inst. Met., (1991), pp.191.

55. K.Kasahara, K.Hashimoto, H.Doi, and T.Tsujimoto, J. Jpn. Inst. Met., Vol.53, (1990), pp.58.

56. A.Denquin, S.Naka, and T.Khan, Titanium 92, Science and Technology, eds. F.H.Froes and I.L.Caplan, pp.1017.

57. A.Denquin and S.Naka, Gamma Titanium Aluminides, eds. Y.W.Kim, R.Wagner, and M.Yamaguchi, (1995), pp.141.

58. C.R.Feng, D.J.Michel, and C.R.Crowe, Scripta Met., Vol.23, (1989), pp.241.

59. J.J.Valencia, C.McCullough, C.G.Levi, and R Mehrabian, Scripta Met., Vol.21, (1987), pp.1341.

60. S.A.Jones, R.D Shul, A.J.McAlister, and M.J.Kaufmann, Sripta Met., Vol.22, (1988), pp.1235.

61. Q.Xu, C.H.Lei, and Y.G.Zheng, Gamma Titanium Aluminides, eds. Y.W.Kim, R.Wagner, and M.Yamaguchi, (1995), pp.189.

62. A.Denquin and S.Naka, Acta Met., Vol.44, No.1, (1996), pp.343.

63. Y.Yamabe, M.Takeyama, and M.Kikuchi, Gamma Titanium Aluminides, eds. Y.W.Kim, R.Wagner, and M.Yamaguchi, (1995), pp.111.

64. M.J.Blackburn, The Science Technology and Applications of Titanium, eds. R.I.Jaffee and N.E.Promisel, Vol.633, (1970).

65. J.M Howe, U.Dahmen, and R.Gronsky, Phil. Mag., Vol.56A, (1987), pp.31.

66. H.I.Aaronson, Met. Trans., Vol.24A, (1993), pp.241.

67. E.Abe, T.Kumagai, and M.Nakamura, Structural Intermetallics, (1997), pp.167.

68. P.Wang, G.B.Viswanathan, and V.K.Vasudevan, Met. Trans, Vol.23A, (1992), pp.690.

69. X.D.Zhang, T.A.Dean, and M.H.Loretto, Acta Met., Vol.42, (1994), pp.2035.

70. A.Denquin and S.Naka, Phil. Mag. Lett., 68, 13, (1993).

71. X.D.Zhang, S.Godfrey, M.Weaver, M.Strangwood, P.Threadgill, M.J.Kaufman, and M.H.Loretto, Acta Met., Vol.44, (1996), pp.3723.

72. P.Wang and V.K.Vasudevan, Scripta Met., Vol.27, (1992), pp.89.

73. P.McQuay, D.M.Dimiduk, and S.L.Semiatin, Scripta Met., Vol.25, (1991), pp.1689.

74. M.C.Chaturvedi, N.L.Richards, and Q.Xu, Mat. Sci. and Eng., A239-240, (1997), pp.605.

75. Kestner-Weykamp et al., Scripta Met., Vol.23, (1989), pp.1697.

76. D.Banerjee, A.K.Gogia, A.K.Nandi and V.A.Joshi, Acta Met., Vol.36, (1988), pp.871.

77. L.M.Hsiung and H.N.G.Wadley, Scripta Met., Vol.26, (1992), pp.35.

78. K.Muralledharan and D.Banerjee, Scripta Met., Vol.29, (1993), pp.527.

79. T.T.Cheng and M.H.Loretto, Structural Intermetallics, (1997), pp.253.

80. M.Krishnan, B.Natarajan, V.K.Vasudevan, and D.M.Dimiduk, Structural Intermetallics, (1997), pp.235.

81. N.Masahashi and Y.Mizuhara, Gamma Titanium Aluminides, eds. Y.W.Kim, R.Wagner, and M.Yamaguchi (1995), pp.165.

82. M.A.Morris, Y.G.Li, and M.Lebeuf, Scripta Met. Vol.31, (1994), pp.449.

83. P.D.Frost, W.M.Parris, L.L.Hirsch, L.L.Doig, and C.M.Schwartz, Trans. ASM, Vol.46, (1954), pp.231.

84. Y.W.Kim, Acta Met., Vol.40, (1992), pp.40.

85. Y.W.Kim, Gamma Titanium Aluminides, eds. Y.W.Kim, R.Wagner, and M.Yamaguchi, (1995), pp.777.

86. Y.W.Kim, Microstructure/Property Relationship in Titanium Aluminides and Alloys, eds. Y.W.Kim and R.R.Boyer, (TMS 1990), pp.91.

87. D.S.Shih et al, Microstructure/Property Relationship in Titanium Aluminides and Alloys, eds. Y.W.Kim and R.R.Boyer, (TMS 1990).

88. D.S.Schwartz and W.O.Soboyejo, Microstructure/Property Relationship in Titanium Aluminides and Alloys, eds. Y.W.Kim and R.R.Boyer, (TMS 1990).

89. K.S.Chan and Y.W.Kim, Met. Trans., 23 A (1992), pp.1663.

90. D.L.Davidsen and J.B.Campbell, Met. Trans., 24 A (1993) pp.1555.

91. S.Mitao, T.Isawa and S.Isuyana, Scripta Met, 336 (1992), pp.1405.

92. R.Gnanamoorthy, Y Moutoh, K.Hayashi, Y.Mizuhara, Scripta Met, 33 (1995), pp.907.

93. J.Beddoes, L.Zhao, J.Triantafillou, P.Au and W.Wallace, Gamma Titanium Aluminides, eds. Y.W.Kim, R.Wagner, and M.Yamaguchi, (1995), pp.959.

94. J.Beddoes, L.Zhao, P.Au, D.Dudzinski and J.Triantafillou, Structural intermatallics, (1997), pp.109.

95. M.M.Keller, V.Aubourg, P.E.Janes, W.J.Porter,III, and D.Eylon, Titanium'95: Science and Technology,(1995), pp.184.

96. T.A.Parthasarthy, M.G.Mendiratta and D.M.Dimiduk, Scripta Met, Vol.173, (1997), pp.315.

97. R.W.Hayes and P.A.McQuay, Scripta Met., Vol.30, (1994), pp.259.

98. J.M.Larsen, B.D.Worth, S.J.Balsene, J.W.Jones, GTA, (1995), pp.821.

99. K.S.Chan and Y.W.Kim, Acta Met., (1995), pp.439.

100. R.W.Beye and R.Gronsky,Acta Met., Vol.4, (1994), pp.137.

101. M.Yoshihara, R. Tanaka, T. Suzuki aand M.Shimizu, M.R.S. Symp-proc., Vol. 213, (1991), pp.975.

102. J.M.Rakowski, F.S.Pettit, G.M.Meier, F. Dettenwanger, E.Schimann and M.Ruhle, Scripta Met., Vol. 33, (1995), pp.997.

103. Choudhury, M.S., M.C. Graham, and J.W.Hinze, Foroulis Z.A. and Pettit F.S(eds), "Oxidation Behaviour of Titanium Aluminides", in properties of High temperature alloys, The electrochem Soc., (1976), pp.662.

104. G.M.Meier, D.Appalonia, R.A.Perkins and K.T.Chiang, in T.Grobstein and J.Doychak (eds), Oxidation of high temperature Intermetallics, (TMS,1989), pp.185.

105. S.Becker, A.Rahmel, M.Schorr, and M.Schutze, Oxid. Metals, Vol.38, (1992), pp.425.

106. Michael D. Brady, William J.Brindly, James L. Smialek, and Ivan E.Locci, JOM, November 1996, pp.46.

107. K.Maki et al, Mat. Sci and Eng., A153, (1992), pp.591.

108. Y.W.Kim, Mat. Res.Soc. Synp. Proc., Vol.213,(1991), pp.777.

109. J.C.Schaeffer, C.M.Austrin, and F.Kaempf, Gamma Titanium Aluminides, ed. Y.W.Kim, R.Wagner, and M.Yamaguchi,(1995), pp.71.

110. S.Taniguchi and T.Shibata, Intermetallics, Vol.4, (1996), pp.85.

111. R.L.McCarron et al, Titanium 1992, ed F.H.Froes and I Caplan (Warrendale, PA: TMS),(1993), pp.1971.

112. M.P.Brady, J.L.Smialk, and F.Terepka, Scripta Met. Mater., 32(10), (1995), pp.1659.

113. M.P.Brady, J.L.Smialek, and D.L.Humphrey, Mat. Res. Soc. Symp. Proc., Vol.364, (1995), pp.1309.

IMAGE EVALUATION
TEST TARGET (QA-3)

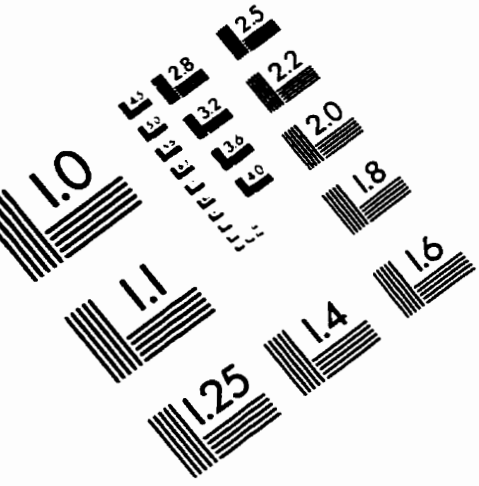

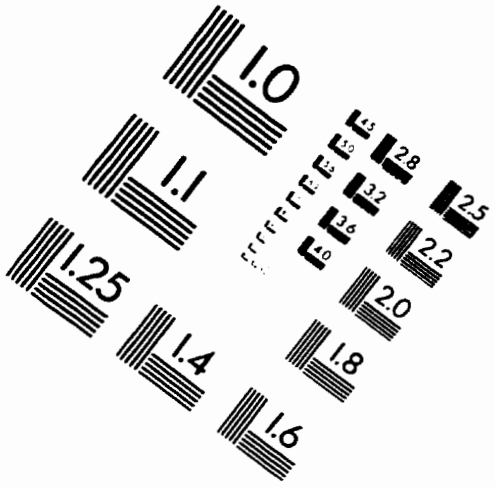

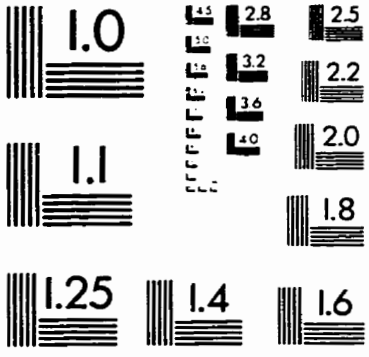

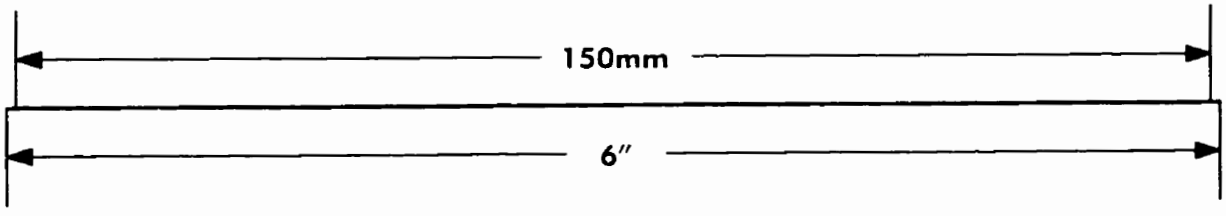

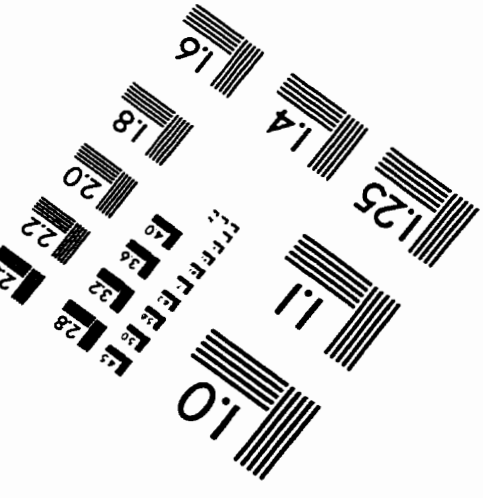

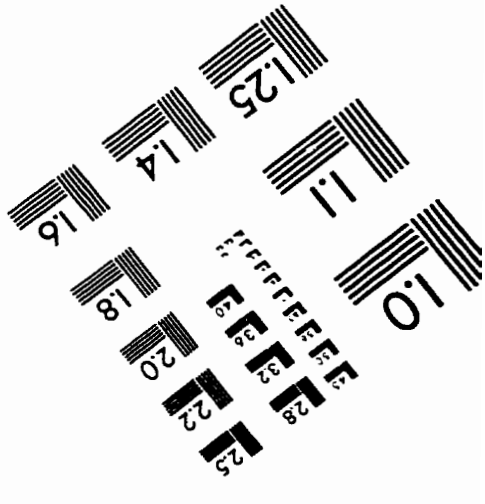

APPLIED IMAGE . Inc
1653 East Main Street
Rochester, NY 14609 USA
Phone: 716/482-0300
Fax: 716/288-5989